# TAILORED 3D GRAPHENE BASED MATERIALS FOR ENERGY CONVERSION AND STORAGE

by

XUELIU FAN

Submitted in partial fulfillment of the requirements

for the degree of Doctor of Philosophy

Dissertation Adviser: Professor Liming Dai

Department of Macromolecular Science and Engineering

CASE WESTERN RESERVE UNIVERSITY

January 2018

CASE WESTERN RESERVE UNIVERSITY

SCHOOL OF GRADUATE STUDIES

We hereby approve the thesis/dissertation of

Xueliu Fan

Candidate for the degree of Doctor of Philosophy*

Professor Liming Dai ____________________________________________

(Chair of the committee)

Professor David Schiraldi ________________________________________

(Committee member)

Professor Alex. M. Jamieson ______________________________________

(Committee member)

Professor Clemens Burda ________________________________________

(Committee member)

Date of Defense

June, 30th, 2017

*We also certify that written approval has been obtained for any proprietary material contained therein.

# TABLE OF CONTENTS

**List of Table**.......... IV
**List of Figures**.......... V
**Acknowledgment**.......... XII
**Abstract**.......... XIII
1. Introduction .......... 1
  1.1 Introduction of three-dimensional (3D) graphene.......... 1
  1.2 Structure of 3D graphene .......... 3
  1.3 Synthesis of 3D graphene.......... 4
    1.3.1 Liquid-phase exfoliation .......... 5
    1.3.2 Chemical vapor deposition .......... 6
  1.4 Synthesis of 3D graphene/2D, 1D, 0D nanomaterial hybrids .......... 8
    1.4.1 Solution-based method.......... 10
    1.4.2 Chemical vapor deposition derived heterostructure .......... 11
  1.5 Functionalization of 3D graphene .......... 12
    1.5.1 Heteroatom doping.......... 14
    1.5.2 Non-covalent functionalization.......... 15
  1.6 Energy conversion and storage application of 3D graphene-based materials..... 15
    1.6.1 Fuel cell based on 3D graphene cathode.......... 18
    1.6.2 3D graphene based electrodes for supercapacitors .......... 20
    1.6.3 3D graphene-based anode for lithium-ion batteries.......... 22
  1.7 Research objective.......... 25
2. Zeolite-Y-templated N-doped nanoporous graphene for oxygen reduction reaction and lithium ion batteries.......... 26
  2.1 Introduction .......... 26
  2.2 Experimental section .......... 28
    2.2.1 Preparation of NPG and N-NPG.......... 28
    2.2.2 Template removal .......... 29
    2.2.3 Characterization.......... 29
    2.2.4 Electrocatalytic activity evaluation.......... 30
    2.2.5 Lithium-ion battery measurements .......... 30

2.3 Results and discussion ... 30
Electrochemical evaluation of N-NPG for ORR ... 42
N-NPG as anode in lithium-ion batteries ... 46
2.4 Conclusions ... 48
3. Graphene networks for high-performance flexible and transparent supercapacitors 50
3.1 Introduction ... 50
3.2 Experimental section ... 52
3.2.1 Synthesis of graphene network via two-step CVD ... 52
3.2.2 Transfer process of graphene network ... 52
3.2.3 Fabrication of supercapacitors using graphene network electrodes ... 53
3.2.4 Characterization ... 53
3.3 Results and discussion ... 54
3.4 Conclusions ... 69
4. N-doped 3D graphene-CNT-graphene for all-solid-state supercapacitors ... 71
4.1 Introduction ... 71
4.2 Experimental section ... 72
4.2.1 AAO template preparation ... 72
4.2.2 CVD synthesis of N-G-CNT-G ... 73
4.2.3 CVD synthesis of G-CNT-G ... 73
4.2.4 Characterization ... 74
4.2.5 Fabrication of N-G-CNT-G and G-CNT-G based all-solid-state supercapacitors ... 74
4.3 Results and discussion ... 75
4.4 Conclusions ... 89
5. Hierarchical $MoS_2$ decorated 3D graphene as anodes for lithium-ion battery ... 90
5.1 Introduction ... 90
5.2 Experimental section ... 92
5.2.1 AAO template preparation ... 92
5.2.2 CVD synthesis of 3DG ... 93
5.2.3 CVD synthesis of $MoS_2$-3DG ... 93
5.2.4 Transfer $MoS_2$-3DG thin films ... 93
5.2.5 Characterization ... 94
5.2.6 Battery assembly ... 94

5.3 Results and discussion .......... 95

Electrochemical performance of the $MoS_2$-3DG films .......... 106

5.4 Conclusions .......... 114

6. Bibliography .......... 115

## List of Table

Table 1 Comparison of electrochemical properties of $MoS_2$ and $MoS_2$/carbon nanomaterial hybrids........................................................................................... 110

## List of Figures

Figure 1.1 (a) Graphene hexagonal structure of identical carbon atoms, (b) schematic of in-plane σ bonds and π orbitals vertical to the basal plane[18], reprinted from ref. [18], copyright © 2008 IOP Publishing Ltd; (c) photograph of a multilayer graphene flake with thickness ~3 nm[5], reprinted from ref. [5], copyright © 2004 AAAS; (d) white light transmittance of single and bilayer graphene sheets[7], reprinted from ref. [7], copyright © 2008 AAAS; (e) Raman spectra (532 nm laser wavelength) of graphene[19], reprinted from ref. [19], copyright © 2009 Nature Publishing Group. ........................................................................ 3

Figure 1.2 (a) Chemical structure of graphite oxide[21], reprinted from ref. [21], copyright © 2009 Nature Publishing Group; (b) schematic hydrothermal method for preparation of self-assembled graphene hydrogel (SGH), (c) SEM image of SGH interior microstructures, (d) photography of strong SHG[22], reprinted from ref. [22], copyright © 2010 American Chemical Society; (e) synthesis of graphene foam (GF) by CVD method and transfer of graphene foam (GF) by etching Ni foams, (f) SEM image of GF, (g) photography of free-standing GF[23], reprinted from ref. [23], copyright © 2011 Nature Publishing Group. ...... 4

Figure 1.3 (a) Fabrication process for the 3D $Fe_3O_4$/N-doped graphene aerogels (N-GAs) by hydrothermal self-assembly and freeze-drying, (b) SEM image of 3D $Fe_3O_4$/N-GAs with macroporous structure, (c) $Fe_3O_4$ nanoparticles encapsulated in thin graphene layers[58], reprinted from ref. [58], copyright © 2013 American Chemical Society; (d) schematic of the 3D graphene-radially aligned CNT (RACNT) structure by CVD method, (e) TEM of RACNT with close end[59], reprinted from ref. [59], copyright © 2015 AAAS; (f) SEM image of $MoS_2$/3D graphene networks by CVD method, (g) HRTEM images of $MoS_2$ particles on the surface of 3D graphene networks[46], reprinted from ref. [46], copyright © 2013 John Wiley & Sons, Inc. ............................................................................... 9

Figure 1.4 Functionalization possibilities for graphene: (a)edge-functionalization, (b)basal-plane-functionalization, (c)non-covalent adsorption on the basal plane, (d) asymmetrical functionalization of the basal plane, and (e) self-assembling of functionalized graphene sheets; (f) chemical structure of graphene oxide[13], reprinted from ref. [13], copyright © 2012 American Chemical Society. ...................................................................... 13

Figure 1.5 Schematic principles of (a) fuel cell, (b) electrochemical double-layer supercapacitor, and (c) lithium-ion battery. ..................................................................... 17

Figure 1.6 (a) Schematic structure of B,N-co-doped graphene, (b) rotating disk electrode voltammograms of the undoped graphene foam (GF), B-doped GF, N-doped GF, and B,N-co-doped GF based electrode, and the commercial Pt/C based electrode in an oxygen saturated 0.1 M KOH solution, (c) CO tolerance test of B,N-co-doped GF and the commercial Pt/C based electrode[76], reprinted from ref. [76], copyright © 2013 Royal Society of Chemistry; (d) Raman spectrum of NiO/graphene composites, (e) cyclic voltammetry curves and (f) specific capacitance of NiO/graphene composites[83] , reprinted from ref. [83], copyright © 2011 John Wiley & Sons, Inc; (g) TEM image of microstructure of $MoS_2$/G (1:2) composite, (h) charge and discharge curves of $MoS_2$/G (1:2) composite, (i) rate capability of $MoS_2$/G (1:2) composites at different current densities[68], reprinted from ref. [68], copyright © 2011 American Chemical Society. ....................................... 17

Figure 2.1 Zeolite-Y templated N-NPG through CVD method: (a) schematic of zeolite-Y with FAU (faujasite) structure, (b) and (c) SEM images of zeolite-Y templated N-NPG under different magnifications, (d-f) TEM of the N-NPG nanosheets with nanopores.... 32

Figure 2.2 (a) and (b) SEM images of N-NPG under different scale. .............................. 32

Figure 2.3 (a) XRD of zeolite-Y, zeolite-Y-templated NPG, zeolite-Y-templated N-NPG; (b) the corresponding small angle XRD. ......................................................................... 33

Figure 2.4 (a) Raman spectra of NPG and N-NPG; (b) XPS survey spectrum of N-NPG-3 from zeolite-Y template, it reveals there are C, N, and O elements in the resulting sample; high-resolution XPS of (c) C1s and (d) N1s in N-NPG-3 samples. ................................ 35

Figure 2.5 (a) Nitrogen adsorption/desorption isotherms and related pore size distribution (b) of N-NPG. ............................................................................................................... 36

Figure 2.6 (a) XRD and (b) Raman spectra of three zeolite-Y templated NPG for investigation of the growth temperature effect. .............................................................. 37

Figure 2.7 TGA of zeolite-Y-templated NPG showing the carbon depositing ratio to the zeolite-Y with the increasing growth time. ...................................................................... 37

Figure 2.8 Raman spectra of three zeolite-Y-templated NPG for investigation of the growth time effect. ........................................................................................................ 38

Figure 2.9 (a) The atomic percentage (%) of C, N, O in graphene and N-NPG through XPS; (b) distribution of N species (%)........................................................................ 39

Figure 2.10 (a) Schematic nitrogen types in N-doped graphene; high-resolution (HR-XPS) spectrum of N 1s from (b) N-NPG-1, (c) N-NPG-2, and (d) N-NPG-4. .......................... 40

Figure 2.11 N-doped nanoporous graphene from zeolite-ZSM-5: (a) structure of zeolite-ZSM-5; (d) Raman spectrum, (b) and (c) SEM images, (e) XRD and (f) SAXRD of N-doped nanoporous graphene derived from zeolite-ZSM-5. ............................................. 41

Figure 2.12 (a) CV curve of N-NPG catalyst for the ORR in an $O_2$ and $N_2$-saturated KOH solution (0.1 M); (b) RRDE voltammograms for the N-NPG catalyst at 1600 rpm and the ring electrode was polarized at 1.1 V, the scan rate: 10 mV $s^{-1}$; (c) LSV for NPG, N-NPG, and Pt/C catalysts on RDE at 1600 rpm; (d) LSVs on RDE at different rotating speed; (e) current-time chronoamperometric response of N-NPG and Pt/C catalysts in an $O_2$-saturated KOH solution at a potential of -0.2 V, the rotating speed: 400 rpm; (f) current-time chronoamperometric response of N-NPG and Pt/C catalysts, the two arrows indicate the introduction of $O_2$ and 10 vol% methanol, respectively. ................................................. 43

Figure 2.13 (a) CV curves for the ORR in $O_2$-saturated 0.1 M KOH at NPG electrode (black) and N-NPG electrode (with different N content); (b) LSV curves for NPG electrode (black) and N-NPG electrode at an RRDE (1600 rpm), scan rate: 0.01 V $s^{-1}$.............................. 45

Figure 2.14 (a) Galvanostatic discharge and charge curves of N-NPG anode based LIB at a current density of 0.1 A $g^{-1}$ measured in a voltage range from 0.02 to 3.0 V; (b) cycling performance at 0.1A $g^{-1}$; (c) discharge and charge profiles at various current rates; (d) the corresponding rate performance. ........................................................................ 47

Figure 3.1 Schematic illustration of the procedures for the growth and transfer of the large-scale graphene network (GN), along with the flexible and transparent all-solid-state supercapacitor constructed by sandwiching PVA/$H_3PO_4$ electrolyte between two PDMS-supported GN electrodes, reprinted from ref. [150], copyright © 2014 The Royal Society of Chemistry........................................................................................................ 54

Figure 3.2 Schematic diagrams of two-step chemical vapor deposition for the synthesis of graphene network films. Step 1: heating up to 960 ℃ with a fast cooling process to form copper network; Step 2: at 960 ℃ for graphene growth on the copper network, reprinted from ref. [150], copyright © 2014 The Royal Society of Chemistry. ............................. 55

Figure 3.3 SEM images of copper network-like structures by annealing 300 nm-thick sputter-coated copper layer on silicon wafers as a function of the annealing temperature. (a) and (b) the dot-like copper formed at 1000 ℃; (c) and (d) the finger-like copper formed at 970℃, reprinted from ref. [150], copyright © 2014 The Royal Society of Chemistry. 56

Figure 3.4 SEM images of the copper networks generated from 300 nm-thick copper coatings by heating at 960 ℃ for 180 s under Ar with different flow rates. From a) to d), Ar flow rates are 50, 100, 200, and 400 sccm, respectively, reprinted from ref. [150], copyright © 2014 The Royal Society of Chemistry. ...................................................... 57

Figure 3.5 The surface coverage ratio of the Cu network formed by annealing at 960 ℃ for 180 s as a function of the Ar flow rate (50, 100, 200, and 400 sccm), reprinted from ref. [150], copyright © 2014 The Royal Society of Chemistry.............................................. 58

Figure 3.6 SEM images and Raman spectroscopy of GN deposited on the Cu network substrate. (a) and (b) SEM images of the GN on the Cu network substrate at low magnification; (c) and (d) SEM images of the GN on the Cu substrate at high magnification; (e) SEM image of a sample with 300 nm Cu after 120 s CVD growth, showing the morphology of the graphene on metal network; (f) Raman spectra measured at five different points marked with different colour dots in (e), reprinted from ref. [150], copyright © 2014 The Royal Society of Chemistry. ...................................................... 60

Figure 3.7 Raman spectra of the pure GN films transferred onto silicon wafers prepared by the two-step method as a function of growth time. The GN films were synthesized at 960 ℃ with 5 sccm $CH_4$ under the gas mixture of 200 sccm Ar/5 sccm $H_2$. The exposure time to carbon source for red, black and blue lines are 30 s, 90 s, 120 s respectively, reprinted from ref. [150], copyright © 2014 The Royal Society of Chemistry. ...................................... 61

Figure 3.8 SEM images of the pure GN films transferred onto Silicon wafers. (a), (b) and (c) the graphene networks formed at 960 ℃ after 30 s exposure time to the carbon source. (d), (e), and (f) the graphene networks formed at 960 ℃ after 120 s exposure time to the carbon source. The gas flowing rate ratio of Ar, $H_2$, and $CH_4$ is 200: 5: 5, reprinted from ref. [150], copyright © 2014 The Royal Society of Chemistry. ...................................... 62

Figure 3.9 (a) and (b) show the SEM images of the GN films transferred on the PDMS substrate; (c) Raman spectra of the PDMS-supported GN films with two different layer numbers (red: 2-4, black: 8-10); (d) optically transmittance of the 2-4 layers and 8-10 layers layer GN films on the PDMS substrate. (e) and (f) dependence of the two-electrode electrical resistance of GN films on the PDMS substrate at different bending angles in clockwise and anticlockwise directions, respectively, reprinted from ref. [150], copyright © 2014 The Royal Society of Chemistry......................................................................... 64

Figure 3.10 Tension test for the resistance *vs*. tension strain, reprinted from ref. [150], copyright © 2014 The Royal Society of Chemistry. ....................................................... 66

Figure 3.11 (a) and (b) Photograph of the GN films on PDMS and the transparent supercapacitor based on the GN films; (c) CV curves of a typical supercapacitor measured at the scan rate from 50 to 500 mV $s^{-1}$ ; (d) Galvanostatic charge/discharge (GCD) curve of the device measured at a constant current of 0.1 μA; (e) GCD curves of the device recorded at different applied currents; (f) variation of specific capacitance as a function of the applied current, reprinted from ref. [150], copyright © 2014 The Royal Society of Chemistry. ......................................................................................................... 67

Figure 4.1 Schematic illustration of 3D N-G-CNT-G structure. ...................................... 75

Figure 4.2 Photography of (a) silicon wafer, (b) AAO thin film, (c) spin-coated precursor and (d) N-G-CNT-G thin film via CVD growth. ............................................................ 76

Figure 4.3 SEM images of (a) free-standing N-G-CNT-G on AAO template; (b) cross view; (c) top view; and (d) two-layer N-G-CNT-G-AAO stacking structure. ........................... 77

Figure 4.4 TEM images of N-G-CNT-G with AAO template: (a), (b) and (c) top view in different magnification; (d) cross-section view of N-G-CNT-G with AAO template...... 79

Figure 4.5 TEM images of (a-b) N-G-CTN-G after removal of AAO template; (c) enlarged view of CNTs under the top graphene layer; (d) the thickness of the graphene layer (ca. 10 nm); (e-f) joint of graphene and CNT indicating covalent bonding. ............................... 81

Figure 4.6 (a) XRD and (b) Raman spectrum of N-G-CNT-G. ...................................... 81

Figure 4.7 Raman spectrum of G-CNT-G. ..................................................................... 82

Figure 4.8 (a) XPS survey spectra of N-G-CNT-G; HR-XPS spectra of (b) C1s and (c) N1s of N-G-CNT-G; (d) HR-XPS spectra of C1s of G-CNT-G. ........................................... 83

Figure 4.9 Raman spectra of G-CNT-G from (a) different growth temperature varied from 550 ℃, 700 ℃, 850 ℃, to 1000 ℃; (b) different growth time ranged from 30 min, 60 min to 120 min ; (c) different loading mass of precursor by varying the spinning rate; (d) the injected gas changed by only pure Ar (200 sccm), only pure $H_2$ (5 sccm), or by mixture of $H_2$ (5 sccm) and Ar (200 sccm)......................................................................... 85

Figure 4.10 N-G-CNT-G based supercapacitor: a) CV curves at the scan rate from 10 to 100 mV $s^{-1}$ ; (b) Galvanostatic charge/discharge (GCD) curves of the device recorded at different applied currents; (c) GCD curve at a constant current of 0.1 μA; (d) variation of specific capacitance as a function of the applied current................................................ 87

Figure 4.11 G-CNT-G based supercapacitor: a) CV curves at the scan rate from 10 to 100 mV $s^{-1}$ ; (b) Galvanostatic charge/discharge (GCD) curves of the device recorded at different applied currents; (c) GCD curve at a constant current of 0.1 μA; (d) variation of specific capacitance as a function of the applied current................................................ 88

Figure 5.1 Schematic illustration of synthesis of $MoS_2$-3DG......................................... 95

Figure 5.2 Photo of transparent $MoS_2$-3DG thin film on PDMS.................................... 96

Figure 5.3 (a) and (b) SEM images of $MoS_2$-3DG with AAO template under different magnification. ............................................................................................................. 96

Figure 5.4 SEM images of the free-standing $MoS_2$-3DG thin film after removal of AAO templates under different magnification. ... 97

Figure 5.5 (a) TEM images of $MoS_2$-3DG; (b) HRTEM image of $MoS_2$ nanosheet layers with orientation along (105) and graphene nanosheet layers with orientation along (210); (c) HRTEM image of $MoS_2$ nanosheet plane; (d) selected area electron diffraction (SAED) pattern. ... 99

Figure 5.6 Element (C, N, Mo, and S) mapping of $MoS_2$-3DG. ... 100

Figure 5.7 (a) Raman spectrum of 3DG; (b) Raman spectrum of $MoS_2$-3DG; (c) Raman spectrum of $MoS_2$; (d) XRD patterns of 3DG and $MoS_2$-3DG. ... 102

Figure 5.8 (a) XPS survey spectra of $MoS_2$-3DG and 3DG; high resolution XPS spectra of (b) C 1s, (c) Mo 3d, (d) S 2p. ... 103

Figure 5.9 SEM images of different volume of $MoS_2$ growing on 3DG ... 105

Figure 5.10 Raman spectra of thick $MoS_2$ decorated on 3DG, corresponding to the sample in Fig. 5.9d. ... 106

Figure 5.11 Galvanostatic charge and discharge curves of (a) $MoS_2$-3DG and (b) 3DG at a current density of 0.1A $g^{-1}$ measured in a voltage range from 0.02 to 3.0 V; (c) rate performance of $MoS_2$-3DG and 3DG; (d) Nyquist plots of $MoS_2$-3DG and 3DG; cycling performances of (e) $MoS_2$-3DG and (f) 3DG. ... 108

Figure 5.12 Electrochemical performance of thick-$MoS_2$ decorated 3DG: (a) Galvanostatic charge and discharge curves at a current density of 0.1A $g_{-1}$ measured in a voltage range from 0.02 to 3.0 V; (b) rate performance; (c) cycling performances; (d) Nyquist plots. 113

# Acknowledgment

I would like to thank my advisor, Professor Liming Dai, for his continuous guidance and support through the years of my stay at Case Western Reserve University. I appreciate the trust he gave to me in these years, especially the first two years when I was struggling with course, research and language. I am grateful to my committee members, Professor David Schiraldi, Professor Alex. M. Jamieson and Professor Clemens Burda for their constructive comments.

It has been a great pleasure for me to work in Prof. Dai's group. I would like to thank all the members for their kind support: Dr. Yonghua Chen, Dr. Xuli Chen, Dr. Long Qie, Dr. Liang Huang, Dr. Enoch Nagelli, Mr. Yachao Jin, Mr. Xiaoyi Chen. My Special thanks to Dr. Tao Chen, Dr. Min Wang and Dr. Chuangang Hu for excellent mentorship and help on my research work and thesis writing.

I am grateful to all the members of Macromolecular Science and Engineering Department for their support and regular feedback.

Finally, I would like to express my deepest thanks to my family for their unconditionally love and support, and to my husband, Dr. Xiaowei Zhang, without him, my life will be much harder.

# Tailored 3D Graphene-Based Materials for Energy Conversion and Storage

## Abstract

by

XUELIU FAN

With the rapid growth of energy electronics market, search for novel nanomaterials for efficient and eco-friendly energy conversion and storage has become an important task for manufacturers. Graphene, a two-dimensional carbon nanomaterial, has been widely applied in energy area due to its unique electric, chemical and physical properties. The atomic-scale and layered structures facilitate the integration of graphene into three-dimensional structures and heterostructures, thus opening a new world for rational design. This thesis consists of five chapters. After the first introduction chapter, the second chapter describes nitrogen-doped nanoporous graphene, which was synthesized on the zeolite-Y template with a tunable nitrogen content. The N-doped nanoporous graphene exhibits promising catalyzing performance in oxygen reduction reaction and is comparable to commercial Pt/C. In the third chapter, graphene networks was fabricated on sputtering-

coated Cu to form a freestanding thin film. The films can be easily transferred onto various substrates, such as PDMS and Si wafer, which can be integrated into flexible and transparent electrochemical-double-layer supercapacitors (EDLC) to offer an opportunity for fabricating the wearable devices. In the fourth chapter, a nitrogen doped graphene-CNT-graphene ordered structure is designed on the anodic aluminum oxide substrate, which, as electrodes in a double-layer supercapacitor, exhibits the high capacity and long-term stability. The completely controllable graphene-CNT-graphene structures provide a chance to achieve ordered three-dimensional graphene hybrids for the first time. Finally, in the last chapter, molybdenum disulfide decorated three-dimensional graphene heterostructure is realized. The hybrids can serve as anodes in lithium-ion battery to exhibit a high capacity, excellent rate capability, and long cycle life.

# Chapter 1

# Introduction

## 1.1 Introduction of three-dimensional (3D) graphene

Materials with high energy efficiency as well as excellent mechanical, chemical and electric properties are key factors to accelerate the advent of the sustainable energy world. There are continuous efforts on developing new materials for renewable energy conversion and storage system from both academia and industry[1]. The groundbreaking discovery of carbon nanomaterials in zero (0D), one (1D), two (2D) and three (3D) dimensions brought many potential and promising applications for energy conversion and storage purpose, such as clean and sustainable fuel cells, rechargeable high-capacity batteries, and wearable high-energy-density supercapacitors[2]. More particularly, the rise of graphene, a start of the atomic-thick materials, is shining new lights on the field[3].

Graphene is a two-dimensional monolayer of carbon hexagonal rings[4] (Fig. 1.1a). Owing to its unique structure, graphene possesses a fast carrier mobility (10,000 $cm^2 V^{-1} s^{-1}$)[5], half-integer quantum Hall effect[4], promising elasticity (1.0 TPa Young's modulus)[6], and high transparency[7] (Figs. 1.1c and d). Since Novoselov and co-workers exfoliated the single layer graphene by mechanical cleavage from graphite in 2004[5], various approaches to synthesize graphene have been intensively studied and now can be largely divided into two catalogs: bottom-up (*i.e.*, epitaxial growth[8] and chemical vapor deposition growth[9, 10]) and top-down (*i.e.*, exfoliation[11] or chemical reduction from graphite[12]). At the same time, the functionalization of graphene by doping heteroatoms and making the composites has also been explored to tune its properties[13-15].

In parallel with the intensive study of 2D graphene, materials with 3D architectures of graphene, named 3D graphene, with different structural layouts, such as foams, networks, and gels, were proposed[16, 17]. Moreover, some desired properties could be achieved by structural modification. The 3D graphene-based materials not only possess the intrinsic advantages of 2D graphene layers but also exhibit innovative functions. The synthetic routes of 3D graphene-based materials are based on but not limited to the above bottom-up and top-down approaches for 2D graphene synthesis. The preparation of 3D graphene with designed structures and the integration of 3D graphene into energy devices are two necessary steps. In this chapter, the synthesis and application of 3D graphene-based materials will be briefly introduced and followed by some prospects of future research.

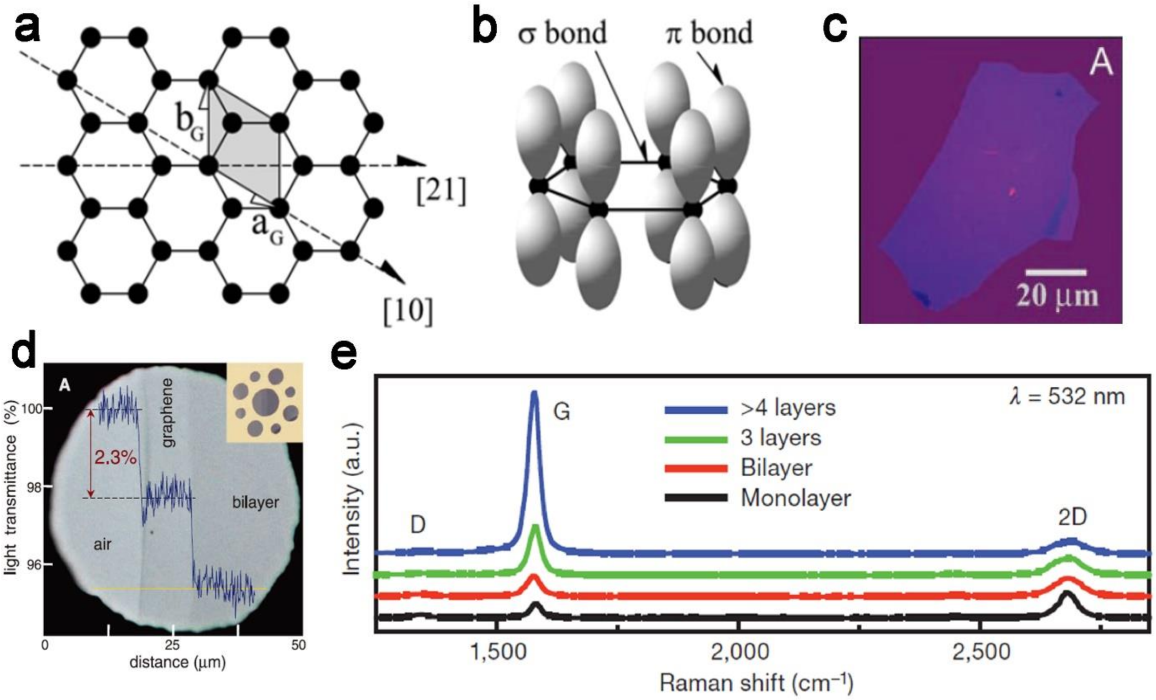

Figure 1.1 (a) Graphene hexagonal structure of identical carbon atoms, (b) schematic of in-plane σ bonds and π orbitals vertical to the basal plane[18], reprinted from ref. [18], copyright © 2008 IOP Publishing Ltd; (c) photograph of a multilayer graphene flake with thickness ~3 nm[5], reprinted from ref. [5], copyright © 2004 AAAS; (d) white light transmittance of single and bilayer graphene sheets[7], reprinted from ref. [7], copyright © 2008 AAAS; (e) Raman spectra (532 nm laser wavelength) of graphene[19], reprinted from ref. [19], copyright © 2009 Nature Publishing Group.

## 1.2 Structure of 3D graphene

Graphene has tightly packed carbon atoms with hybridized $sp^2$ bonding in honeycomb crystal lattice[4]. Each carbon atom has three strong in-plane σ bonds and one out-of-plane π bond[18] (Fig. 1.1b). 2D graphene can be wrapped into 0D fullerenes, rolled into 1D nanotubes, or stacked into 3D graphite at atomic-scale[3]. The 3D structure can be established from self-assembly of 2D graphene as well. The synthesis methods could influence the structure, quality, and functional groups of the graphene materials and further affect the electric and chemical properties for energy conversion and storage applications.

## 1.3 Synthesis of 3D graphene

Since the first isolated graphene is exfoliated and characterized[4, 20], the experimental approaches to synthesize 3D graphene have been developed with the aims of producing high-quality materials and simplifying the process to integrate into functional devices.

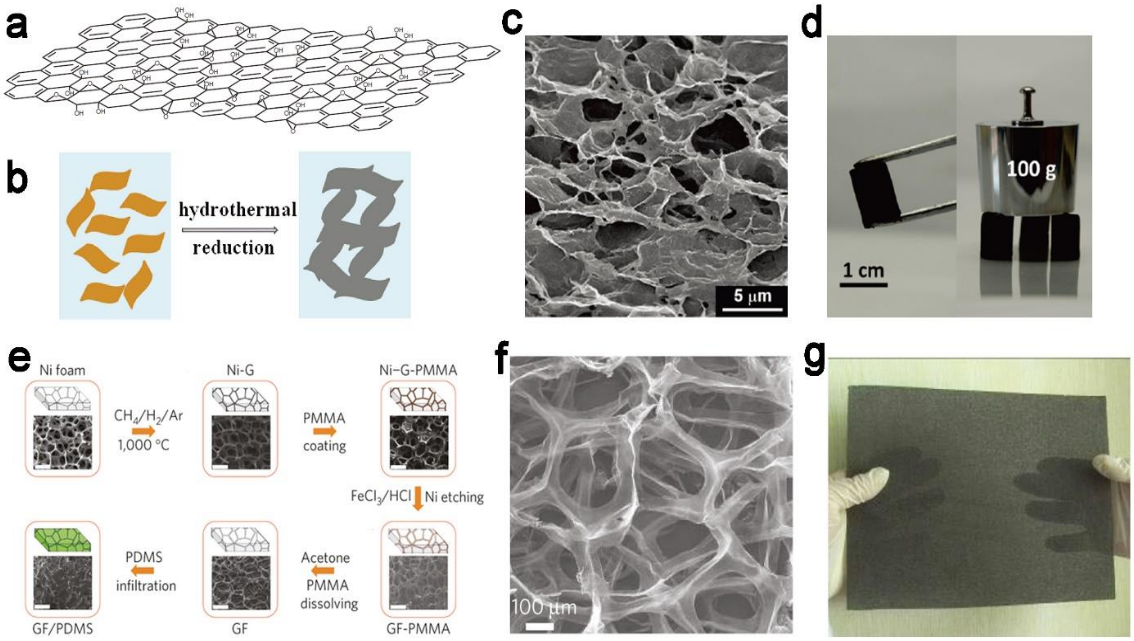

Figure 1.2 (a) Chemical structure of graphite oxide[21], reprinted from ref. [21], copyright © 2009 Nature Publishing Group; (b) schematic hydrothermal method for preparation of self-assembled graphene hydrogel (SGH), (c) SEM image of SGH interior microstructures, (d) photography of strong SHG[22], reprinted from ref. [22], copyright © 2010 American

Chemical Society; (e) synthesis of graphene foam (GF) by CVD method and transfer of graphene foam (GF) by etching Ni foams, (f) SEM image of GF, (g) photography of free-standing GF[23], reprinted from ref. [23], copyright © 2011 Nature Publishing Group.

### 1.3.1 Liquid-phase exfoliation

Ruoff's group first reported the fabrication of single-layer graphene by a solution method[21], in which the graphite was oxidized by Hummer's method[24] to form the AB stacking graphene oxide (GO) sheets[12] (Fig. 1.2a). The GO sheets have the epoxide and hydroxyl groups on the basal planes and the carbonyl and carboxyl groups at the edges. The static repulsion between the functional groups makes the GO nanosheet exfoliate from oxidized graphite and disperse in the solution[21]. With the reduction process, reduced graphene oxide (rGO) partially recovers its conjugated structure and constructs into 3D architecture by the weak Van der Waals attraction between the basal planes[17].

Various methods have been developed to reduce GO into electric conducting graphene, including chemical reduction[11, 12, 25, 26], hydrothermal approach[22, 27, 28], and electrochemical reduction[29-31]. The chemical reduction process can be carried out in both solution and gas phase via the reducing agents. For example, the graphene aerogel with 3D architectures via chemical reduction of hydrohalic acid (HI) showed a conductivity of 110 S $cm^{-1}$ and a density of 15 mg $cm^{-3}$ [26]. In contrast, the hydrothermal approach is simple and environmental-friendly to reduce GO aqueous dispersion into high electrically conductive 3D graphene hydrogel, in which randomly dispersed GO sheets were hydrothermally reduced and disordered stacked with hydrophobic and $\pi-\pi$ interactions[22] (Fig. 1.2b). In this process, water played an important role as reductant trapped into the graphene framework at the high temperature. The hydrothermally reduced graphene hydrogel consisted of 2.6% (wt%) graphene sheets and 97.4% (wt%) water with the strong mechanical properties (Figs. 1.2c and d). Similar to this hydrothermal approach, no reductant is required in the electrochemical reduction method as well. When the reducing voltage is applied on GO in the aqueous dispersion, the 3D graphene could be assembled with interpenetrating graphene microstructure[31].

The above methods of reduction of graphite oxide can be scaled up for industrial manufacturing, and graphene properties can be modified easily in the solution. However, the irreversible agglomerates and restacking of graphene sheets in 3D graphene from wet chemical approach cannot be avoided due to the π-π interaction. During oxidation and reduction process, the introduced defects could result in inferior electric properties. Therefore, a more effective and controllable way is adopted to fabricate high-quality 3D graphene to facilitate the industrial energy application, which is chemical vapor deposition.

### 1.3.2 Chemical vapor deposition

Chemical vapor deposition (CVD) belongs to the bottom-up approaches. In brief, the transition metal substrates (Cu[32], Ni[33], Ru[8], Pd[34], Ir[35], Co[36]) are exposed to gaseous, liquid or solid hydrocarbon source at high temperature. The hydrocarbon is then decomposed thermally, and carbon atoms are saturated into transition metal and precipitate from the surface upon the cooling process. Finally, graphene can form on the substrate.

The transition metal substrates play a critical role as catalysts in promoting graphene growth during the reaction. Crystal lattice match between the substrate and the graphene is required for nucleation and epitaxial growth of graphene. Large lattice mismatch will induce the production of the amorphous carbon[37].

For the CVD synthesis process, there are two growth mechanisms of graphene on transition metals: precipitation and surface reaction[38]. Nickel (Ni) and copper (Cu) are two common substrates for graphene growth on CVD, representing two different growth mechanism. For graphene growing on Ni[10], it shows a continuous segregation-precipitation process, in which graphene crystals grow on Ni (111) epitaxy and nucleate at Ni grain boundaries. After carbon atoms segregate, the highly defective graphitic structure forms at a fast cooling rate while few-layer graphene forms at moderate cooling rate. No carbon segregation is observed at slow cooling rate because of the high carbon solubility and diffusion in Ni. In contrast, the graphene growth on Cu is a surface reaction[32]. Cu has the low solubility and affinity of carbon due to the filled 3d-electron shell. As the hydrocarbon is decomposed, a thin layer of graphene is formed. Once no Cu catalyst surface is exposed to hydrocarbon, the growth of graphene ends.

CVD grown graphene has high quality. For example, the graphene synthesized by CVD on Cu foil can reach the size of 30 inches with a low electric resistance of 125 $\Omega$ $sq^{-1}$ [39]. CVD-produced graphene can be integrated into the 3D macroscopic structure by the selective substrate. For instance, 3D graphene foam is synthesized on Ni foam which serves as both template and catalyst (Fig. 1.2e) and demonstrates a high electric conductivity of 10 S $cm^{-1}$ as 0.5 wt% graphene foam/ poly(dimethyl siloxane) (PDMS) composites (Figs. 1.2f and g)[23].

Beside of large-scale synthesis of high-quality 3D graphene on transition metals, graphene can grow on the insulator substrate by CVD method to assemble into electronic devices directly. It has been reported about the continuous graphene film grown on dielectric substrates (*i.e.*, $SiO_2$[40], $Al_2O_3$[41], MgO[42, 43]). The graphene grown on sapphire showed a high carriers mobility 3000 $cm^2\ V^{-1}\ s^{-1}$ at room temperature which is comparable with the graphene grown on SiC (0001)[41].

3D graphene materials have exhibited various structures and morphologies by rational design of CVD process. For example, Yoon and co-workers fabricated 3D graphene nano-network on silica sphere using PVA as precursor and iron as a catalyst via CVD method[44]. The graphene network was achieved with a conductivity of 52 S $cm^{-1}$ and a high surface areas of 1,025 $m^2\ g^{-1}$. Ning and co-workers produced graphene nanomesh on gram-scale on the porous MgO layers at low temperature with a high specific surface area of up to 1654 $m^2\ g^{-1}$ [43]. By using enhanced plasma in CVD method, the 3D graphene walls could directly grow on $SiO_2$ substrate without catalysts and achieve comparable electric properties (sheet resistance of 198 $\Omega\ sq^{-1}$) to the graphene grown on transition metals[45].

## 1.4 Synthesis of 3D graphene/2D, 1D, 0D nanomaterial hybrids

3D graphene-based hybrids have been explored by incorporating and decorating with 2D (*i.e.*, metal dichalcogenide[46, 47], boron nitride nanosheet[48]), 1D (*i.e.*, carbon nanotube[49-52], metal/metal oxide nanowire/nanorod[53]), 0D (*i.e.*, fullerene[54], metal/metal oxide nanoparticles[55]) and quantum dots[56, 57]. Because of the heterostructure and unique properties, the multi-functional hybrids are very attractive for energy storage application, such as fuel cells, supercapacitors, and batteries. Inspired by 3D graphene synthesis, many approaches have been explored to synthesize 3D graphene-based hybrids. The conventional methods include hybrids from dispersion and chemical vapor deposition to fabricate heterostructures.

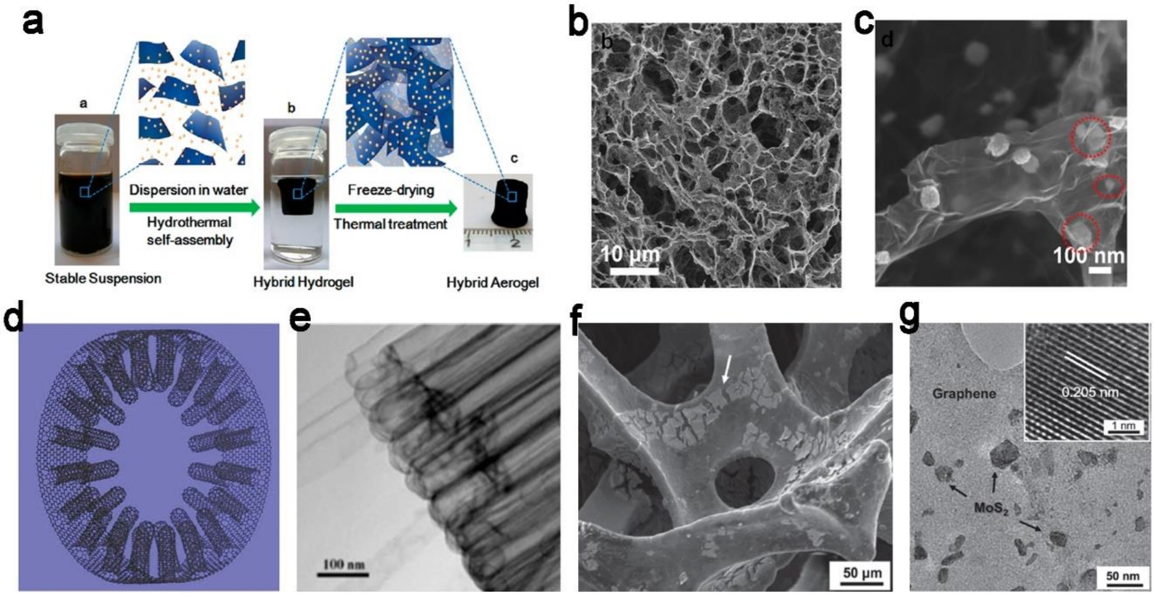

Figure 1.3 (a) Fabrication process for the 3D $Fe_3O_4$/N-doped graphene aerogels (N-GAs) by hydrothermal self-assembly and freeze-drying, (b) SEM image of 3D $Fe_3O_4$/N-GAs with macroporous structure, (c) $Fe_3O_4$ nanoparticles encapsulated in thin graphene layers[58], reprinted from ref. [58], copyright © 2013 American Chemical Society; (d) schematic of the 3D graphene-radially aligned CNT (RACNT) structure by CVD method, (e) TEM of RACNT with close end[59], reprinted from ref. [59], copyright © 2015 AAAS; (f) SEM image of $MoS_2$/3D graphene networks by CVD method, (g) HRTEM images of $MoS_2$ particles on the surface of 3D graphene networks[46], reprinted from ref. [46], copyright © 2013 John Wiley & Sons, Inc.

### 1.4.1 Solution-based method

Large-scale synthesis of 3D graphene-based hybrids can be achieved by multiple methods, including chemical deposition, electrodeposition, ultrasonication, Langmuir-Blodgett, and dip casting. The solution-based methods can achieve a high yield of 3D graphene-based hybrids and be applied for decorating 3D graphene with different dimensional materials, such as quantum dots, 0D fullerenes and metal nanoparticles, 1D CNTs and metal oxide nanowires, and 2D nanosheets.

Graphene quantum dots (GQDs) have quantum confined effects and edge effects. It can exhibit semiconducting properties when the sizes are down to <10 nm. Chen *et al.* reported the GQDs/3D graphene hybrids by electrodepositing ca. 2-5nm GQDs on the surface of 3D graphene homogeneously, which showed high-performance supercapacitors[57]. Dip casting is another efficient way to decorate quantum dots on 3D graphene. Cadmium sulfide quantum dots (CdS QDs) were distributed on graphene by dip casting for several times[56]. The graphene decorated with CdS QDs demonstrated an effective photoresponse.

Hydrothermal and chemical methods are commonly adapted for in-situ grown transition metal and metal oxide nanomaterials to enhance the electrochemical performance. The metal and metal oxides could be Au[60], Fe[61, 62], Co[63], Pd, $MnO_2$[53, 64], $Fe_3O_4$[58, 65, 66], $Co_3O_4$[67], $TiO_2$[59], *etc*, in forms of nanoparticles, nanowires, nanorods, and nanoplates. For example, $Fe_3O_4$ nanoparticles were decorated on 3D N-doped graphene through the hydrothermal process (Fig. 1.3a)[58]. The $Fe_3O_4$ nanoparticles with the size of 20-80 nm were encapsulated within the interconnected graphene layers (Figs. 1.3b and c), and the obtained aerogel showed efficient cathode catalyzing performance for the oxygen reduction reaction (ORR).

Although the products' quality is not as good as that made from CVD method, the solution-based method is an effective way for large-scale production of 3D graphene-based hybrids.

### 1.4.2 Chemical vapor deposition derived heterostructure

Graphene is a promising template for epitaxial growth of 1D and 2D nanomaterials via CVD due to the matched crystalline, such as CNT/G[49, 59], boron nitride (BN)/G[48], molybdenum disulfide ($MoS_2$)/G[68, 69], $WS_2$/G[47], *etc*.

For example, 1D vertically aligned CNTs (VACNTs) intercalated into the thermally expanded highly ordered pyrolytic graphite (HOPG) by CVD process and formed 3D pillared VACNT-G architectures[52]. Shortly after, 1D VACNTs could seamlessly grow on CVD graphene with conjugated covalent bonds characterized by the aberration-corrected STEM[49]. Although different 3D CNT/G hybrid architectures have been reported, the metal catalytic nanoparticles required for the CNT growth were likely hard to remove, which could affect the performance for energy applications. To address this issue, a novel one-step metal-free CVD method was reported to fabricate a radially aligned CNT (RACNT)/graphene hybrid material with seamless covalently C-C bonding between the graphene and RACNTs (Figs. 1.3d and e)[59]. The resultant RACNT/graphene hybrids had a large surface area of 526.9 $m^2$ $g^{-1}$ and exhibited minimized interfacial electrical/thermal resistances, according to the molecular dynamic simulations.

2D materials, such as BN and layered transition metal dichalcogenides (TMDCs), can also be decorated on graphene via a CVD method. 2D insulator BN and graphene are structure analogs, and the BN-graphene hybrids have been synthesized in the form of BN-graphene in-plane junction or inter-plane hetero layers[70]. As BN has a large bandgap and smooth surface at atomic-scale, it served as an excellent dielectric or separation layers in BN-graphene hybrids based electronic devices. The epitaxial growth of layered TMDCs on graphene has attracted more attention as the TMDCs/G hybrids can be large-scale synthesized and widely used for electrocatalysis and batteries with tremendous performances[71]. For example, $MoS_2$, a typically layered transition metal dichalcogenide, has the layered structure held by the weak Van der Waals forces[20] and shows a great lithium storage capacity in lithium-ion batteries[72] and a highly efficient catalyst activity for hydrogen evolution reaction[73]. Also, Cao and co-workers[46] have reported that $MoS_2$ decorated 3D graphene foams could be fabricated by a simple CVD method (Figs. 1.3f and g). The $MoS_2$/G heterostructure was characterized by Raman spectrum with $E_{2g}^1$ peak at 383 $cm^{-1}$ and $A_{1g}$ peak at 405 $cm^{-1}$ for $MoS_2$ and G peak at 1582 $cm^{-1}$ for graphene. Coupled with the high electric properties of graphene, the obtained hybrids exhibited highly reversible capacities and high rate capabilities, which could be used as an anode material candidate in lithium-ion batteries too.

## 1.5 Functionalization of 3D graphene

Graphene has zero band gap with excellent electron mobility and can be taken as either metal or semiconductor material[4]. For energy application, functionalizing graphene is an efficient way to open the band gap and tune the mobility so that the electric and chemical properties can be modified to enhance the performance, such as catalyzing efficiency and energy storage capacity[13].

In general, two pathways were studied to functionalize graphene (Fig. 1.4). The first is covalent functionalization, in which heteroatoms are induced in $sp^2$ structure through covalent bonding in graphene hexagonal lattice and create defects. One of the common covalent functionalization is to substitute carbon atoms in graphene lattice by nitrogen (N), boron (B), sulfur (S) or phosphorus (P) atoms, which is also called heteroatoms doping[14]. The second is non-covalent functionalization. Various chemical moieties are also introduced on the graphene via π–π interaction and Van der Waals forces without changing the graphene lattice structure[15].

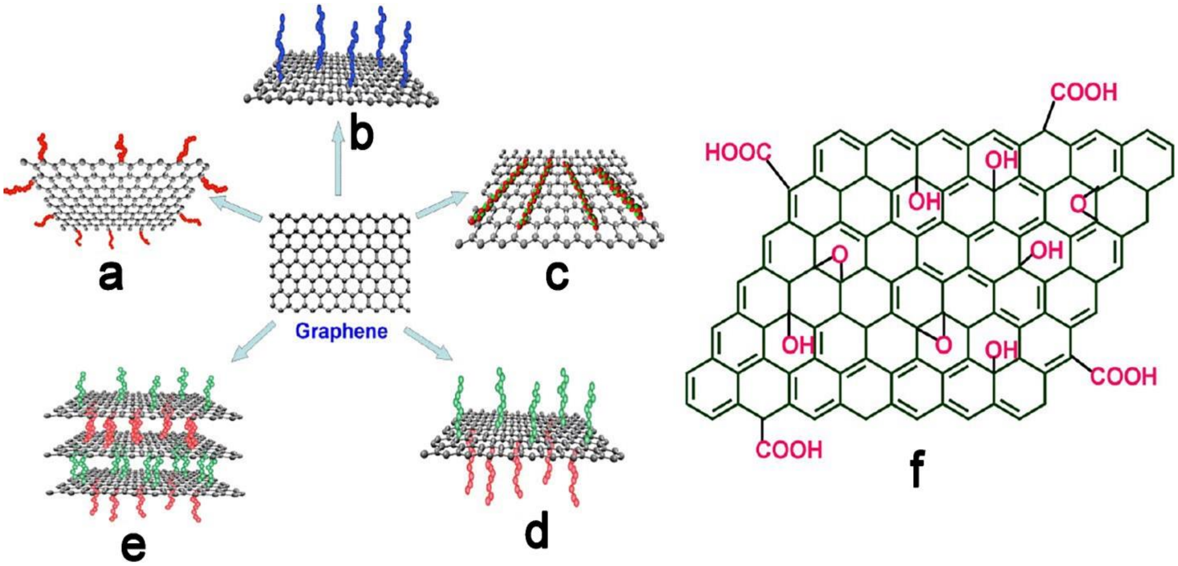

Figure 1.4 Functionalization possibilities for graphene: (a) edge-functionalization, (b) basal-plane-functionalization, (c) non-covalent adsorption on the basal plane, (d) asymmetrical functionalization of the basal plane, and (e) self-assembling of functionalized graphene sheets; (f) chemical structure of graphene oxide[13], reprinted from ref. [13], copyright © 2012 American Chemical Society.

### 1.5.1 Heteroatom doping

N and B are two of the most common heteroatoms for doping graphene. The electronegativity of heteroatoms such as B (2.0) and N (3.0) are different from that of C (2.5). Thus doping of N or B can cause the charge polarization to increase the carrier concentration[74]. Although S-doping cannot bring obvious polarization effect due to the close electronegativities of S (2.6) and C, the covalent bonding of S at graphene edges and the Stone-Wales defects can induce the redistribution of spin densities on graphene lattice[75]. Beside polarization phenomena arising from the different electronegativity of P (2.2) to C, P doping can also cause the transform of $sp^2$ C into $sp^3$ hybridization by strong hybridization between P 3p and C 2p orbitals, and generate the structural deformation[14]. In general, heteroatom doping can provide active sites, enhance the carrier mobility, and modify the electrochemical properties of graphene materials.

The heteroatom-doping process can be conducted either by in-situ doping during synthesis of graphene or post-treatment of graphene with precursors containing heteroatoms[13]. In the in-situ doping process, the carbon sources mixed with heteroatom-containing precursor are introduced to dissociate and recombine into heteroatom-doped graphene. For example, the synthesis of in-situ B, N-co-doped graphene foam has been reported with the extraordinary performance of oxygen reduction reaction[76]. The high-resolution XPS of N1s and B1s spectrum showed the B-N bonding as a dominant component in the graphene structure. The post-treatment doping for graphene often leads to the surface functionalization. For instance, N-doped rGO was fabricated by annealing rGO under ammonium at 800 °C for 1 hour[77]. The N-doping-induced defects in 3D mesoporous structures endowed the N-doped graphene foam with a high capacity as anodes for sodium ion batteries.

### 1.5.2 Non-covalent functionalization

Noncovalent functionalization is an attractive method to modify graphene with functional groups and maintain its natural graphene lattice structure. The noncovalent functionalization of graphene is based on $\pi$–$\pi$ interactions, van der Waals forces or electrostatic force with aromatic species or organic molecules[15].

The functionalized 3D graphene materials have demonstrated unique properties and been used in energy systems. The polymers with aromatic rings can functionalize graphene homogeneously via $\pi$–$\pi$ interactions. Yu *et al.* reported polyaniline nanocone was vertically aligned with 3D graphene network by electrodeposition method[78]. As the electrodes of supercapacitors, the PANI-3D graphene materials improved its surface and provided an unblock diffusion path for electrolyte ions. Biomolecules can also functionalize graphene as the manner of polymer molecules. For example, Xu *et al.* reported 3D self-assembling GO/DNA hydrogen was synthesized by a simple hydrothermal approach, in which in-situ-formed ssDNA chain bridged GO sheets via strong noncovalent interactions[79]. The obtained GO/DNA hydrogel showed the strong mechanical properties with a high environmental stability and dye-loading capacity.

## 1.6 Energy conversion and storage application of 3D graphene-based materials

The expanded market for electric vehicles (EVs) offers huge opportunities to tackle the challenges of the energy crisis when combined with an environmental-friendly and sustainable power source such as fuel cells, supercapacitors, and lithium-ion batteries.

Fuel cell is a clean power source to convert chemical energy to electric energy by reducing oxygen from air or hydrogen peroxide and oxidizing hydrogen or other fuels[80] (Fig. 1.5a). On the other hand, supercapacitor is one kind of energy storage device, and it harvests energy via either ion adsorption or surface redox reactions, based on which supercapacitors are divided into electrochemical double-layer capacitors (EDLC) (Fig. 1.5b) and pseudocapacitors[81]. Lithium ion battery has occupied the market as the most common power source, in which charge-transfer is generated via the lithium-ion intercalation/deintercalation in the anode/cathode with redox reactions[82] (Fig. 1.5c). Although the operation mechanisms of the energy conversion and storage are different, all of them are based on the electrochemical principles. Therefore, the electrochemical properties of the materials in electrodes can significantly determine the performance of these energy devices.

In this section, we will focus on 3D graphene-based materials for fuel cells, supercapacitors, and lithium ion batteries.

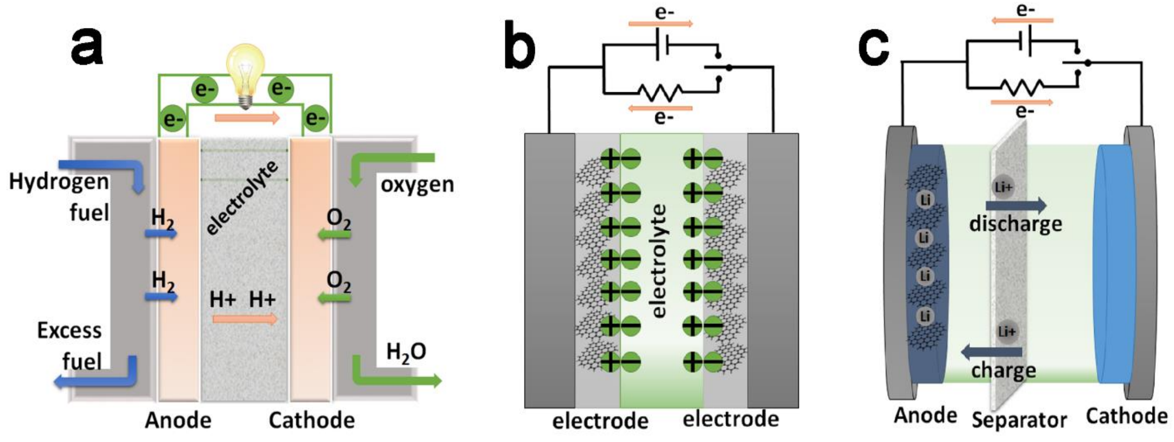

Figure 1.5 Schematic principles of (a) fuel cell, (b) electrochemical double-layer supercapacitor, and (c) lithium-ion battery.

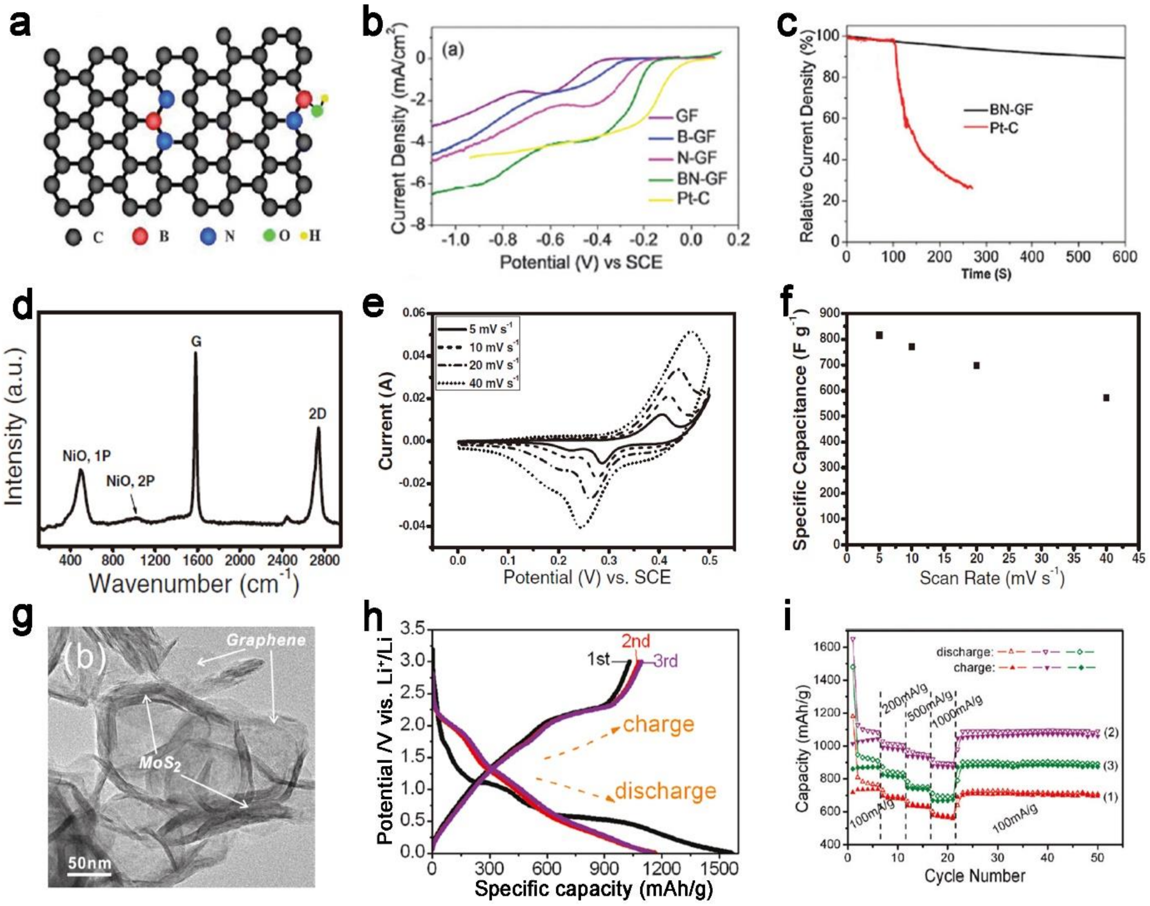

Figure 1.6 (a) Schematic structure of B,N-co-doped graphene, (b) rotating disk electrode voltammograms of the undoped graphene foam (GF), B-doped GF, N-doped GF, and B,N-co-doped GF based electrode, and the commercial Pt/C based electrode in an oxygen saturated 0.1 M KOH solution, (c) CO tolerance test of B,N-co-doped GF and the commercial Pt/C based electrode[76], reprinted from ref. [76], copyright © 2013 Royal Society of Chemistry; (d) Raman spectrum of NiO/graphene composites, (e) cyclic voltammetry curves and (f) specific capacitance of NiO/graphene composites[83] , reprinted

from ref. [83], copyright © 2011 John Wiley & Sons, Inc; (g) TEM image of microstructure of $MoS_2$/G (1:2) composite, (h) charge and discharge curves of $MoS_2$/G (1:2) composite, (i) rate capability of $MoS_2$/G (1:2) composites at different current densities[68], reprinted from ref. [68], copyright © 2011 American Chemical Society.

### 1.6.1 Fuel cell based on 3D graphene cathode

Fuel cell is a clean and sustainable power to produce electricity. Fuel cell consists of three parts: anode, cathode and separation membrane. The hydrogen is injected from the anode and electrochemically split into electrons and protons. The electron will flow through an external circuit to provide electricity while the protons will diffuse toward the cathode to combine with the reduce oxygen into water, as shown by the following reactions[80]:

In acidic

$$O_2 + 2H_2O + 4e^- \rightarrow 4OH^- \tag{1-1}$$

$$O_2 + H_2O + 2e^- \rightarrow HO_2 + OH^- \tag{1-2}$$

In alkaline

$$O_2 + 4H^+ + 4e^- \rightarrow 2H_2O \tag{1-3}$$

$$O_2 + 2H^+ + 2e^- \rightarrow 2H_2O_2 \tag{1-4}$$

Oxygen reduction reaction (ORR) on the cathode could determine fuel cell's efficiency[84], and noble metals, such as platinum (Pt), have been widely used as cathode materials. As the high cost and limited reserves of the noble-metals hindered the commercial manufacture of renewable fuel cells, 3D graphene-based catalysts have been developed to outperform the conventional carbon black supported platinum (Pt/C) catalysts with a low cost and high efficiency.

Early research focused on graphene with various morphologies as Pt support for fuel cell. For example, Geng *et al.* have reported the preparation of nanoflower-like N-doped graphene via the hydrothermal method[85]. The obtained nanoflower-like N-doped graphene showed a higher durability than commercial carbon black as a Pt support due to the active sites by N-doping and the high stability from highly graphitization.

Later, the novel metal/graphene hybrids were developed to enhance the electrocatalytic activity. Guo *et al.* have synthesized 3D Pt-on-Pd bimetallic nanodendrites/graphene nanosheets hybrids via wet-chemical approaches[86]. The hybrids demonstrated the higher electrocatalytic activity toward methanol oxidation reaction than the platinum black (PB) and commercial Pt/C catalysts.

To further reduce the cost of the fuel cell, non-precious metal (oxide) decorated 3D graphene were investigated as catalysts in fuel cells[58, 87-88], showing promising ORR activities. A study on $Fe_3O_4$ nanoparticles decorated 3D N-doped graphene aerogels was carried out by Wu and co-workers[58]. The aerogel had a high specific surface area of 110 $m^2$ $g^{-1}$ with meso- and macro- porous feature and exhibited a higher current density, the lower $H_2O_2$ yields and better durability than those of Pt/C in alkaline electrolytes for ORR.

The recent intensive research efforts were devoted to replacing metal-based electrodes in fuel cells rather than reducing the usage. In this regard, metal-free catalysts were studies to cut down the cost substantially and improve the efficiency of fuel cells[74]. Since researchers found that the charge redistribution via doping can promote ORR process by creating charged sites ($C^+$, $N^-$, $B^+$) beneficial for oxygen adsorption[84], heteroatom-doped graphitic carbon materials have been considered as an alternative ORR catalyst.

Following the discovery of N-doped CNTs worked as an efficient metal-free ORR catalyst[89], N-doped graphene thin film was synthesized by CVD method and exhibited a three-time-higher current density than the commercial Pt/C and a long-term stability for 200,000 cycles in alkaline electrolyte[90]. Further research showed CVD grown N, B-co-doped graphene foam with the better performance than B, and N-doped graphene in ORR[76], as seen in Figs. 1.6b and c. The enhancement of electrocatalytic activities were attributed to not only N and B atoms doping with more active sites for charge transfer, but the synergistic interaction between adjacent N and B atoms that could reduce the bandgap to facilitate ORR process (Fig. 1.6a). Therefore, heteroatom-doped graphene paves the way for low-cost, high-efficient, and commercialized fuel cells.

### 1.6.2 3D graphene based electrodes for supercapacitors

Since one of the high surface area carbons were reported[91], researchers have devoted significant efforts to develop supercapacitors and extended the applications into portable power supplies and electrical vehicles. As mentioned earlier, supercapacitor consists of two electrodes and a separator that only allows electrolyte ions to permeate (Fig. 1.5b). In the charging state, positive and negative ions move toward the anode and cathodes respectively and accumulate at interfaces between the solid electrode and the electrolytes. The resultant potential difference can create current in the discharging state[80].

Various carbon materials are frequently used as the electrode material for supercapacitors. Among them, 3D graphene-based materials based supercapacitors have achieved high performance owing to their large surface area and promising electric and mechanical properties[16]. Furthermore, 3D graphene can be integrated into flexible all-solid-state supercapacitors, which offer an opportunity for fabricating portable electronic devices[92].

Using 3D graphene-based materials as electrodes can avoid the restacking of graphene sheets and promote the electrolyte diffusion within the active materials. For example, the graphene hydrogel by hydrothermal method had the large surface area of ∼414 $m^2$ $g^{-1}$ [93]. The graphene hydrogel based flexible solid-state supercapacitor exhibited the gravimetric specific capacitance of 185 F $g^{-1}$ at a current density of 1 A $g^{-1}$, the excellent rate capability and the cycling stability after 10000 charge/discharge cycles.

Heteroatom doping of 3D graphene can facilitate the charge transfer and thus enhance the electrochemical performance. Wu and co-workers reported B, N co-doped graphene aerogel (BN-GAs) based all-solid-state supercapacitors, which showed a higher specific capacitance (62 F $g^{-1}$) than that of N-doped GAs (190 F $g^{-1}$) and B-doped GAs (228 F $g^{-1}$)[94], indicating that heteroatoms contributed to the improvement of performance.

The 3D graphene hybrids can also improve the performance of supercapacitors by combination with pseudo-capacitive materials, including metal oxide[67, 83, 95, 96] and conducting polymer[78, 97, 98]. For example, after electrochemical deposition of NiO film on graphene foam from CVD[83], the NiO/graphene foam (GF) materials showed graphene peak and NiO peak in Raman spectrum in Fig. 1.6d. The NiO/GF based supercapacitor demonstrated a high specific capacitance of 816 F $g^{-1}$ at 5 mV $s^{-1}$ (Figs. 1.6e and f), which was much higher than NiO-based supercapacitor (305 F $g^{-1}$ at 5mV $s^{-1}$). The enhancement can be attributed to the large surface area and the excellent electric conductivity of 3D graphene foam. Dong and co-workers reported graphene-polyaniline (PANI) hybrids by the in-situ polymerization of aniline monomer on the CVD graphene foam[98]. The hybrids showed the specific capacitance of 346 F $g^{-1}$ at 4 A $g^{-1}$. For the comparison, 3D graphene foam based supercapacitor had the specific capacitance of 36 F $g^{-1}$ at 4 A $g^{-1}$, suggesting the hybrids based supercapacitors have integrated the function of the electrical double-layer capacitor (EDLC) and the pseudocapacitor.

Carbon allotropes nanomaterials based supercapacitors are also developed as they provide fast electron transport via covalent bonding, smooth ionic conducting channels, and light weight. For example, 3D graphene/CNT carpets based microsupercapacitors demonstrated the specific capacitances up to 2.16 mF $cm^{-1}$ in 1 M $Na_2SO_4$ aqueous electrolyte[99]. Later, one-step synthesized 3D graphene-CNT hollow fibers were used as electrodes for fiber-shaper supercapacitor[59]. The device showed the high area and length capacitance of 89.4 mF $cm^2$ and 23.9 mF $cm^{-1}$, respectively, and outperformed the corresponding record fiber-like supercapacitors.

Therefore, 3D graphene-based materials are a promising candidate for supercapacitors. By rational design of morphology and properties, 3D graphene-based supercapacitors can achieve outstanding performance.

### 1.6.3 3D graphene-based anode for lithium-ion batteries

Lithium-ion battery (LIB) has become one kind of frequently used power source for portable electronics. The fast development of electric vehicle also facilitated the demand for LIB[1]. LIB consists of cathode, anode, porous membrane permeable for lithium ions and electrolyte (Fig. 1.5c). In the charging state, lithium ions are deintercalated from the cathode, diffuse across the porous membrane, and intercalated into the anode. Conversely, lithium ions are deintercalated from anode and back to cathode in the discharge state[100].

To realize high energy and power density and fast charge/discharge, considerable efforts are devoted to find the alternative materials as anodes in LIB and to replace commercial graphite which has a low theoretical capacity of 372 mAh $g^{-1}$ [101]. For this purpose, 3D graphene-based materials have widely used as anode materials due to their controllable morphology with large surface area, tunable electrochemical properties, and natural excellent electric and mechanical properties.

The theoretical capacity of graphene is 744 mAh $g^{-1}$ when the lithium ions are intercalated and attached on both sides of graphene sheets to form $Li_2C_6$[102]. By change of morphology, the graphene-based anodes in LIB can achieve an improved performance with increased active sites for lithium insertion. For example, Lian and co-workers reported wrinkled paper-like graphene by thermal exfoliation method[103]. The obtained materials had the large specific surface area of 492.5 $m^2$ $g^{-1}$ and showed the high reversible capacity of 1264 mAh $g^{-1}$ at a current density of 100 mA $g^{-1}$ and the long cycle stability as an anode in LIB.

Heteroatom doping is an effective way to enhance the performance of graphene-based LIB. N-doped graphene nanosheets with a crumpled structure had shown the higher reversible capacity and the greater long cycle life compared to the graphene nanosheet as an anode in LIB, which ascribed to the increase of defect sites for lithium ion intercalation by N-doping[104].

Si[105], Ge[106], Sn[107] and many metal/metal oxides[27, 108, 109] also act as active materials of anodes to replace conventional graphite. Those materials show the high theoretical lithium ion capacities, but they suffer from the poor conductivity and the unstable structure during charge/discharge. Therefore, Si, Ge, Sn or metal oxides decorated 3D graphene-based materials are developed to enhance the LIB performance regarding lithium storage capacity and cycling stability. In brief, graphene layers can prevent the structure deterioration as a solid matrix, offer excellent conductivity for electron transport, and provide enough space for electrolyte diffusion with large surface area. For example, $Fe_3O_4$ nanospheres ($Fe_3O_4$ NSs) were encapsulated by the continuous graphene layers and formed the $Fe_3O_4$ NSs/3D graphene foam structures that prevented the volume change and the aggregation of $Fe_3O_4$ NSs during the charge/discharge process[110]. With the highly conductive network of 3D graphene foam, the hybrids delivered a high reversible capacity of 1059 mAh $g^{-1}$ at a current density of 93mA $g^{-1}$ over 150 cycles and the excellent rate capability (363 mAh g-1 at 4800 mA $g^{-1}$).

2D transition metal dichalcogenides (TMDCs)/graphene hybrids are also studies as anode materials. As TMDCs have the similar structure of graphene, they can stack on graphene surface to facilitate the electron transport and ion diffusion. The 2D $MoS_2$ layer was in-situ synthesized on the graphene surface to form the hybrids with 3D architecture by a hydrothermal process and annealing[68], as seen in Fig. 1.6g. The prepared $MoS_2$/G hybrids showed excellent electrochemical performances as anode materials for LIB with the high rate capability and the high specific capacity of ~1100 mAh $g^{-1}$ at a current of 100 mA $g^{-1}$ in Fig. 1.6h, far greater than the theoretical capacity of bulk $MoS_2$ (only 167 mAh $g^{-1}$), and with the excellent cycling stability (Fig. 1.6i).

Further improving the performance of 3D graphene-based LIB may depend on the rational design of morphology and structure, a tunable increase of electrochemically active sites, as well as fully explore of intrinsic properties of active materials.

## 1.7 Research objective

The materials and technologies in energy conversion and storage areas have been rapidly developing. In particular, 3D graphene-based materials brought promising applications in energy devices, such as fuel cells, supercapacitors, and lithium-ion batteries, owing to their excellent electric, chemical, and thermal properties and controllable structure. However, we are still facing various challenges. First, the structure and morphology of 3D graphene-based materials cannot be completely controlled during the synthesis, particularly in terms of the well-defined structure, ideal pore size, and specific surface area. Second, novel approaches to fabricate 3D graphene-based hybrids are demanded to achieve tunable heteroatom doping and designable heterostructure. Third, the growth mechanism of 3D graphene-based materials is not clear, which would hinder the synthesis of optimal materials. Finally, it is in urgent need of applying the 3D graphene-based materials for energy conversion and storage devices with outstanding performance mass-production. Thus, it is necessary to carry out further research on advanced approaches for the synthesis of 3D graphene-based materials for energy conversion and storage applications.

# Chapter 2

# Zeolite-Y-templated N-doped nanoporous graphene for oxygen reduction reaction and lithium ion batteries

## 2.1 Introduction

Three-dimensional (3D) graphene has attracted increasing interest in many critical applications, such as gas separation, oil adsorbents, chemical sensors, and energy conversion and energy storage due to its high specific surface area and high electrical conductivity. Since the first time nitrogen doped (N-doped) graphene was reported to improve the electrochemical performance[90], heteroatom (N, B, S, P, *etc*.) doping of 3D graphene has been widely studied to modulate their electrical and chemical properties[13]. For example, N-doped graphene foams have been used as anode in sodium-ion batteries and exhibited a high initial reversible capacity (852.6 mAh $g^{-1}$)[77], and B,N co-doped graphene aerogels based all-solid-state supercapacitors have achieved high specific capacitance (≈62 F $g^{-1}$)[94]. In addition, N and S co-doped graphene mesh foams via hydrothermal method exhibited excellent electrocatalytic activities for oxygen reduction reaction[111]. Therefore, heteroatoms doped 3D graphene with improved electrochemical properties can be widely used in energy conversion and storage.

Some methods have been reported for the synthesis of N-doped 3D graphene, such as sol-gel process followed by thermal treatment (hydrothermal method)[112-115], direct calcination by heteroatom-containing precursor (carbonization)[62, 116] and template-assisted chemical vapor deposition (CVD) with heteroatom-containing gas flows ($NH_3$, $H_2S$, *etc*.)[59, 117]. The sol-gel process or the direct calcination method can easily obtain large-scale samples with a high doping content. However, it is not effective enough to control the morphology and achieve a high conductivity. CVD method is such a promising and inexpensive approach to synthesize large-scale and high-quality doped 3D graphene. The obtained graphene can not only has a controlled specific surface area but also possesses a structural integrity. Furthermore, the graphene produced by the template-assisted CVD shows better electrical properties than those of the graphene obtained from the hydrothermal and carbonization methods. Considering the ever-increasing need for high-quality porous graphene, low-cost and controllable CVD growth templates are demanded for the synthesis of 3D doped graphene.

Zeolites are one of aluminosilicate materials with well-defined nano space[118] that provides an ideal opportunity to fabricate a novel and order microporous graphene in the confined space of zeolite channel. Zeolites X, Y, β, L, and ZSM-5 have been used as a hard template to prepare carbon nanotubes (CNTs)[119-121], fullerenes[122, 123], and other porous carbon materials[124-127]. Graphene can grow inside the interconnected pores along the smoothly curved surface and form the seamless 3D nanoporous structure. Although recent studies of graphene synthesis on zeolite have achieved by embedding metal catalyst into the pores[128, 129], the removal of metal catalysts would damage the graphene structure, and potential applications of zeolite-templated graphene materials in catalysis and batteries have rarely been reported to date.

Herein, the synthesis of N-doped nanoporous graphene (N-NPG) is reported by zeolite Y-templated CVD technique, which combines the advantageous features of a high surface area, abundant active sites of easy access, and favorable mass transport for electrolytes. As a result, the newly prepared N-NPG shows highly efficient catalytic activity towards oxygen reduction reaction in alkaline media with a high kinetic limiting current, outstanding stability and tolerance to methanol crossover effect with respect to the commercial Pt/C electrodes. On the other hand, as an anode material for lithium ion batteries, N-NPG also exhibits an excellent high initial discharge/charge capacity of ~2439/1237 mAh $g^{-1}$ at 0.1A $g^{-1}$, excellent rate capability, and long cycling stability.

## 2.2 Experimental section

### 2.2.1 Preparation of NPG and N-NPG

Zeolite Y-ammonium ($SiO_2$:$Al_2O_3$ = 5.1:1, surface area = 925 $m^2$ $g^{-1}$,) was purchased from Alfa Aesar. 2g zeolite-Y powder was put in a quartz boat in the quartz tube for 30 minutes under pure argon (Ar, 99.99% purity, Airgas) with the gas flow rate of 200 standard cubic centimeters per minute (sccm) at room temperature and then heated up by 3 ℃ $min^{-1}$ until 700 ℃. The NPG samples were obtained by a series of heat-treatments at 700 ℃ for 10 min under the reaction gas mixture of acetylene ($C_2H_2$, 99.6% purity, Airgas), hydrogen ($H_2$, 99.999% purity, Airgas), and Ar with the gas flow rate of 10, 10 and 200 sccm respectively. The N-NPG was obtained by heat-treatment at 700 ℃ for 10 minutes under the reaction gas mixture of ammonia ($NH_3$, 99.995% purity, Airgas), $C_2H_2$, and Ar with the gas flow rate of 10, 10 and 200 sccm, respectively, followed by purging with a gas flow of $NH_3$ and Ar only for another 30 min. All the samples went through the rapid cooling process under Ar subsequently.

### 2.2.2 Template removal

The zeolite-Y templated NPG or N-NPG powder was washed with in 48 wt% hydrofluoric acid (HF, Sigma-Aldrich, 48 wt% in $H_2O$) overnight, refluxed at 100 ℃ by 1 M hydrochloric acid (HCl, 37%, Sigma-Aldrich), centrifuged and washed with deionized water for several times to remove the zeolite templates completely.

### 2.2.3 Characterization

Scanning electron microscope (SEM) images were collected from Hitachi S-5200 and transmission electron microscope (TEM) images from FEI Tecnai G2 T20 (120 kV). Raman spectra were obtained by Raman spectrometer (Renishaw) with a 514 nm laser. The X-ray powder diffraction (XRD) patterns were obtained on a Bruker D8-advance X-ray powder diffractometer with Cu Kα radiation source (λ= 1.54 Å). X-ray photoelectron spectroscopy (XPS) measurements were carried out on a PHI-5300 ESCA spectrometer (PerkinElmer) using 300W Al Kα radiation. Thermogravimetric analysis (TGA) was conducted on a TGA Q50 (TA instrument) instrument with a heating rate of 10 °C $min^{-1}$. Brunauer-Emmett-Teller (BET) was performed on an AutoSorb iQ2 (77K) in the relative pressure range from 0.05 to 0.3 to collect the specific areas data, and the pore size distribution curves were obtained by computing the desorption branches of the isotherms with Barrett, Joyner, and Halenda (BJH) method.

### 2.2.4 Electrocatalytic activity evaluation

2 mg N-NPG powder was dispersed in the solution containing 400 μl ethanol and 40 μl Nafion uniformly by ultrasonic dispersion machine. 10 μl mixture was drop cast on the 0.2 $cm^2$ glass-carbon disk electrode for rotating ring-disk electrode (RRDE) voltammogram measurements.

Oxygen reduction reaction measurements were performed on a computer-controlled potentiostat (CHI 760C, CH Instrument, USA) with a three-electrode cell equipped with gas flow systems. N-NPG samples were used as a working electrode, an Ag/AgCl (0.1 M KCl-filled) electrode as a reference and a platinum wire as counter electrode.

### 2.2.5 Lithium-ion battery measurements

The electrodes were prepared by mixing N-NPG with acetylene black carbon and PVDF with a mass ratio of 75:15:10 respectively. Then the mixture was ground into slurry with N-methyl-2- 3 pyrrolidone (NMP), cast on Cu foil and dried overnight at 90 ℃. The obtained electrodes were integrated into CR2032 coin cells. The battery assemble process was conducted in the Ar-filled glove box by stacking N-NPG based electrode, a porous polypropylene film as separator, Li foil as the counter electrode and reference electrode. The electrolyte is 1 M $LiPF_6$ in a mixture of ethylene carbonate (EC), diethyl carbonate (DEC) and dimethyl carbonate (DMC) (1:1:1).

## 2.3 Results and discussion

The preparation procedure details for N-NPG are depicted in the experiment section. Briefly, the zeolite-Y templated N-NPG was synthesized by CVD with a mixture gas of

$C_2H_2$, $NH_3$ and Argon (Ar) at 700 °C for 10 minutes, followed by flowing of $NH_3$ and Ar only for another 30 min. The templates were removed by HF and HCl solution etching, followed by repeated centrifuge and washing with deionized water. As a reference, pure graphene was prepared under the same CVD growth condition without nitrogen doping. The corresponding samples were designated as NPG.

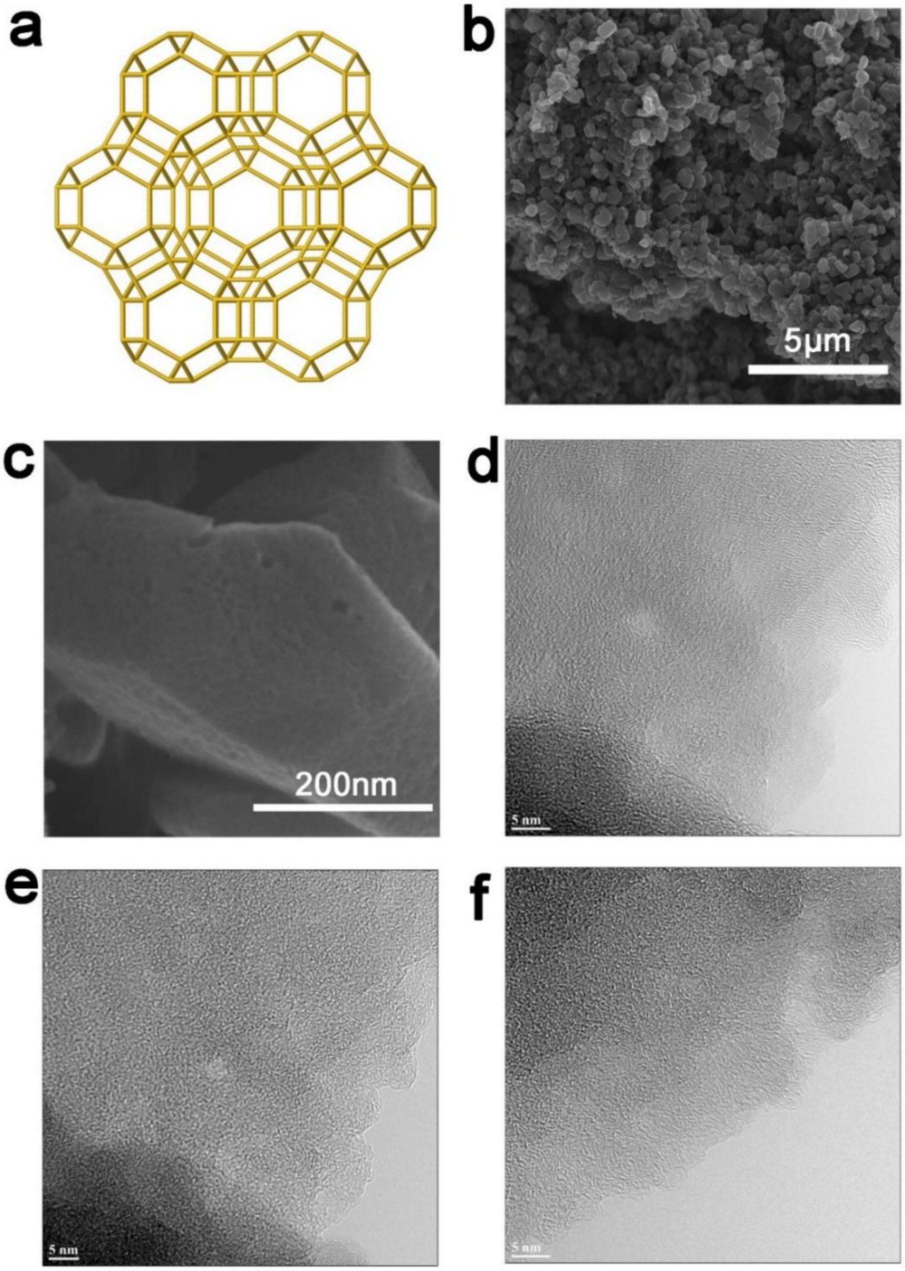

Figure 2.1 Zeolite-Y templated N-NPG through CVD method: (a) schematic of zeolite-Y with FAU (faujasite) structure, (b) and (c) SEM images of zeolite-Y templated N-NPG under different magnifications, (d-f) TEM of the N-NPG nanosheets with nanopores.

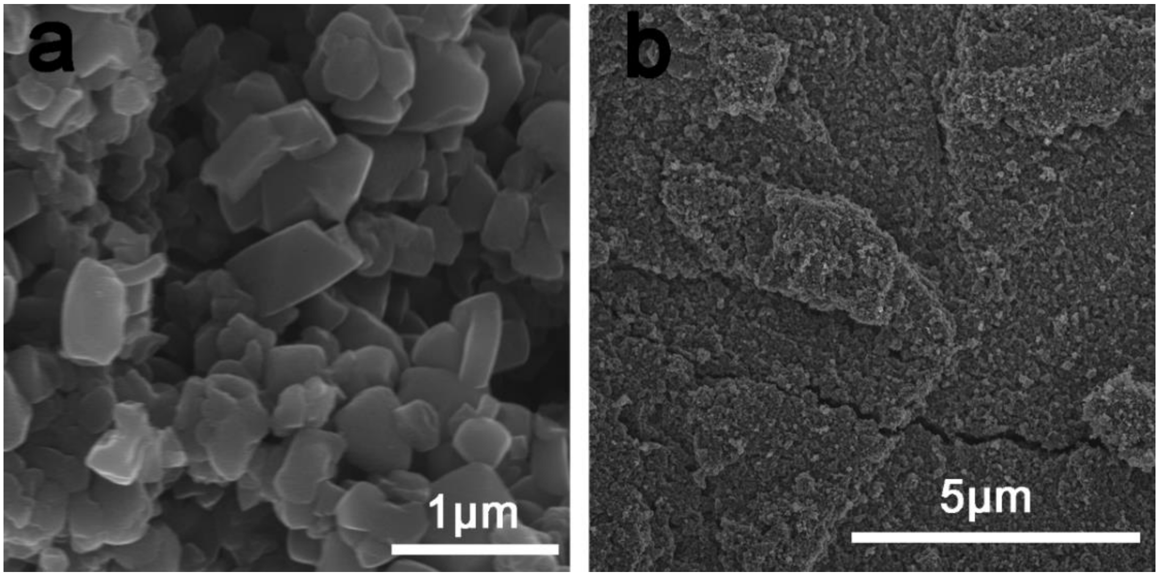

Figure 2.2 (a) and (b) SEM images of N-NPG under different scale.

Scanning electron microscope (SEM) in Figs. 2.1b and c and Fig. 2.2 clearly show nanoporous graphene particle less than 1μm. Enlarge views of the transmission electron microscopy(TEM) images in Figs. 2.1d-f reveal that the resultant N-NPG was constructed with holes ranging from 1 to 5 nm in diameter and the graphitic structures could facilitate electrocatalysis. The observed highly porous structure could provide a significant number of accessible active sites and rich microporosities and mesoporosities for sufficient electrolyte/ion diffusion during the electrocatalytic process.

The powder X-ray diffraction (XRD) patterns and small angle XRD (SAXRD) patterns of zeolite-Y, NPG and N-NPG are shown in Figs. 2.4a and b respectively. XRD patterns show the peak at ca. $2\theta=26°$ indicating the graphite structure in both NPG and N-NPG. Furthermore, the SAXRD shows a peak at ca. $2\theta=6°$ from ordered (111) plane of zeolite-Y, indicating NPG and N-NPG samples have a replica of ordered nanopores of zeolite-Y templates and offer the graphene with highly nanoporous structure.

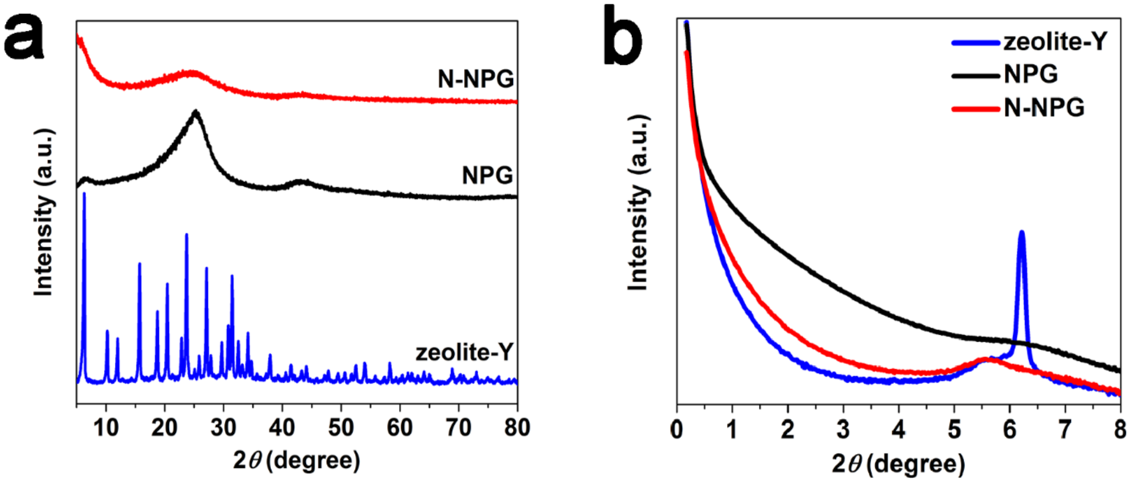

Figure 2.3 (a) XRD of zeolite-Y, zeolite-Y-templated NPG, zeolite-Y-templated N-NPG; (b) the corresponding small angle XRD.

Raman spectra of NPG and N-NPG samples in Fig. 2.4a show the G peak for N-NPG shifted to 1593 $cm^{-1}$ from 1589 $cm^{-1}$ of NPG's G peak and $I_D/I_G$ of N-NPG (~0.39) which is relatively lower than that of NPG (~0.28). As the G peak demonstrates the graphite-like structure and the D peak indicates the presence of defects[130], the sharp G peak proves the high crystalline quality of both NPG and N-NPG while the doping process for N-NPG introduces more defects which are potential electrochemical active sites for electrochemical catalysis and lithium-ion storage.

The presence of N atoms in the N-NPG can be confirmed by X-ray photoelectron spectroscopic (XPS) measurements, as shown in Fig. 2.4b. The XPS survey spectrum (Fig. 2.4b) for the N-doped graphene shows a sharp C1s peaks at 284.6 eV, N1s peak at ca. 400 eV, and O1s peak at 532.4 eV. The absence of Si and Al peaks in XPS survey spectrum indicates that the template has been removed completely by HF and HCl solution. The high-resolution XPS (HRXPS) spectra of C1s and N1s are shown in Figs. 2.4c and d, respectively. The C1s peak can be resolved into $sp^2$ and $sp^3$ carbon at ~284.6 eV, C-N bonding at ~286.0 eV and hydroxyl carbon at ~289.4 eV[90], while HR-XPS spectra of N1s peak reveals pyridinic N at 398.4 eV, pyrrolic N at 399.7 eV and quaternary N at 401.0 eV [131] in the N-NPG samples.

The specific surface area of N-NPG was measured the Brunaue-Emmett-Teller (BET). N-NPG shows a high specific surface area of 786 $m^2\ g^{-1}$, greater than N-doped 3D graphene nanoribbon networks (N-GRW) (~530 $m^2\ g^{-1}$)[132] and the N-doped graphene foam by CVD method (436 $m^2\ g^{-1}$)[133]. Barrett-Joyner-Halenda (BJH) pore size distribution curves derived from the $N_2$ desorption confirms the presence of micropores with diameters less than 2 nm and mesopores between 3 and 20 nm (Fig. 2.5a) and an average pore volume of 0.63 $cm^3\ g^{-1}$. The type IV isotherm curve with a clear hysteresis confirms the presence of micropores and mesopores (Fig. 2.5b). Therefore, the N-NPG sample with stereoscopic holes possesses a large surface area, high pore volume, and wide pore size distribution suitable to facilitate the electrocatalysis.

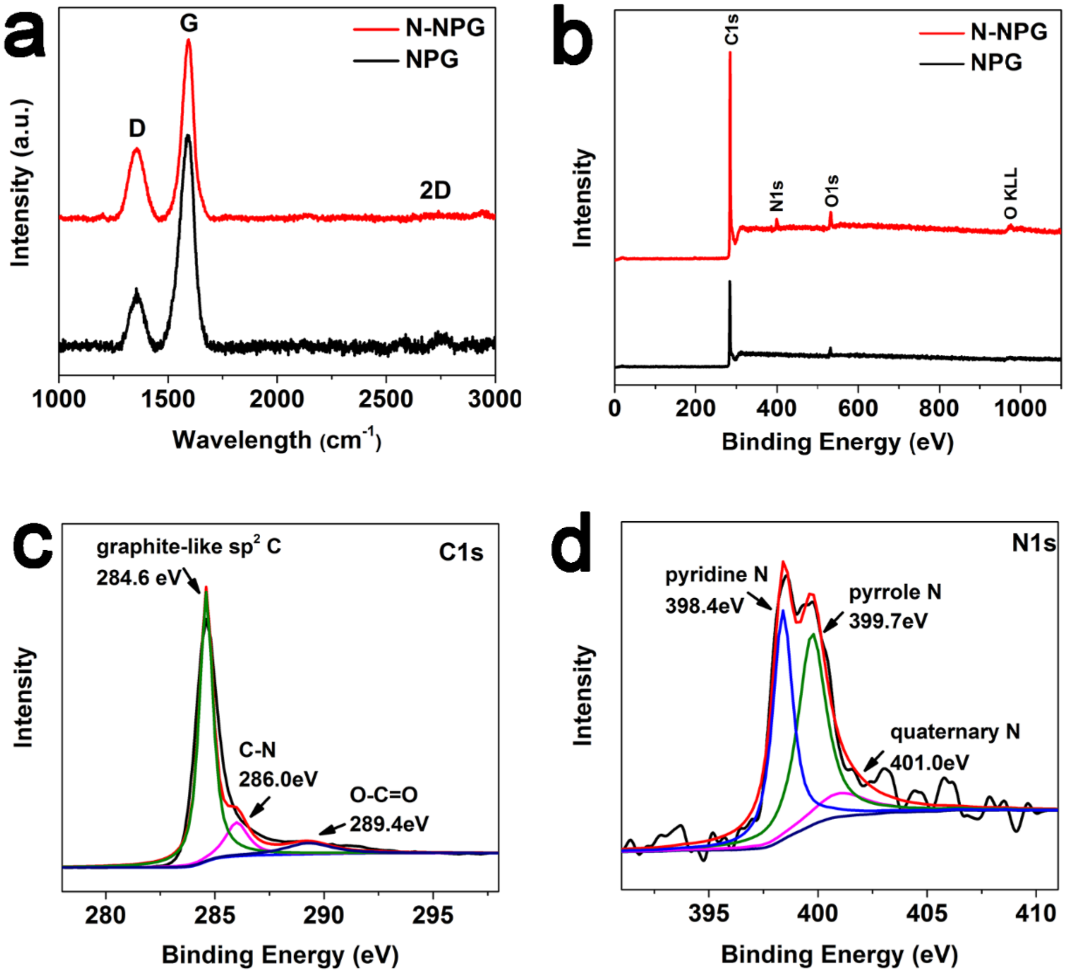

Figure 2.4 (a) Raman spectra of NPG and N-NPG; (b) XPS survey spectrum of N-NPG-3 from zeolite-Y template, it reveals there are C, N, and O elements in the resulting sample; high-resolution XPS of (c) C1s and (d) N1s in N-NPG-3 samples.

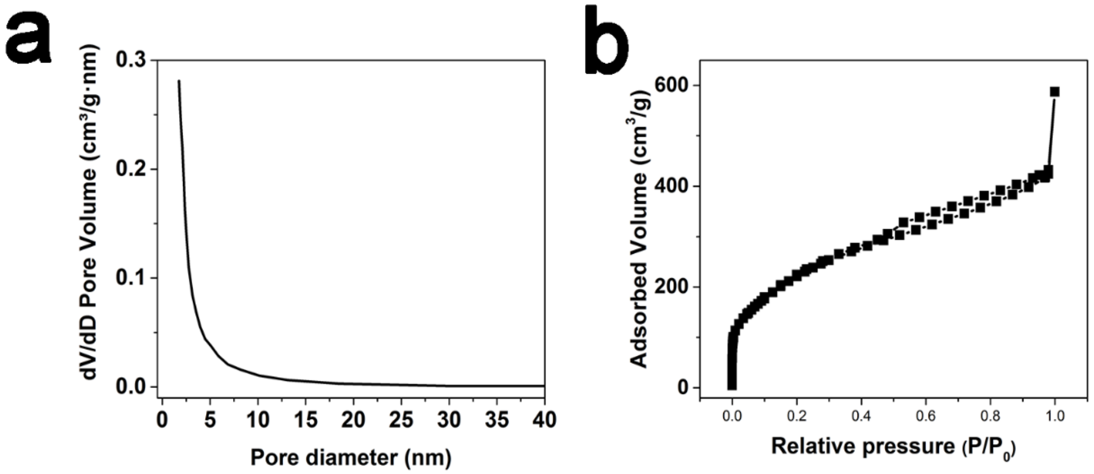

Figure 2.5 (a) Nitrogen adsorption/desorption isotherms and related pore size distribution (b) of N-NPG.

The growth mechanism of N-NPG was investigated under various experimental conditions. The zeolite-Y materials were heated under CVD conditions using acetylene for 30 min at different temperatures. As the CVD temperature increased to 800 ℃, acetylene would accelerate to decompose into carbon atoms, which preferred carbonization on the surface of zeolite particles before diffusion in the inner holes. Therefore, the resultant materials are hard to replicate the zeolite-Y pore structure under the high CVD temperature. As seen in Fig. 2.6a, the peak intensities at ca. $2\theta=6°$ in the XRD patterns become weaker corresponding to the higher CVD temperature, suggesting a lower crystallization degree. Correspondingly, the Raman spectra of samples derived from 800 ℃ demonstrated a higher D band and a lower G band than that of samples from 700 ℃. On the other hand, a lower CVD temperature leads to insufficient graphitization, which shows a lower G peak in the Raman spectrum for samples derived from 600 ℃ (seen in Fig. 2.6b).

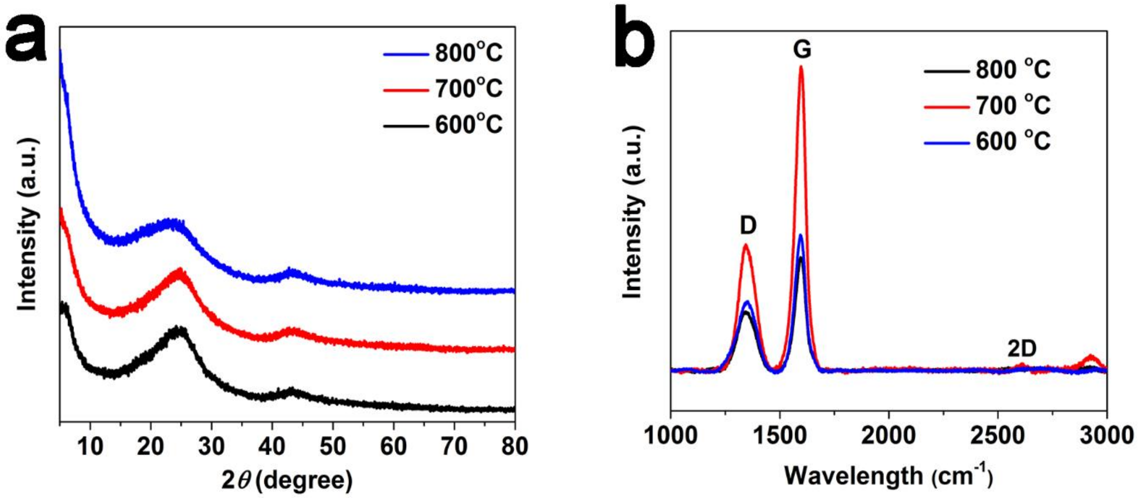

Figure 2.6 (a) XRD and (b) Raman spectra of three zeolite-Y templated NPG for investigation of the growth temperature effect.

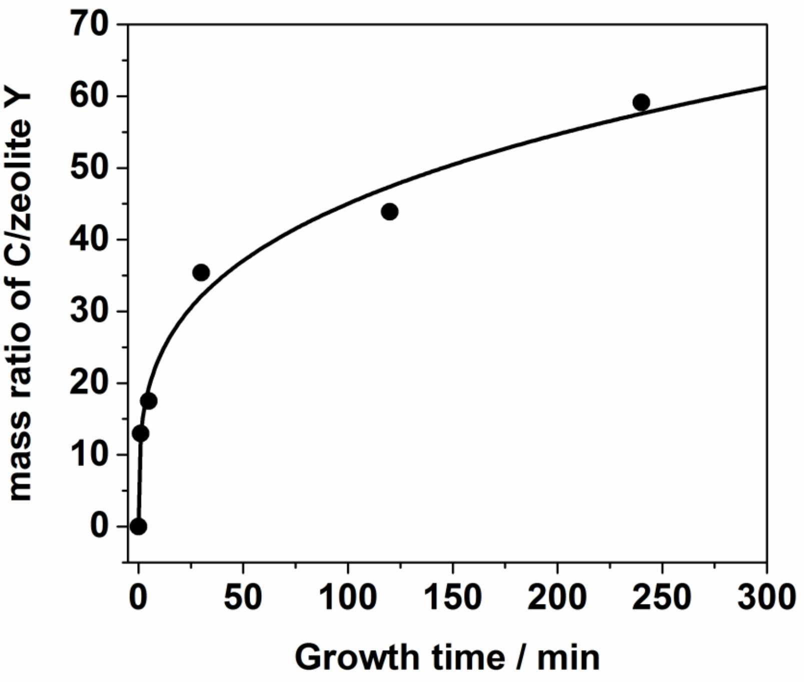

Figure 2.7 TGA of zeolite-Y-templated NPG showing the carbon depositing ratio to the zeolite-Y with the increasing growth time.

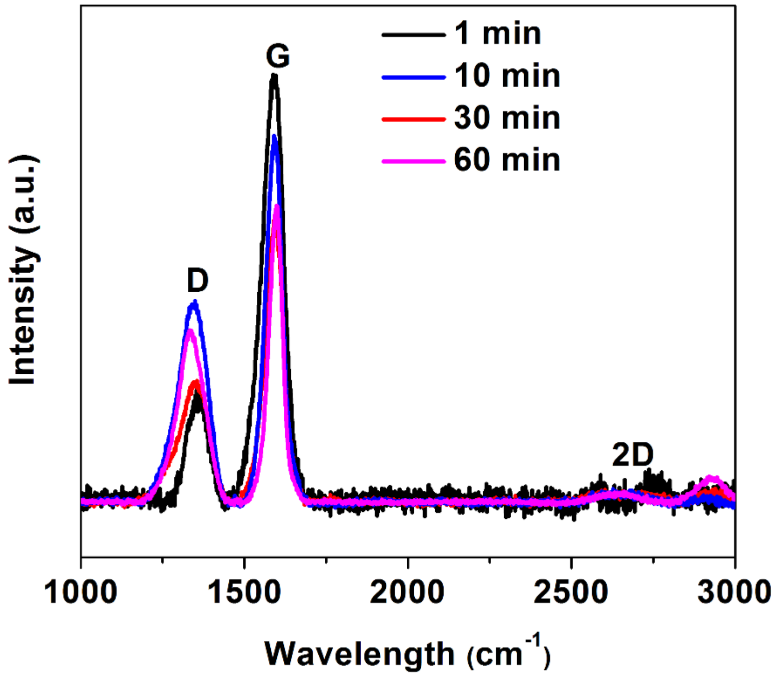

Figure 2.8 Raman spectra of three zeolite-Y-templated NPG for investigation of the growth time effect.

To investigate the carbon deposition process, the NPG materials were prepared at 700 ℃ with different growth duration, varying from 1 min, 5 min, 10 min, 30 min, 1 hour to 3 hours. The amount of carbon deposition at each growth time was measured by thermogravimetric and analyzed as a function of growth time, as seen in Fig. 2.7. The data indicates the rapid carbon depositions within 20 min and the zeolite-Y can accommodate a large number of carbon atoms to anchor after 3 hours' CVD growth. The Raman spectra in Fig. 2.8 demonstrate the increased D band, illustrating the more induced defects with the increasing growth time. However, the lasting treatment in 700 ℃ can lead to a better graphitic crystallization. As a result, the G band also increases. After comparison and optimization, we found that the samples under CVD with the temperature of ca. 700 ℃ for 10 min could achieve an excellent electrochemical performance.

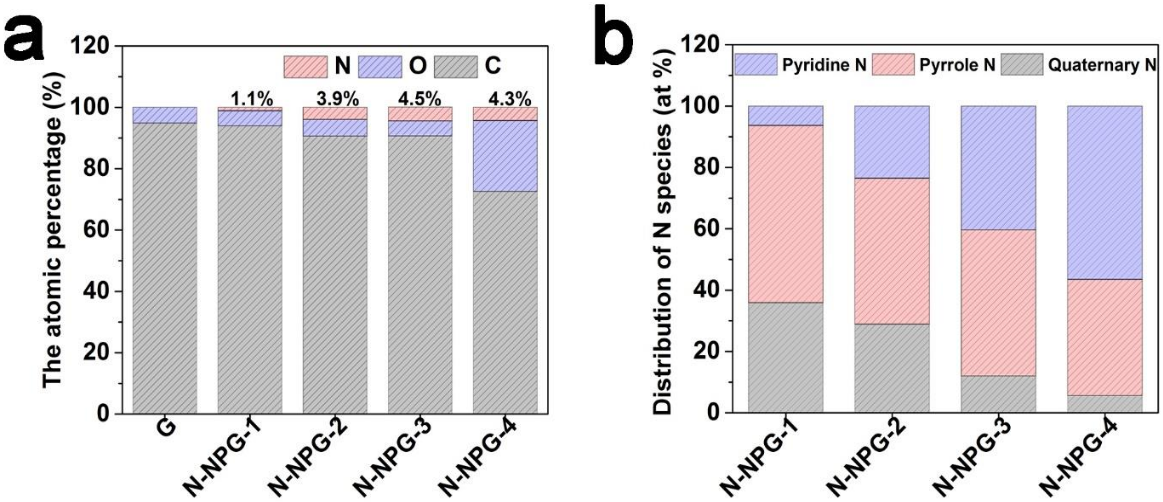

Figure 2.9 (a) The atomic percentage (%) of C, N, O in graphene and N-NPG through XPS; (b) distribution of N species (%).

For the further investigation of N doping effect on electrochemical performance, N-NPG samples with different N contents were prepared by changing the extra ammonia injection time from 0, 10, 30, to 60 min. The sample N-NPG-1 was obtained by CVD growth under mixture gas of $C_2H_2$, $NH_3$ and Ar at 700 ℃ for 30 minutes. Accordingly, N-NPG with further ammonia treatment for 10, 30, and 60 min were denoted as N-NPG-2, N-NPG-3, and N-NPG-4. Since no additional ammonia treatment, the content of N in the N-NPG-1 sample is as low as 1.1%. As the additional ammonia treatment extended, the N contents increased until reaching ca. 4.3%~4.5% while the C % reduced because of the etching of carbon atoms under the ammonium atmosphere at the high temperature.  The study of N species in Fig. 2.9b and Fig. 2.10 illustrate the decrease of quaternary N in the honeycomb lattice and the increase of the pyridine N, indicating the transformation of quaternary N to pyridine N in graphene with the ammonia treatment time.

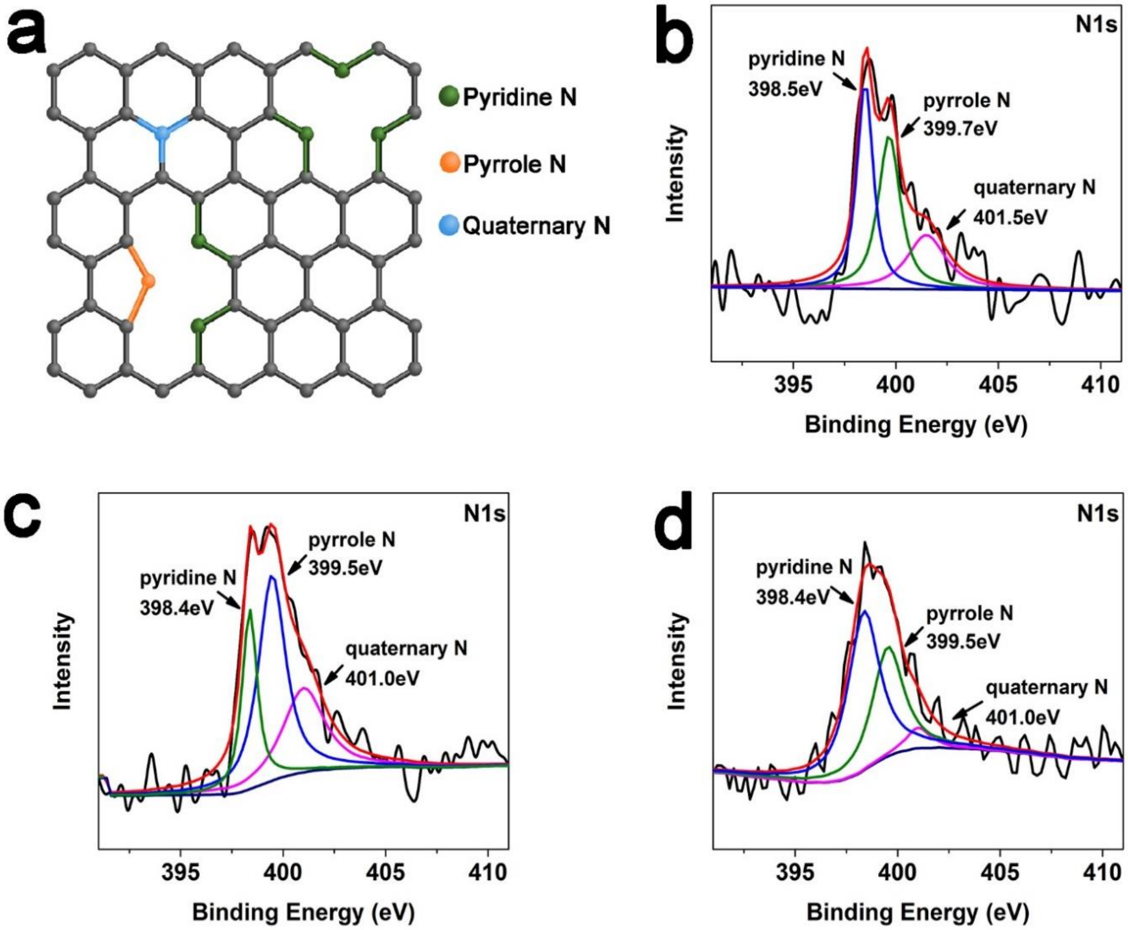

Figure 2.10 (a) Schematic nitrogen types in N-doped graphene; high-resolution (HR-XPS) spectrum of N 1s from (b) N-NPG-1, (c) N-NPG-2, and (d) N-NPG-4.

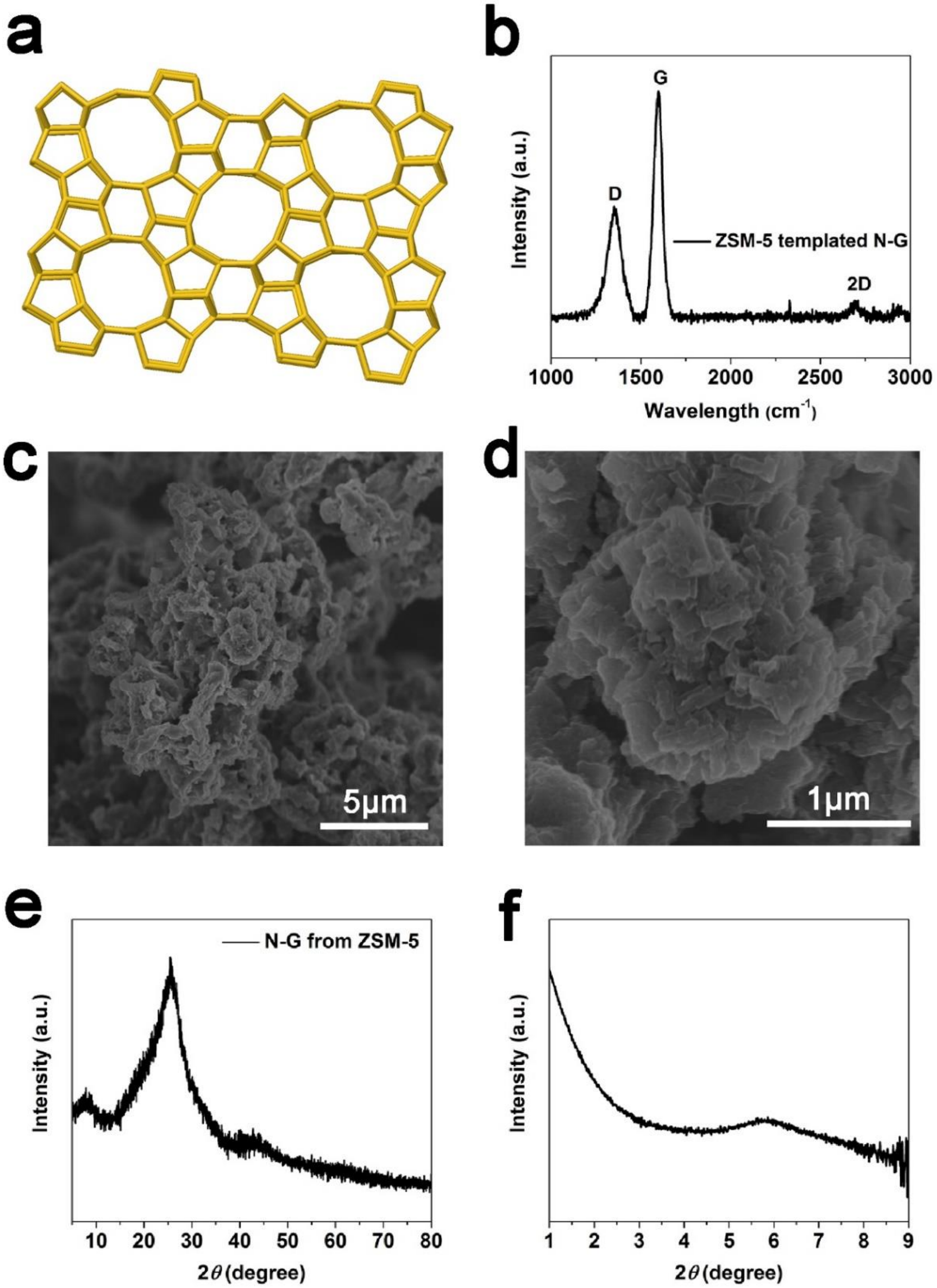

Figure 2.11 N-doped nanoporous graphene from zeolite-ZSM-5: (a) structure of zeolite-ZSM-5; (d) Raman spectrum, (b) and (c) SEM images, (e) XRD and (f) SAXRD of N-doped nanoporous graphene derived from zeolite-ZSM-5.

Not only the N-NPG samples can be synthesized on zeolite-Y, but the N-doped nanochannel graphene can also be obtained when zeolite-ZSM-5 is applied as templates. In Figs. 2.11c and d, the zeolite-ZSM-5-templated graphene shows the particle morphology via SEM. The Raman spectrum in Fig. 2.11b shows a sharp G and 2D band indication the graphene layer stacking. The XRD and SAXRD in Figs. 2.11e and f both prove the replica of zeolite-ZSM-5 after growing and the template removal. Hence, this straightforward and one-step method can produce multiple N-doped nanoporous graphene materials with tunable N content.

### Electrochemical evaluation of N-NPG for ORR

The electrocatalytic performance for oxygen reduction reaction (ORR) of the N-NPG from zeolite-Y was carried out in $O_2$ or $N_2$-saturated 0.1 M KOH electrolyte. Compared to the electrocatalytic activities in $N_2$-saturated 0.1 M aqueous KOH solution, a characteristic oxygen reduction peak at ca. -0.2 V in the cyclic voltammetry (CV) curve was observed for N-NPG catalyst in $O_2$-saturated 0.1 M aqueous KOH solution, indicating a high ORR activity (Fig. 2.12a).

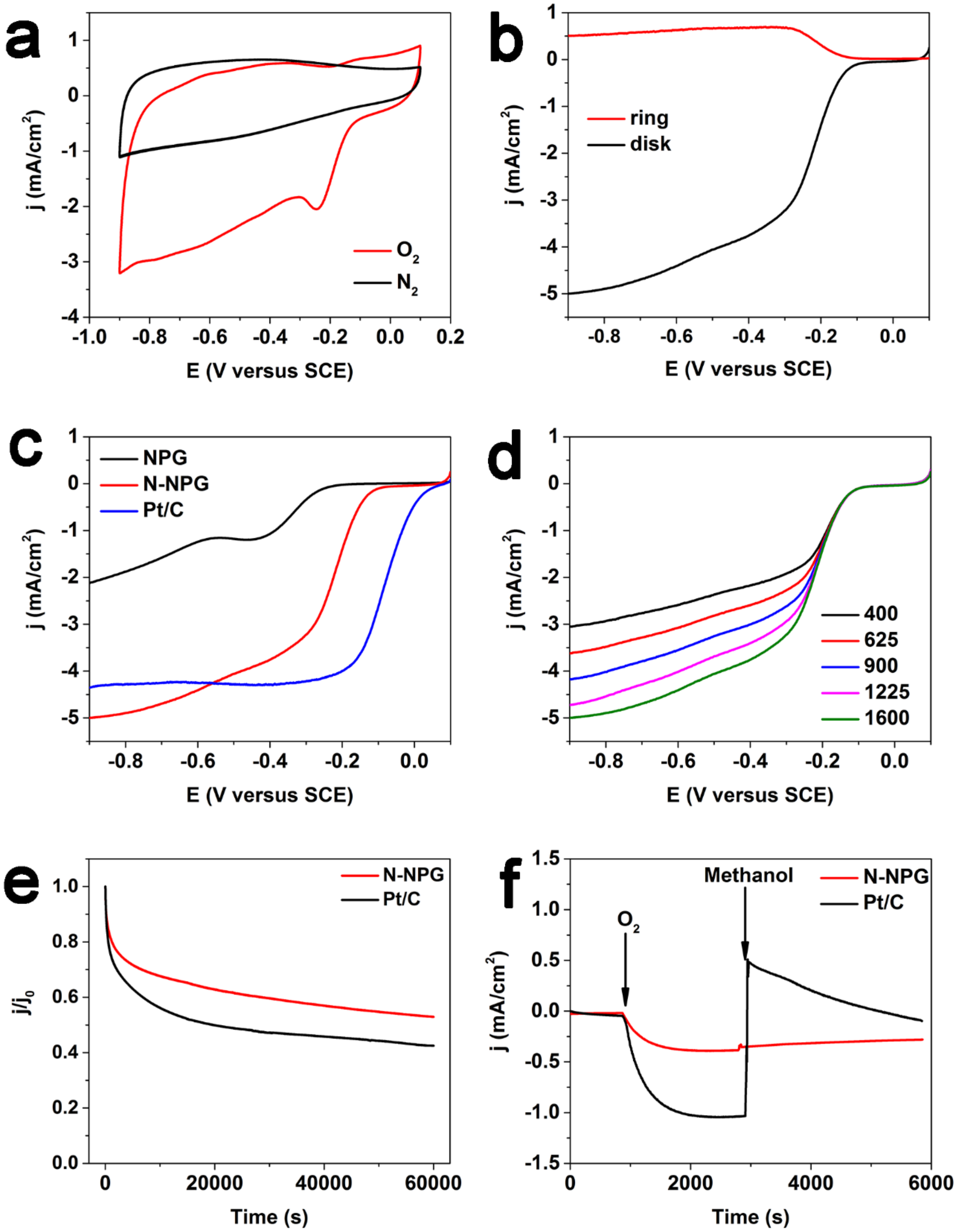

Figure 2.12 (a) CV curve of N-NPG catalyst for the ORR in an $O_2$ and $N_2$-saturated KOH solution (0.1 M); (b) RRDE voltammograms for the N-NPG catalyst at 1600 rpm and the

ring electrode was polarized at 1.1 V, the scan rate: 10 mV $s^{-1}$; (c) LSV for NPG, N-NPG, and Pt/C catalysts on RDE at 1600 rpm; (d) LSVs on RDE at different rotating speed; (e) current-time chronoamperometric response of N-NPG and Pt/C catalysts in an $O_2$-saturated KOH solution at a potential of -0.2 V, the rotating speed: 400 rpm; (f) current-time chronoamperometric response of N-NPG and Pt/C catalysts, the two arrows indicate the introduction of $O_2$ and 10 vol% methanol, respectively.

The linear sweep voltammogram (LSV) measurements were conducted via rotating ring-disk electrode (RRDE) in alkaline electrolytes. Fig. 2.12b shows the disk and ring current for N-NPG catalyst on an RRDE at 1600 rpm, which exhibit an onset potential of ca. -0.15 V, a half-wave potential ($E_{1/2}$) of ca. -0.2 V, and a diffusion-limited current density of ca. -5 mA $cm^{-2}$ versus standard calomel electrode (SCE). These values are close to those of Pt/C (-0.05 V, -0.1 V, -4.4 mA $cm^{-2}$), indicating comparable activities for catalysts. Compared with NPG catalyst, the N-NPG catalyst exhibits a positive shift in the onset potential, showing a superior ORR performance in Fig. 2.12c. As expected, an increased current with the increasing rotation speed can be observed in Fig. 2.12d. Furthermore, N-NPG catalyst shows a higher ORR stability (Fig. 2.12e) than that of commercial Pt/C catalyst after 1000 min chronoamperometric test under the same condition (-0.2 V with $O_2$-saturated KOH solution) and a better methanol tolerance ability (Fig. 2.12f) than that of commercial Pt/C catalyst. These results indicate an efficient metal-free ORR catalyst that attributed to the incorporation of nitrogen in the N-NPG.

To investigate the effect of N doping on ORR activity, N-NPG-1, N-NPG-2, N-NPG-3 and N-NPG-4 catalysts were compared in which the contents of quaternary N and pyridine

N were varied in the nanoporous structure in Fig. 2.9b. The CV curves in Fig. 2.13a demonstrate the enhanced ORR performance with the positive shift of onset potential due to the rising pyridine N species[134]. However, the dramatic decrease of the quaternary N would lead to a drop of nucleophile strength for the adjacent carbon rings and hinder $O_2$ adsorption. Consequently, the N-NPG-4 catalyst exhibits the worse ORR performance in N-NPG materials. LSV curves in Fig. 2.13b also illustrate the similar phenomena. Therefore, N-NPG-3 with the high content of pyridine N and a relatively low quaternary N has the best electrocatalytic performance in ORR.

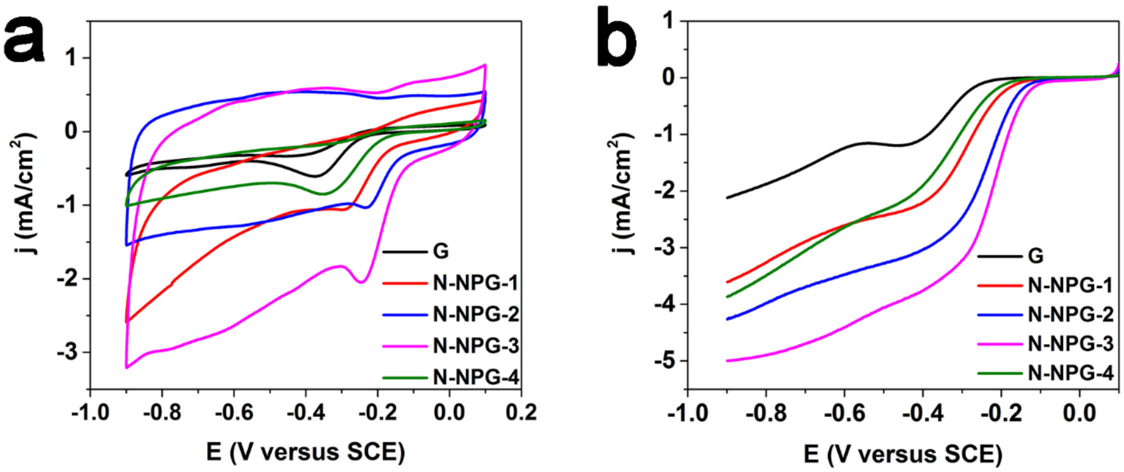

Figure 2.13 (a) CV curves for the ORR in $O_2$-saturated 0.1 M KOH at NPG electrode (black) and N-NPG electrode (with different N content); (b) LSV curves for NPG electrode (black) and N-NPG electrode at an RRDE (1600 rpm), scan rate: 0.01 V $s^{-1}$.

### N-NPG as anode in lithium-ion batteries

The electrochemical performance of N-NPG as anode active materials in LIBs were evaluated by fabricating the battery cells. Fig. 2.14a shows the first three cycle of galvanostatic charge and discharge of N-NPG at a current density of 0.1 A $g^{-1}$ in the voltage range from 0.02 to 3.0 V. In the first discharge process, the plateau at ca. 0.7 V is ascribed to the formation of the solid electrolyte interphase (SEI) film from the electrolyte decomposition[135], which disappears in the second and the third discharge curves. The subsequent cycles demonstrate the reversible and stable discharging and charging behavior without distinct potential plateaus.

The initial discharge and charge capacities are 2083 and 1130 mAh $g^{-1}$, respectively, with an initial Coulombic efficiency of 54%. The charge/discharge capacity of the N-NPG is much higher than that of disordered graphene sheets (1544/1013 mAh $g^{-1}$)[136] due to the large surface area and efficient active sites after N doping. The second discharge and charge capacities are 1174 and 1070 mAh $g^{-1}$, respectively, with a loss capacity due to the SEI formation. Nevertheless, the Coulombic efficiencies reach to and remain above 92% from the second cycles, illustrating the excellent stability and cycling performance, which are attributed to the robust nanoporous structure and the stable chemical structures.

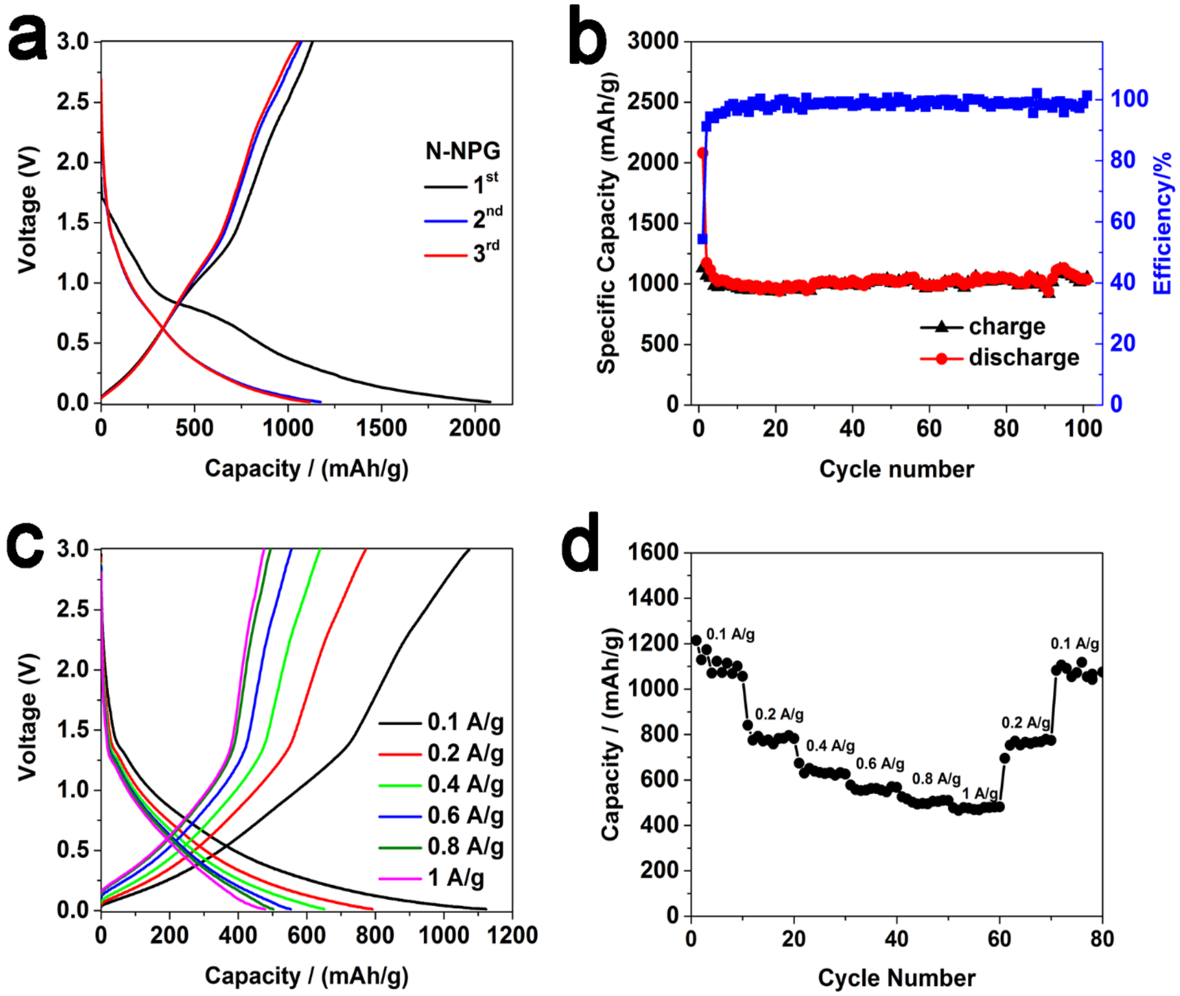

Figure 2.14 (a) Galvanostatic discharge and charge curves of N-NPG anode based LIB at a current density of 0.1 A $g^{-1}$ measured in a voltage range from 0.02 to 3.0 V; (b) cycling performance at 0.1A $g^{-1}$; (c) discharge and charge profiles at various current rates; (d) the corresponding rate performance.

The cycling performance of N-NPG was further investigated by charging/discharging the cells for 100 cycles at 0.1 A $g^{-1}$ in the voltage range of 0.02~3.0 V. As seen in Fig. 2.14b, the N-NPG based anode exhibits a stable charging/discharging behavior after the initial cycles and have the reversible capacity of 1036 mAh $g^{-1}$ after 100 cycles, representing the complete contact and diffusion of electrolytes to the N-NPG anode materials during the cycling. The Coulombic efficiencies are close to 99% after 100 cycles, suggesting the clear nanoporous channels in N-NPG samples for $Li^+$ intercalation and deintercalation. Therefore, N-NPG based anode has the outstanding long-term life due to the robust nanoporous structure.

To test the rate capability, a cell based on the N-NPG anode was measured from 0.1 to 1 A $g^{-1}$ in the voltage range of 0.01~3 V. As seen in Fig. 2.14c, the N-NPG based anode shows a shorten charging/discharging curve as the current density increases. The rate capacity is demonstrated in Fig. 2.14d with the average reversible capacities of 1173, 791, 639, 562, 506, and 479 mAh $g^{-1}$ as the current density increased from 0.1, 0.2, 0.4, 0.6, 0.8 and 1A $g^{-1}$, respectively. After charging/discharging at 1A $g^{-1}$, the reversible capacity of the N-NPG based anode bounces back to 768 mAh $g^{-1}$ at 0.2 A $g^{-1}$ and maintains as high as 1090 mAh $g^{-1}$ when the current density returns to 0.1 A $g^{-1}$, indicating a very good rate capability.

## 2.4 Conclusions

We have developed a scalable and low-temperature approach to fabricate three-dimensional N-doped nanoporous graphene by zeolite-Y-templated CVD method. The homogeneous nanopores with N-doping provide the resulting N-NPG materials with a high specific surface area and rich active sites, which facilitate the fast electron transport and the sufficient electrolyte diffusion in the electrochemical reactions. The resultant N-NPG materials exhibit an effective electrocatalytic activity for ORR with excellent activity with an onset potential of ca. -0.15 V and a half-wave potential ($E_{1/2}$) of ca. -0.2 V, which is comparable to the commercial Pt/C catalyst. The N-NPG catalyst has even a better stability and methanol tolerance than those of the commercial Pt/C catalyst. Furthermore, the N-NPG has been used, for the first time, as the anode in lithium-ion batteries, demonstrating a high initial charge/discharge capacity (2083 mAh $g^{-1}$/1130 mAh $g^{-1}$), an excellent rate capability, and a long cycle life with a reversible capacity of 1036 mAh $g^{-1}$ after 100cycles.

# Chapter 3

# Graphene networks for high-performance flexible and transparent supercapacitors

## 3.1 Introduction

As the depletion of fossil fuel and related environmental pollution become more and more serious, it has become more urgent than ever to develop clean and sustainable energy conversion (e.g., solar cell) and storage (e.g., supercapacitor) systems. Supercapacitor, also referred as electrochemical capacitor, has recently attracted considerable attention because of its high power density and long cyclic lifetime[13, 81, 137]. The recent development of flexible, wearable and paper-like electronics requires lightweight, flexible, all-solid-state energy storage devices as compact power sources[138-140]. Although much progress has been made in developing all-solid-state supercapacitors[141, 142], there is very limited research effort on the development of transparent and flexible all-solid-state supercapacitors[143, 144], since most electrode materials are either transparent with low flexibility (*e.g.*, ITO) or flexible with low transmittance (*e.g.*, conducting polymers). However, transparent and flexible all-solid-state supercapacitors, if developed, are promising components for future smart energy window or integrated energy devices.

Due to its unique structure, excellent mechanical, electrical and optical properties[3, 145], the two-dimensional (2D) graphene has attracted a large amount of interest as new electrode materials for energy conversion and storage. Various approaches, such as metal-catalysed chemical vapor deposition (CVD)[18, 32] and exfoliating graphite by either chemical oxidation[21] or ball milling[146], or electrochemical exfoliation[147] have been developed for the preparation high-quality 2D graphene sheets. Recently, three-dimensional (3D) graphene networks (GNs) have also been produced by directly CVD growth on a nickel foam[23] or by freezing drying graphene oxide dispersion[133]. Owing to their high surface area and hierarchically porous architectures, 3D GNs have been demonstrated to be a new class of efficient electrode materials for energy conversion (*e.g.*, dye-sensitized solar cells[148]) and storage devices (*e.g.*, supercapacitors and lithium ion batteries[149]). However, it is difficult, if not impossible, to prepare 3D GNs with desirable bulk properties to also possess a high transmittance.

In this study, we developed a simple two-step CVD method for depositing continuous 3D graphene network (GN) with a high optical transmittance and excellent mechanical flexibility on copper substrates. The resulting 3D GN could be transferred onto flexible PDMS substrates whilst retaining the high transparency (transmittance of 86% at 550nm wavelength) and good flexibility, leading to ideal flexible and transparent electrode materials. Furthermore, flexible all-solid-state supercapactors based on the 3D GN electrodes were developed and demonstrated to exhibit a transmittance as high as 84% at 550 nm wavelength, which is much higher than that of corresponding devices based on pinhole-free planar graphene sheets[143].

## 3.2 Experimental section

### 3.2.1 Synthesis of graphene network via two-step CVD

A copper (Cu) film of 300 nm-thickness was first sputter-coated (Denton Vacuum Explorer 14) onto a silicon wafer (with 200 nm silicon oxide coated, Silicon Quest International, Inc.). A two-step CVD method was then used to synthesize the GN, as schematically shown in Fig. 3.1 and Fig. 3.2. In the first step, a Cu-coated silicon wafer was put into a sealed quartz tube furnace, which was heated up to 960 ℃ and maintained for 180 s, followed by a fast cooling to room temperature with the mixture of argon (Ar, 400 sccm, 99.99% purity, Airgas) and hydrogen ($H_2$, 10 sccm, 99.999% purity, Airgas) to form the Cu network. Then, the furnace was re-heated up to 960 ℃ under the gas mixture of 200 sccm Ar/5 sccm $H_2$, and maintained at the high temperature for 30 s to 120 s while injecting 5sccm methane ($CH_4$, 99.999% purity, Airgas) for graphene growth. The system was then cooled down under 200 sccm Ar atmosphere. The layer number of the resulting graphene can be tuned by regulating the exposure time of methane.

### 3.2.2 Transfer process of graphene network

To transfer the GN from the silicon wafer, the as-synthesized sample on a silicon wafer ($GN/Cu/SiO_2/Si$, Fig. 3.1) was immersed in an aqueous solution of hydrofluoric acid at a concentration of 20 wt% (HF, Sigma-Aldrich, 48 wt% in $H_2O$) for 30 min. As the $SiO_2$ layer was etched by HF solution, the GN/Cu film gradually separated from the silicon wafer, floating on the surface of the HF solution as a free-standing film.

To transfer the free-standing GN/Cu film onto PDMS and to remove the underlying Cu[39], we prepared the PDMS film by pouring the “base” and “curing agent” at a ratio of 10:1 (Sylgard 184, Dow Corning) into a plastic dish, followed by mixing and thermally curing at 75 °C for 1 hour. The free-standing GN/Cu film was then physically adhered by the solidified PDMS film from the top surface as graphene possessed strong adhesion to PDMS. Finally, pure GN on the PDMS substrate was obtained without obvious structure damage after etching Cu in the $FeCl_3$ solution for 1 hour, followed by thoroughly washing with deionized (DI) water. The similar procedure was also used to transfer pure GNs onto silicon wafers for electron microscopic characterization.

### 3.2.3 Fabrication of supercapacitors using graphene network electrodes

Prior to the supercapacitor assembling, the PDMS-supported GN film was cut into small pieces (3 cm × 1.5 cm) to be used as both current collectors and electrodes. A gel solution containing polyvinyl alcohol (PVA) (1.0 g) and $H_3PO_4$ (1.0 g) in water (10.0 mL) was used as both electrolyte and separator. The gel electrolyte solution was directly drop-coated onto the GN film, followed by solvent evaporation under atmosphere for 6 hours. Thereafter, two pieces of the PDMS-supported GN films coated with the PVA/$H_3PO_4$ electrolyte were assembled under compression (Fig. 1). For the device testing without damage of GN, a copper wire was connected to a small portion of the GN electrode free from electrolyte using silver paste.

### 3.2.4 Characterization

The GN samples were characterized by Renishaw Raman spectroscopy with 514 nm laser. Scanning electron microscope (SEM, JEOL JSM-6510LV/LGS operated at 20 kV) was employed to characterize the GN morphology. The optical properties of graphene electrodes and supercapacitor were measured on a spectrophotometer (Jasco V-670), and the electrochemical properties of supercapacitors were measured on CH Instruments 760C electrochemical workstation.

## 3.3 Results and discussion

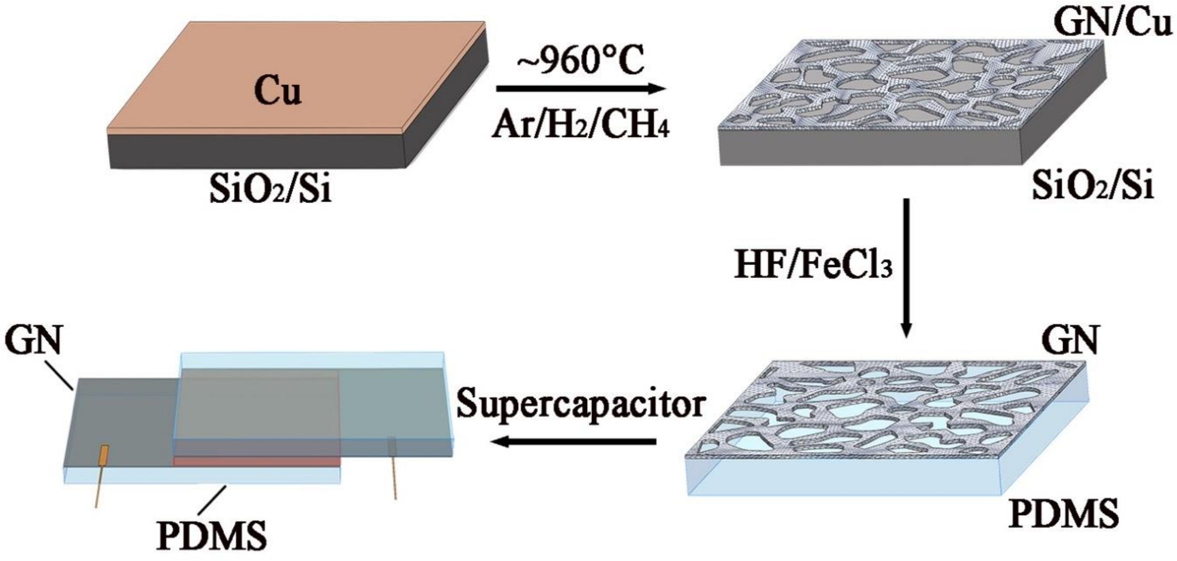

Figure 3.1 Schematic illustration of the procedures for the growth and transfer of the large-scale graphene network (GN), along with the flexible and transparent all-solid-state supercapacitor constructed by sandwiching PVA/$H_3PO_4$ electrolyte between two PDMS-supported GN electrodes, reprinted from ref. [150], copyright © 2014 The Royal Society of Chemistry.

To start with, the Cu network was formed by annealing the 300-nm-thick sputter-coated copper film on a silicon wafer at a controlled temperature during the first step of the two-step CVD (Fig. 3.2). Scanning electron microscope (SEM) images given in Fig. 3.3 show that isolated dot-like and finger-like copper domains formed at 1000 °C and 970 °C, respectively, in accordance with the previous results reported by Ismach *et al.*[151] As seen in Fig. 3.3, Cu network structure was not formed until the temperature was lowered down to 960 °C. It was further found that the macroscopic structure of the Cu network on the silicon wafer could be regulated to a certain extent by adjusting the flow rate of Ar during the first step of the two-step CVD (Figs. 3.2 and 3.4). The estimated area ratio of Cu coverage was found to increase with increasing Ar flow rate (Fig. 3.5). A similar increase in the surface coverage ratio could also be observed for the GN as graphene was deposited on the surface of the copper network.

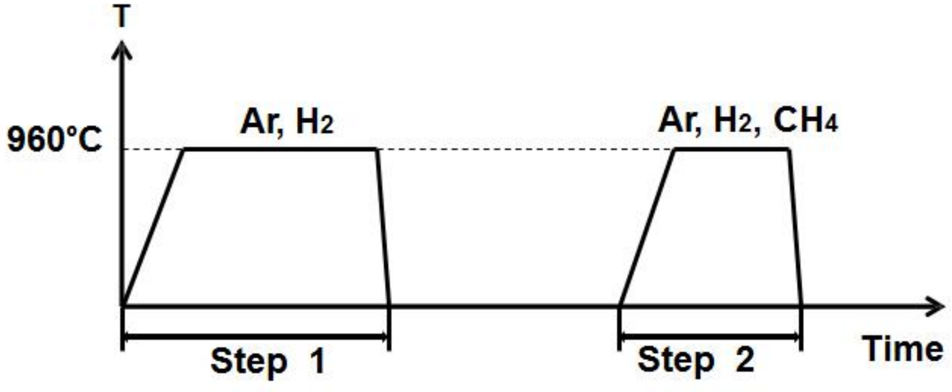

Figure 3.2 Schematic diagrams of two-step chemical vapor deposition for the synthesis of graphene network films. Step 1: heating up to 960 ℃ with a fast cooling process to form copper network; Step 2: at 960 ℃ for graphene growth on the copper network, reprinted from ref. [150], copyright © 2014 The Royal Society of Chemistry.

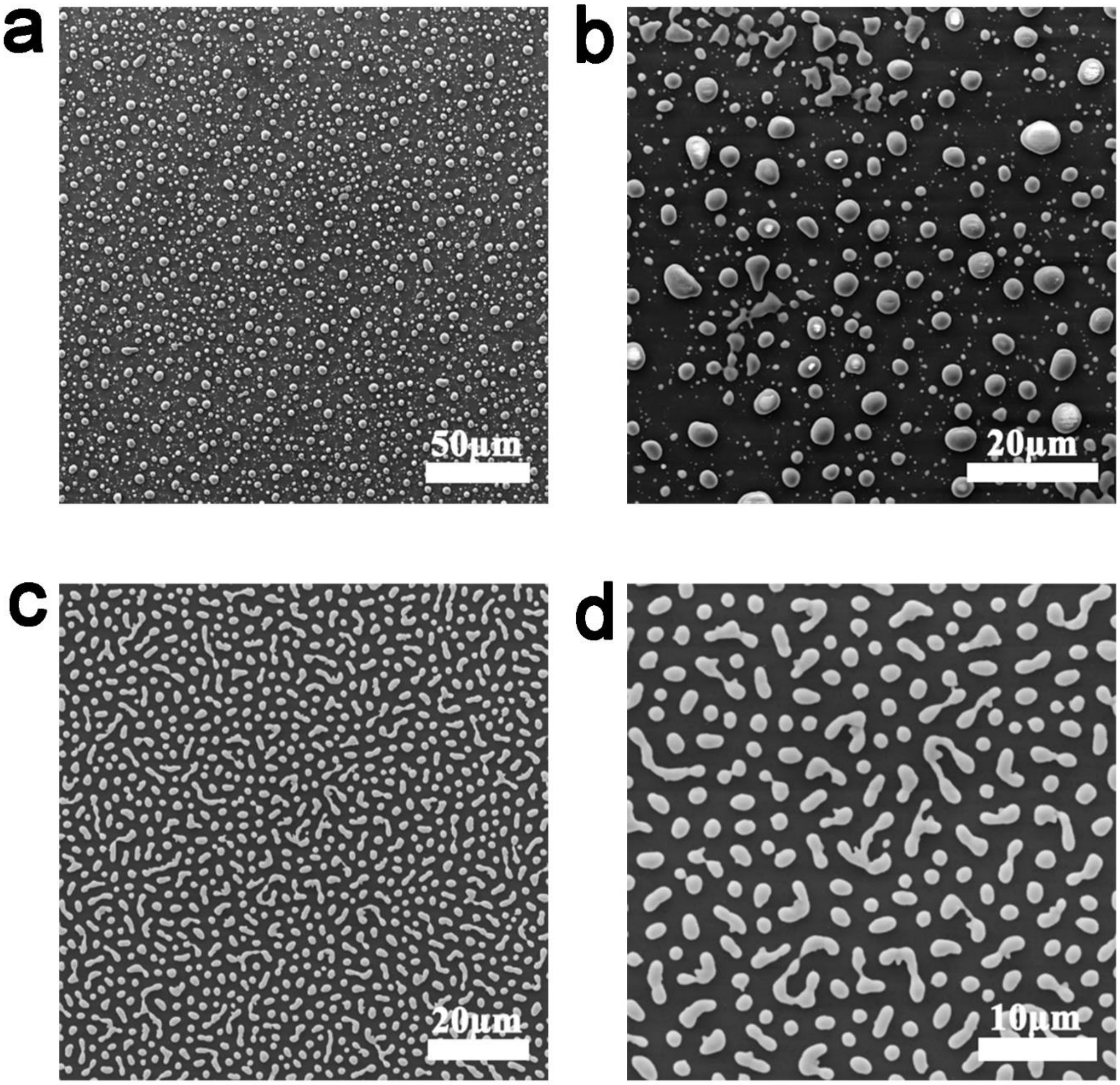

Figure 3.3 SEM images of copper network-like structures by annealing 300 nm-thick sputter-coated copper layer on silicon wafers as a function of the annealing temperature. (a) and (b) the dot-like copper formed at 1000 °C; (c) and (d) the finger-like copper formed at 970 °C, reprinted from ref. [150], copyright © 2014 The Royal Society of Chemistry.

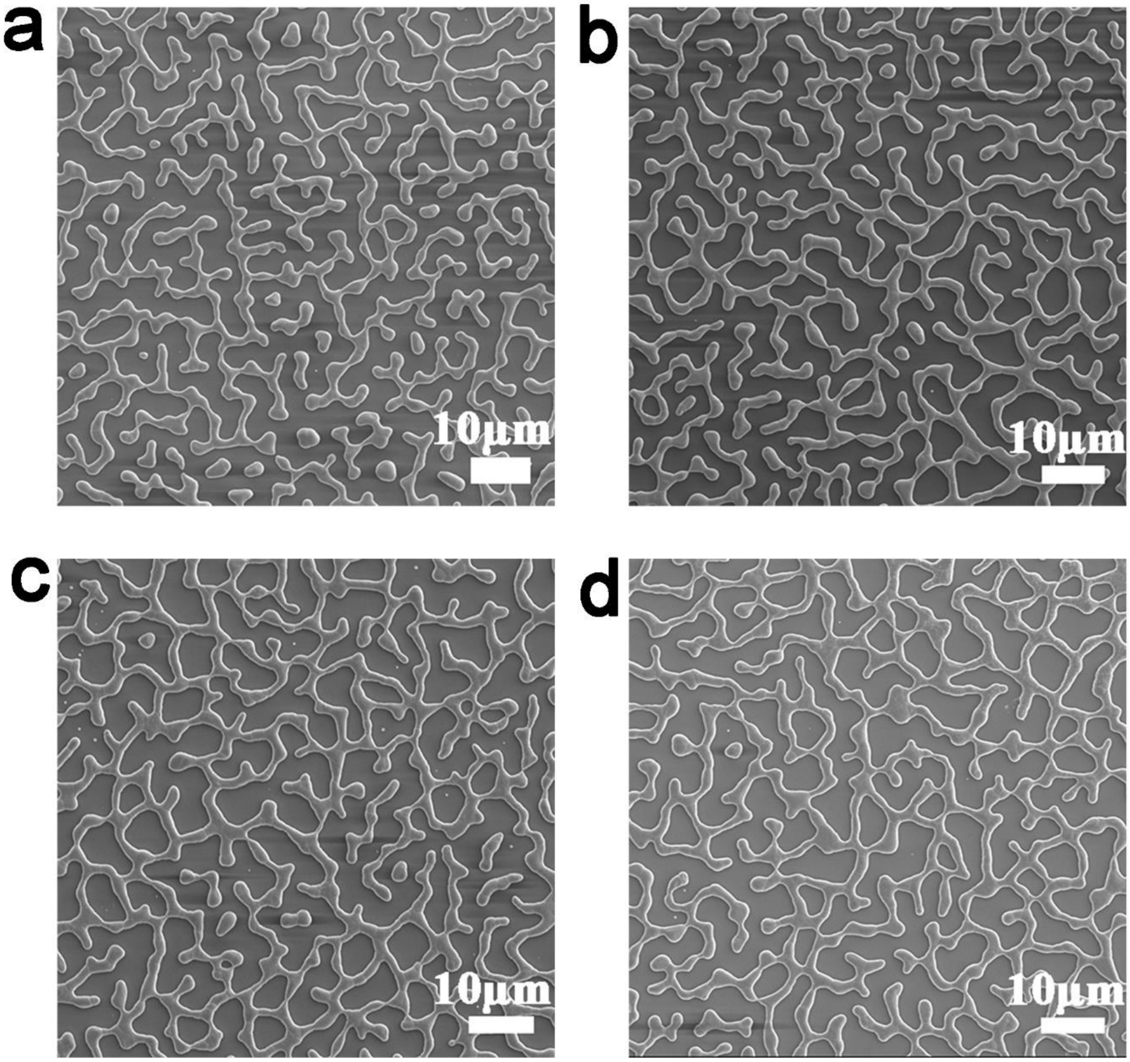

Figure 3.4 SEM images of the copper networks generated from 300 nm-thick copper coatings by heating at 960 ℃ for 180 s under Ar with different flow rates. From a) to d), Ar flow rates are 50, 100, 200, and 400 sccm, respectively, reprinted from ref. [150], copyright © 2014 The Royal Society of Chemistry.

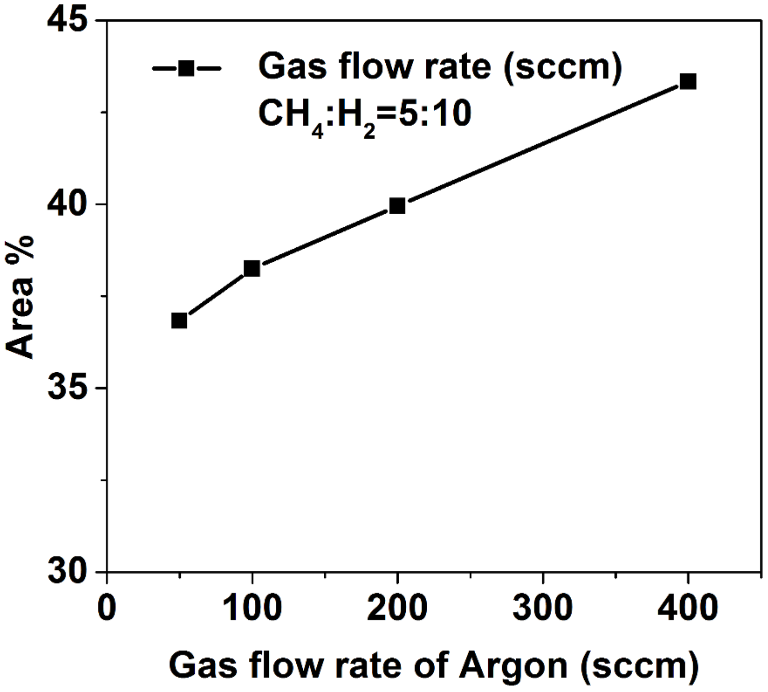

Figure 3.5 The surface coverage ratio of the Cu network formed by annealing at 960 °C for 180 s as a function of the Ar flow rate (50, 100, 200, and 400 sccm), reprinted from ref. [150], copyright © 2014 The Royal Society of Chemistry.

During the second step of the two-step CVD, a thin film of few-layer graphene grew on the Cu network formed at the first step. As shown in Figs. 3.6a-d, the width of graphene ribbons within the GN formed on the copper substrate is about 1-2 μm. The average hole size within the GN ranges from 5 to 10 μm. The results show that the Cu network acted as the catalyst to support the graphene growth. During the carbon source deposition process, most part of the catalyst would be covered by the grown graphene. Meanwhile rest part of the catalyst will expose to the carbon sources by shrinking and evaporation, which result in the new nucleation of graphene and the increasing of the graphene layers. Raman spectroscopic measurements at different locations on the as-synthesized GN (Figs. 3.6e and f) clearly show that graphene was deposited on the Cu network, but not in the Cu-free regions. Raman spectra recorded on the Cu network (*i.e.*, points 1, 2, and 3 in Fig. 3.6e) exhibit the D, G and 2D bands with a much higher G band intensity ($I_G$) than that of the D band ($I_D$) (Fig. 3.6f), indicating the presence of high-quality graphene on the Cu network. In Fig. 3.6f, the intensity ratio $I_D/I_G$ and $I_G/I_{2D}$ are 0.5 and 1.3 respectively, which prove to be several layers graphene.

The layer number of graphene thus formed could be controlled by adjusting the deposition time during the step 2 of the two-step CVD. As can be seen from Raman spectra shown in Fig. 3.7, the G to 2D peak intensity ratio increased from 0.8 to 2.4 with increasing the CVD time, indicating the layer number of graphene increases from 2-4 layers to 8-10 layers as the exposure time to carbon source increases from 30 s to 120 s. However, the intensity ratio of D band ($I_D$) to G band ($I_G$) keeps at 0.3~0.5, showing more defects existing in the graphene network than that of the planar graphene sheet, which can be attributed to the formed edges in the network of graphene compared with the planar graphene sheet. Unlike many other complex patterning methods[152], this newly-developed simple two-step CVD allows for the direct formation of highly conductive GN with a well-connected network structure, which are promising to be used as transparent and/or flexible electrode materials for various applications, as exemplified by flexible and transparent all-solid-state supercapacitors developed in the present study (*vide infra*).

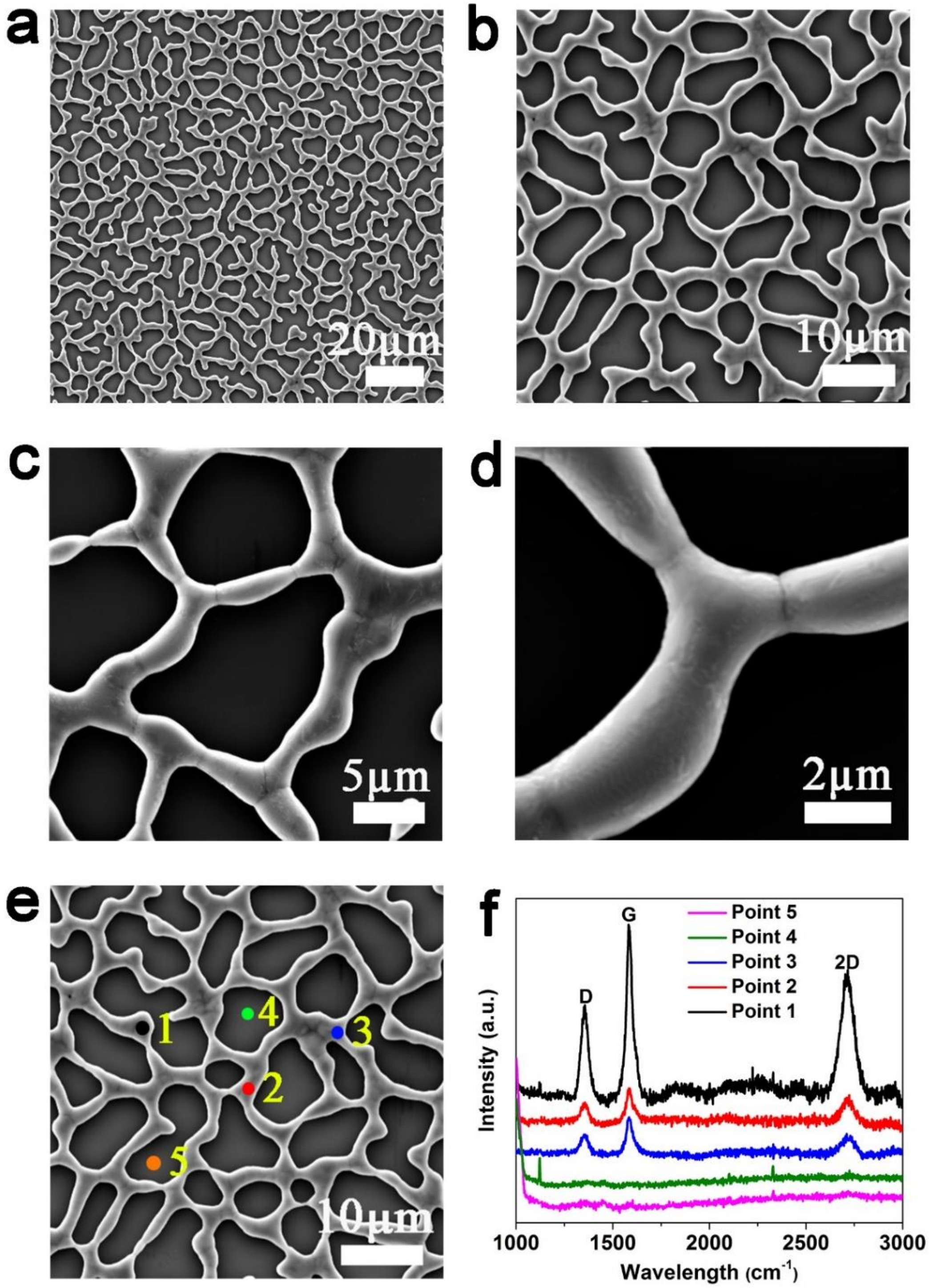

Figure 3.6 SEM images and Raman spectroscopy of GN deposited on the Cu network substrate. (a) and (b) SEM images of the GN on the Cu network substrate at low

magnification; (c) and (d) SEM images of the GN on the Cu substrate at high magnification; (e) SEM image of a sample with 300 nm Cu after 120 s CVD growth, showing the morphology of the graphene on metal network; (f) Raman spectra measured at five different points marked with different colour dots in (e), reprinted from ref. [150], copyright © 2014 The Royal Society of Chemistry.

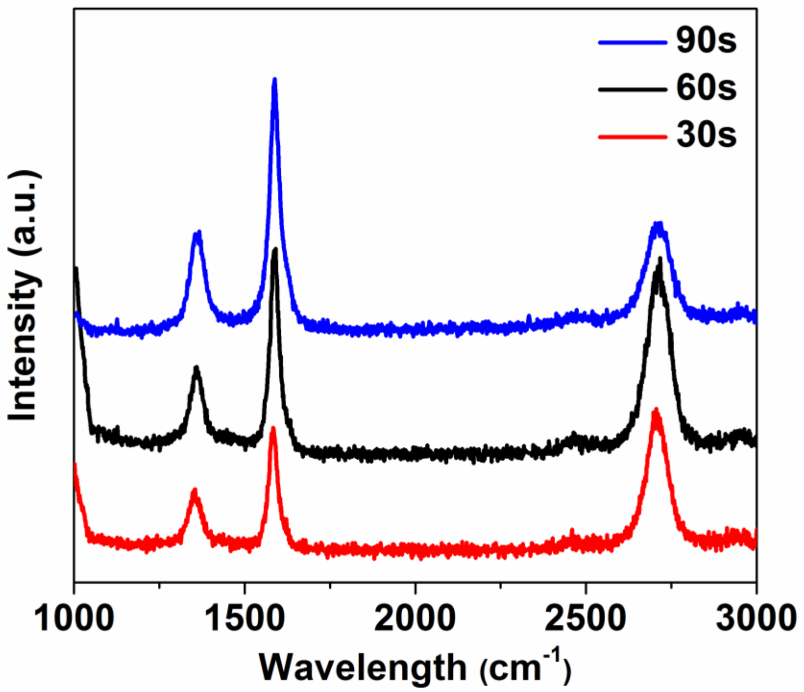

Figure 3.7 Raman spectra of the pure GN films transferred onto silicon wafers prepared by the two-step method as a function of growth time. The GN films were synthesized at 960 °C with 5 sccm $CH_4$ under the gas mixture of 200 sccm Ar/5 sccm $H_2$. The exposure time to carbon source for red, black and blue lines are 30 s, 90 s, 120 s respectively, reprinted from ref. [150], copyright © 2014 The Royal Society of Chemistry.

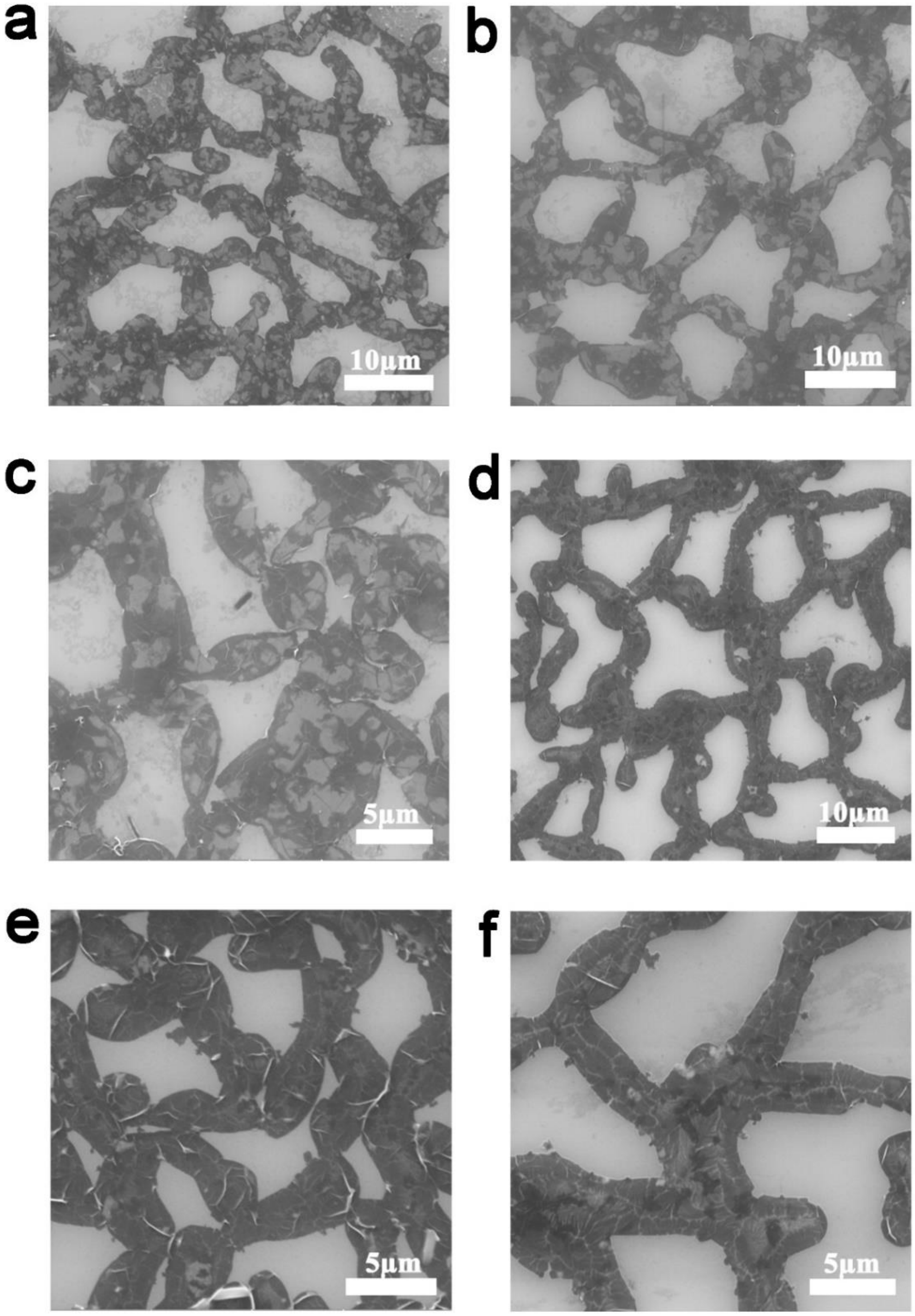

Figure 3.8 SEM images of the pure GN films transferred onto Silicon wafers. (a), (b) and (c) the graphene networks formed at 960 ℃ after 30 s exposure time to the carbon source.

(d), (e), and (f) the graphene networks formed at 960 °C after 120 s exposure time to the carbon source. The gas flowing rate ratio of Ar, $H_2$, and $CH_4$ is 200: 5: 5, reprinted from ref. [150], copyright © 2014 The Royal Society of Chemistry.

Prior to fabrication of the GN-based supercapacitors, pure GNs after removing the underlying Cu layer were further subjected to electron microscopic characterization. SEM images of the GN transferred onto a clean silicon wafer given in Fig. 3.8 show wrinkles across graphene ribbons within the GN, presumably resulted from the surface-tension-induced shrinking/collapsing of the free-standing graphene surface during the transfer/Cu-etching processes. Instead of breaking the network integrity, the shrinkage and wrinkle formation near the cross-section points could actually make both thin (Figs. 3.8a-c) and thick (Figs. 3.8d-f) GNs even stronger

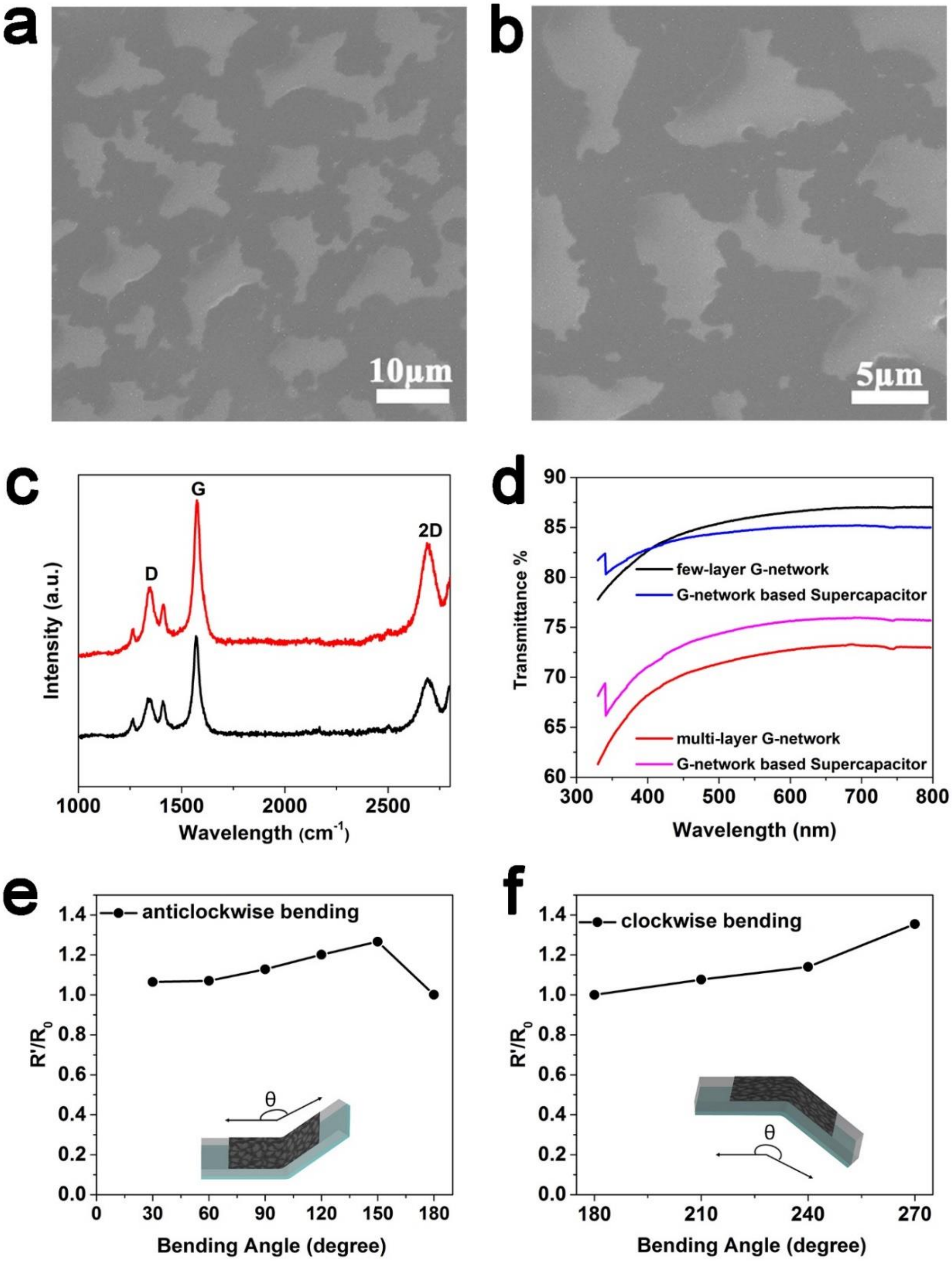

Figure 3.9 (a) and (b) show the SEM images of the GN films transferred on the PDMS substrate; (c) Raman spectra of the PDMS-supported GN films with two different layer

numbers (red: 2-4, black: 8-10); (d) optically transmittance of the 2-4 layers and 8-10 layers layer GN films on the PDMS substrate. (e) and (f) dependence of the two-electrode electrical resistance of GN films on the PDMS substrate at different bending angles in clockwise and anticlockwise directions, respectively, reprinted from ref. [150], copyright © 2014 The Royal Society of Chemistry.

Figs. 3.9a and b show SEM images of the PDMS-supported GN network, from which it can be seen that the network of graphene maintained its interconnected structure, though with some distortion, after being transferred onto the PDMS substrate. Raman spectra for the PDMS-supported GN given in Fig. 3.9c also show that there is no obvious change occurred with respect to that of the as-synthesized GN on the Cu network (Fig. 3.6f) or pure GN transferred on a silicon wafer (Fig. 3.7), apart from some additional background signals from the PDMS substrate. Due to its unique network structure, the GN film transferred on the PDMS substrate is highly transparent. As seen in Fig. 3.9d, the 4-layer GN films on PDMS showed a high transmittance of ~86% at 550 nm wavelength, while the transmittance of the 10-layer GN film was ~75%. Both of them are much higher than that of a pin-hole free multi-layer graphene sheet on the similar PDMS substrate reported previously.[10] In addition to the excellent optical transparency, the GN film also exhibited high flexibility. The changes in electrical resistance were measured while bending the PDMS-supported GN film to different angles. The electric resistance of the GN film is ranging from 4-6 kΩ $cm^{-1}$, which is much higher than that of single-sheet multi-layer graphene sheet because of its porous structure. Figs. 3.9e and f show that the change in electrical resistance of the PDMS-supported GN was lower than 40% when it was bent up at the highest possible deformation angles in both clockwise and anticlockwise directions, suggesting a very good flexibility.

The tension test is carried out on PDMS-supported GN by stretching the film in one direction. As seen in Fig. 3.10, the resistance dramatically increased with the tension strain. After the tension strain is released, the resistance drops back to the original value, suggesting the robust network structure.

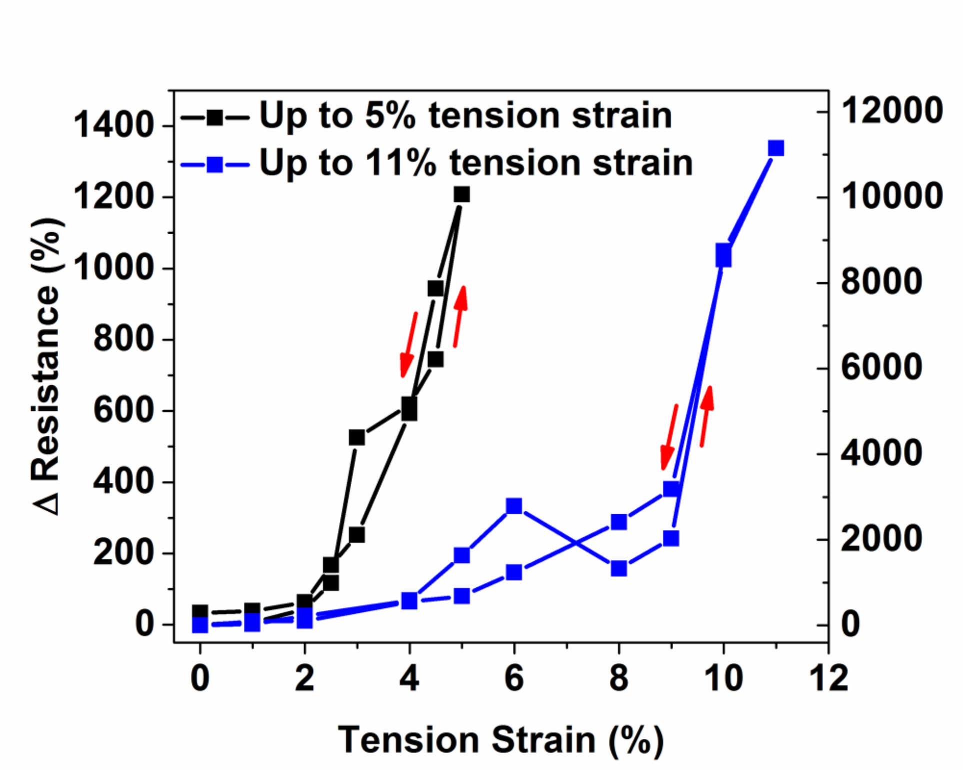

Figure 3.10 Tension test for the resistance *vs*. tension strain, reprinted from ref. [150], copyright © 2014 The Royal Society of Chemistry.

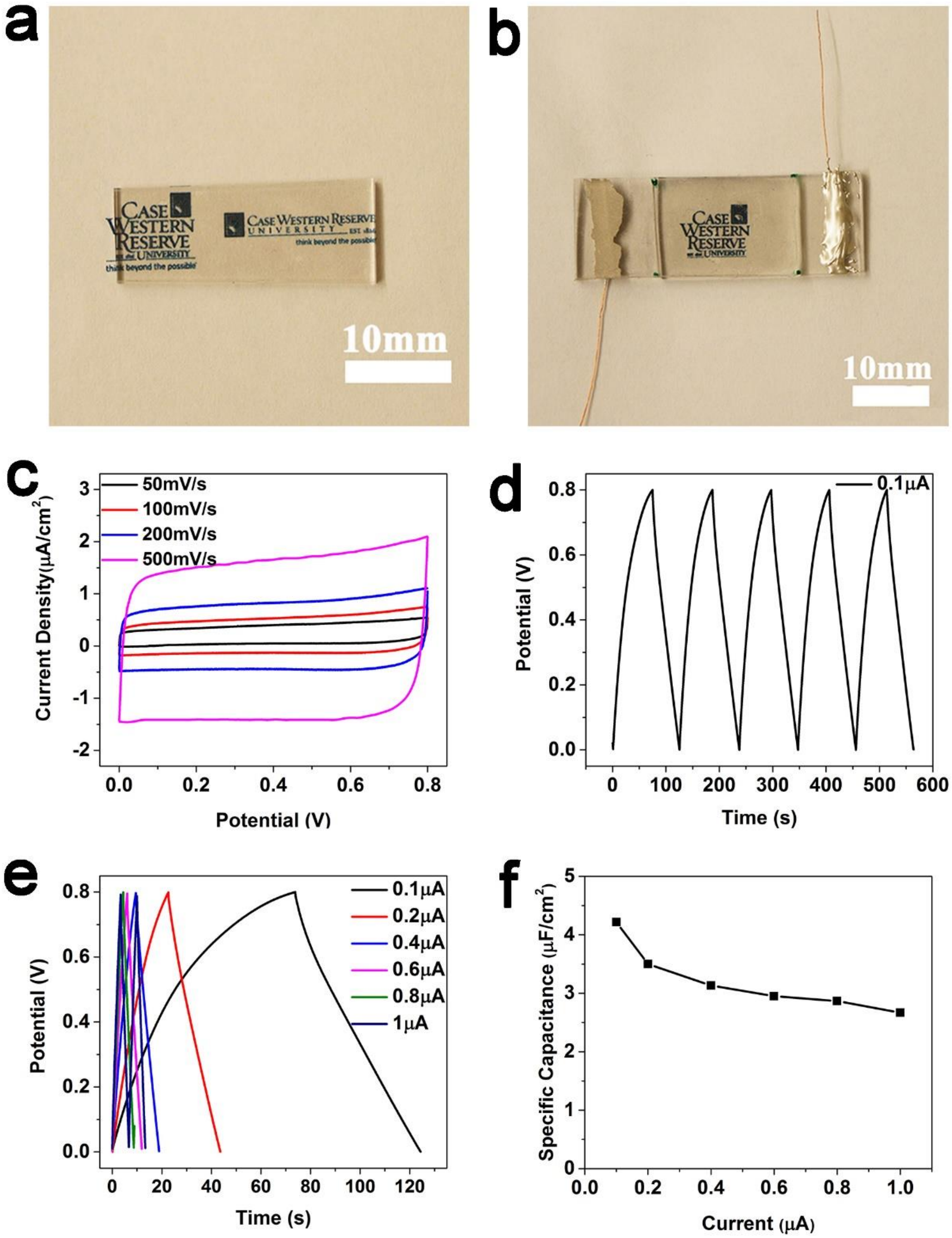

Figure 3.11 (a) and (b) Photograph of the GN films on PDMS and the transparent supercapacitor based on the GN films; (c) CV curves of a typical supercapacitor measured at the scan rate from 50 to 500 mV $s^{-1}$ ; (d) Galvanostatic charge/discharge (GCD) curve

of the device measured at a constant current of 0.1 μA; (e) GCD curves of the device recorded at different applied currents; (f) variation of specific capacitance as a function of the applied current, reprinted from ref. [150], copyright © 2014 The Royal Society of Chemistry.

Using these highly transparent and flexible PDMS-supported GN films as electrodes, we developed flexible and transparent all-solid-state supercapacitors, in which a polymer gel (PVA/ $H_3PO_4$, 1:1 wt%/wt%) was used as both electrolyte and separator. The all-solid-state supercapacitor was assembled by pressing two of the electrolyte-coated GN films supported by the PDMS substrate. Due to the high transparency of the PDMS-supported GN film (Figs. 3.9d and 3.11a) and the polymer electrolyte, the assembled supercapacitor (Fig. 3.11b) shows high transparency with a transmittance of ~84% for electrodes with the 2-4 layers GN and ~72% for that of 8-10 layers (Fig. 3.9d).

Fig. 3.11c shows cyclic voltammetry (CV) curves of such a supercapacitor based on the GN film electrodes measured at the scan rate range from 50 mV $s^{-1}$ to 500 mV $s^{-1}$, which indicates an excellent capacitive behavior with nearly a rectangular shape even at a high scan rate of 500 mV $s^{-1}$. Galvanostatic charge/discharge (GCD) curves given in Fig. 3.11d and e for the flexible and transparent supercapacitor show triangular shapes, suggesting once again nearly ideal capacitive behaviors. The area specific capacitance ($C_{sp}$) was calculated using the equation

$$C_{sp} = {}^{I\Delta t}/_{S\Delta V} \tag{3-1}$$

where $I$ is the applied current, $\Delta t$ is the discharging time, $S$ is the area of the active electrode in supercapacitor, and $\Delta V$ is the voltage window, respectively. From the GCD curves shown in Figs. 3.11d and e, the calculated surface-specific capacitances were 4.2 μF cm$^{-2}$ at the discharge current of 0.1 μA and 2.7 μF cm$^{-2}$ at 1.0 μA (Fig. 3.11f), which were close to those of transparent devices based on uniform multi-layer graphene sheets, but better optical transmittance because of the unique network structure.[10] Comparing with uniform graphene films, the GN films possess an apparently reduced surface area for charge storage. However, the network structure could not only significantly facilitate the electrolyte transport but also impart the edge-effect[153] to enhance the supercapacitor performance effectively. Therefore, the resultant supercapacitor based on the new-developed GN films showed comparable performance with the multi-layer graphene sheet with a planar structure.

## 3.4 Conclusions

In summary, we have developed a simple two-step CVD approach to highly transparent and flexible two-dimensional graphene network films, which can be readily transferred onto various substrates (*e.g.,* rigid silicon wafer and flexible polymer substrates) in large scale for a large variety of applications, including wearable electronics and advanced energy storage. Due to its unique porous and interconnected network structure, such graphene network film transferred on the PDMS substrate showed a transmittance up to 86% at 550 nm wavelength and excellent flexibility. Furthermore, flexible and transparent all-solid-state supercapacitors based on the graphene network electrodes showed a high transmittance of 84% and a large area specific capacitance of up to 4.2 μF cm$^{-2}$. Owing to its unique conductive network structure with high transparency and flexibility, the graphene network films developed in this study should also be very promising for many other applications, including, but not limited to, mechanical sensors, wearable electronics, and integrated energy conversion and storage devices.

# Chapter 4

# N-doped 3D graphene-CNT-graphene for all-solid-state supercapacitors

## 4.1 Introduction

Graphene, an atomic two-dimensional (2D) carbon material with hexagonal lattice, has exhibited attractive in-plane properties such as fast electron transport, large surface area, and superb mechanical properties[3]. The poor out-of-plane properties due to the weak Van der Waals force between layers, however, have limited their applications as electrodes for supercapacitors.

Some efforts have been devoted to exploring the all-direction functions of graphene by establishing three-dimensional (3D) structure, such as embedding metal oxides[64, 67, 83] or introducing conducting polymers between graphene layers[154, 155], which can avoid restacking of graphene layers and enhance the electron transfer in the vertical direction. However, the low compatibility of two different materials would hamper the electrochemical properties. Later, graphene materials with large surface areas have been developed by fabricating 3D graphene (foams[23, 76] or aerogels[22, 156]) with porous structures for efficient ion diffusion and rapid electron transport in all-directions. Nevertheless, 3D graphene materials with a disordered structure cannot be designed in a completely controllable way for supercapacitor integration. Since the theoretical simulation results indicated that the combination of the graphene and the vertically aligned carbon nanotubes (VACNTs) could significantly achieve a superior out-of-plane electron transport while maintaining their excellent intrinsic electric properties[157, 158], synthesis of hybrid material by growth of VACNTs between graphene layers were reported and demonstrated tremendous electrochemical performance as electrodes for supercapacitor[49, 159]. Despite various approaches to realize graphene/CNT heterostructure, some issues have to be addressed, including multiple synthesis steps, hard-to-remove of catalysts, and non-covalent bonding. Therefore, it is desirable to develop a one-step approach to design an ordered 3D graphene with tunable functions.

Here, we present a 3D nitrogen doped graphene-CNT-graphene (N-G-CNT-G) ordered structure via simple one-step chemical vapor deposition (CVD) method. The well-defined N-G-CNT-G structure consists of top and bottom layers of graphene and CNT with 250 nm length between them. The sandwich structure demonstrates a seamlessly covalent bonding between CNT and graphene. The obtained N-G-CNT-G materials have exhibited high specific capacities with a great rate capability, and a long-cycle stability as electrodes in a double-layer all-solid-state supercapacitor.

## 4.2 Experimental section

### 4.2.1 AAO template preparation

250 nm aluminum is sputtering coated (Denton Vacuum Explorer 14) onto a 1 cm × 3 cm silicon wafer (with 200 nm silicon oxide coated, Silicon Quest International, Inc.). The Al thin film was anodized with a constant voltage of 40 V in 0.3 M oxalic acid at 0 ℃ for 1

hour to form anodic porous aluminum oxide (AAO) template. A 1 cm × 3 cm slice of platinum was supplied as a counter electrode, and the distance between the working and counter electrode was 3 cm. After anodization for 1 hour, the pores of AAO template were further expanded by the chemical etching in the 0.1 M phosphoric acid ($H_3PO_4$, 85%, Fisher Scientific) solution for 30 min via water bath at 40 ℃.

### 4.2.2 CVD synthesis of N-G-CNT-G

The highly conductive poly(3,4-ethylenedioxythiophene) polystyrene sulfonate (PEDOT: PSS, 1.1% in $H_2O$, Sigma-Aldrich) solution was spin-coated onto the AAO template with various spinning rate (3000 rpm, 6000 rpm, and 9000 rpm) to change the loading mass. The coated template was baked at 120 ℃ for 15 min before CVD growth and placed at the center of quartz tube in the furnace. 200 sccm argon (Ar, 99.99% purity, Airgas), 5 sccm hydrogen ($H_2$, 99.999% purity, Airgas), and 50 sccm ammonium ($NH_3$, 99.995% purity, Airgas) were introduced into the quartz tube for 30 min, followed by the rapid heating up to 800 ℃ and kept for 120 minutes for the synthesis of G-CNT-G samples. After fast cooling down, the N-G-CNT-G samples were obtained on AAO template.

### 4.2.3 CVD synthesis of G-CNT-G

The G-CNT-G samples were obtained by CVD growth. In brief, PEDOT:PSS coated AAO template were heated up at 800 ℃ for 120 minutes under the atmosphere of 200 sccm Ar and 5 sccm $H_2$. After fast cooling down, the G-CNT-G samples were obtained on AAO template.

### 4.2.4 Characterization

Scanning electron microscope (SEM) images were collected from a Hitachi S-5200 SEM. TEM was performed using an FEI Tecnai F30 TEM working at 300 kV. Raman spectra were collected using a Raman spectrometer (Renishaw) with a 514-nm laser. The X-ray powder diffraction (XRD) patterns were obtained on a Bruker D8-advance X-ray powder diffractometer with Cu Kα radiation source (λ= 1.54 Å). The XPS measurements were performed on a PHI 5000 Versa Probe.

### 4.2.5 Fabrication of N-G-CNT-G and G-CNT-G based all-solid-state supercapacitors

Two as-synthesized thin films were used as two electrodes. Cu wire was connected to the electrode surface by conductive silver paste. A polymer gel (poly (vinyl alcohol) (PVA)/phosphoric acid ($H_3PO_4$), 1:1 wt%/wt%) was used as both electrolyte and separator. The polymer gel electrolyte was applied to the active electrode surface with 1 cm ×1 cm and dried in the oven for 2 hours. Finally, the all-solid-state supercapacitor was assembled by pressing two of the electrolyte-coated electrodes. Electrochemical measurements were performed on an electrochemical working station (CHI 760C, U.S.A.).

## 4.3 Results and discussion

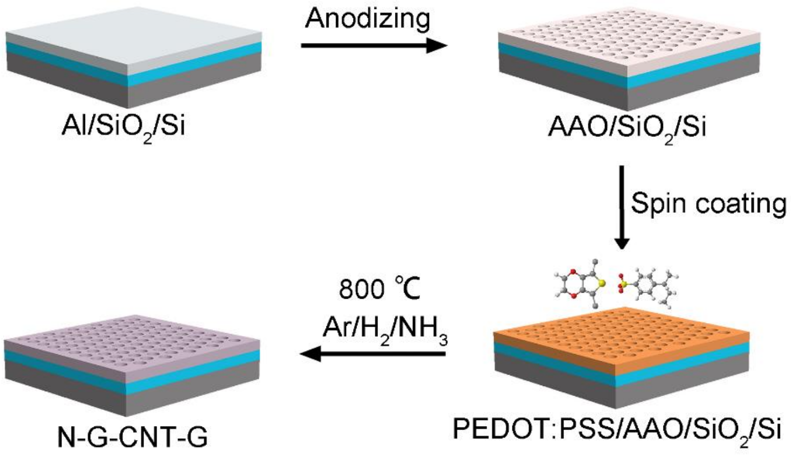

Figure 4.1 Schematic illustration of 3D N-G-CNT-G structure.

Schematic diagram of the fabrication process is described in Fig. 4.1. The AAO template with the thickness of 250 nm was formed on a silicon wafer by anodizing the sputter-coated Al film. The AAO template consisted of uniform nano-cylindrical pores vertically aligning to each other, and the average pore size is ca. 60 nm. Then PEDOT:PSS solution was spin coated onto the AAO template as the carbon precursor. The AAO templates before and after coating by the carbon precursor are showing the different colors in optical images in Figs. 4.2b and c. The prepared sample was subsequently put in the quartz furnace at 800 °C under the mixture of Ar/$H_2$/$NH_3$. During CVD growth, PEDOT:PSS were pyrolyzed, and the carbon atoms were deposited onto the AAO template with N doping. Finally, the uniform N-G-CNT-G thin film was formed, as seen in Fig. 4.2d. Both N-G-CNT-G and G-CNT-G thin films are easily integrated into double-layer all-solid-state supercapacitors.

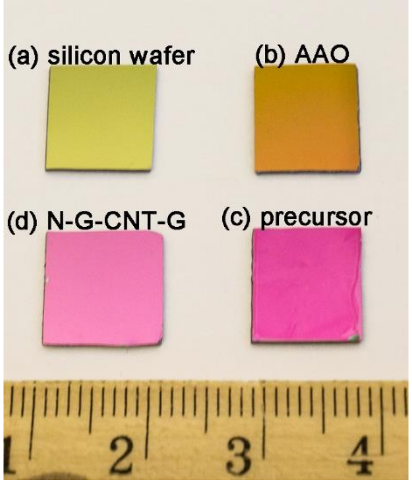

Figure 4.2 Photography of (a) silicon wafer, (b) AAO thin film, (c) spin-coated precursor and (d) N-G-CNT-G thin film via CVD growth.

The morphology of the N-G-CNT-G thin film was characterized by scanning electron microscopy (SEM). Fig. 4.3a is the SEM image of free-standing N-G-CNT-G. The enlarged cross-section (Fig. 4.3b) and top (Fig. 4.3c) views reveal the 3D structure made up of aligned holes with the average pore size of ca. 50 nm. Two-layer 3D structure (Fig. 4.3d) can also be fabricated by stacking AAO template and one-step CVD growth, which provide a potential opportunity to establish multi-layer 3D graphene-aligned CNT stereo structures.

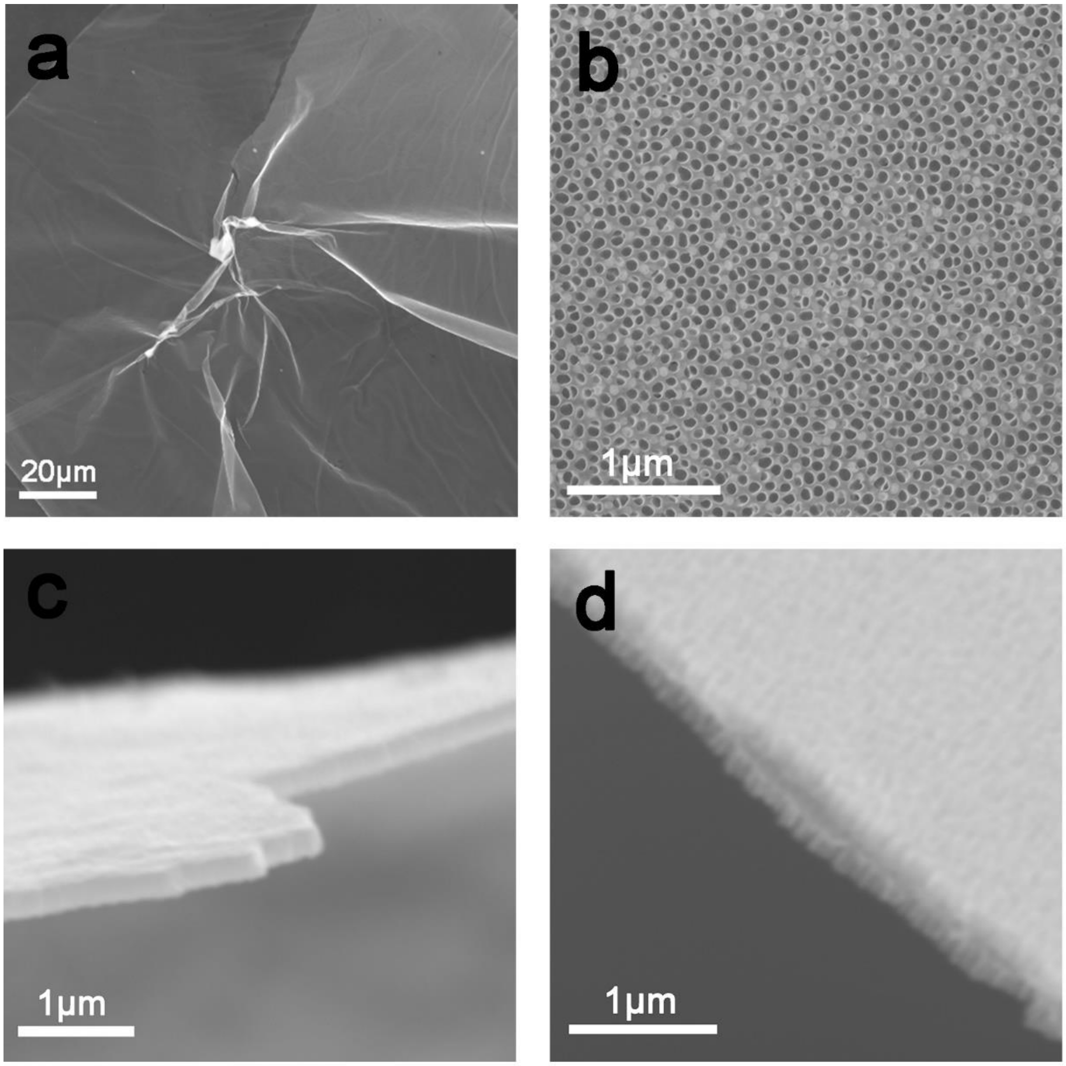

Figure 4.3 SEM images of (a) free-standing N-G-CNT-G on AAO template; (b) cross view; (c) top view; and (d) two-layer N-G-CNT-G-AAO stacking structure.

The unique 3D structure was further investigated by transmission electron microscopy (TEM). The N-G-CNT-G ordered structure with the homogenous holes is shown in Fig. 4.4a. The enlarged TEM image in Figs. 4.4b and c indicate the AAO template as a strong framework for N-G-CNT-G growth with the average hole diameter of ca. 60 nm, which is in good agreement with the SEM characterization in Fig. 4.3. The diameters of CNTs between the top and the bottom graphene layer are ca. 60 nm, suggesting the carbon atoms fully covered the AAO template on the top/bottom surface and along the hole walls during the CVD growth (Fig. 4.4d).

After removal of the AAO template, the integrated N-G-CNT-G 3D structure could be retained to the greatest extent due to CNTs' bridging between the top and the bottom graphene layers, as seen in Figs. 4.5a and b. The diameter of CNTs in Fig. 4.5c is ca. 60 nm, corresponding to the hole sizes in TEM images in Figs. 4.4c and d. Fig. 4.5d shows the thickness of graphene is ca. 10 nm, indicating the multilayer graphene. The junction of CNTs and graphene layers are revealed in Figs. 4.5e and f, showing the seamless connections between the CNTs and the graphene. As the 3D N-G-CNT-G structure was achieved by one-step CVD growth, the graphene-CNT-graphene is constructed with the covalent bonding that can enhance the electron transport and make the efficient electrolyte/ion diffusion. As a result, the electrochemical performance will be improved for the N-G-CNT-G based electrodes in a supercapacitor.

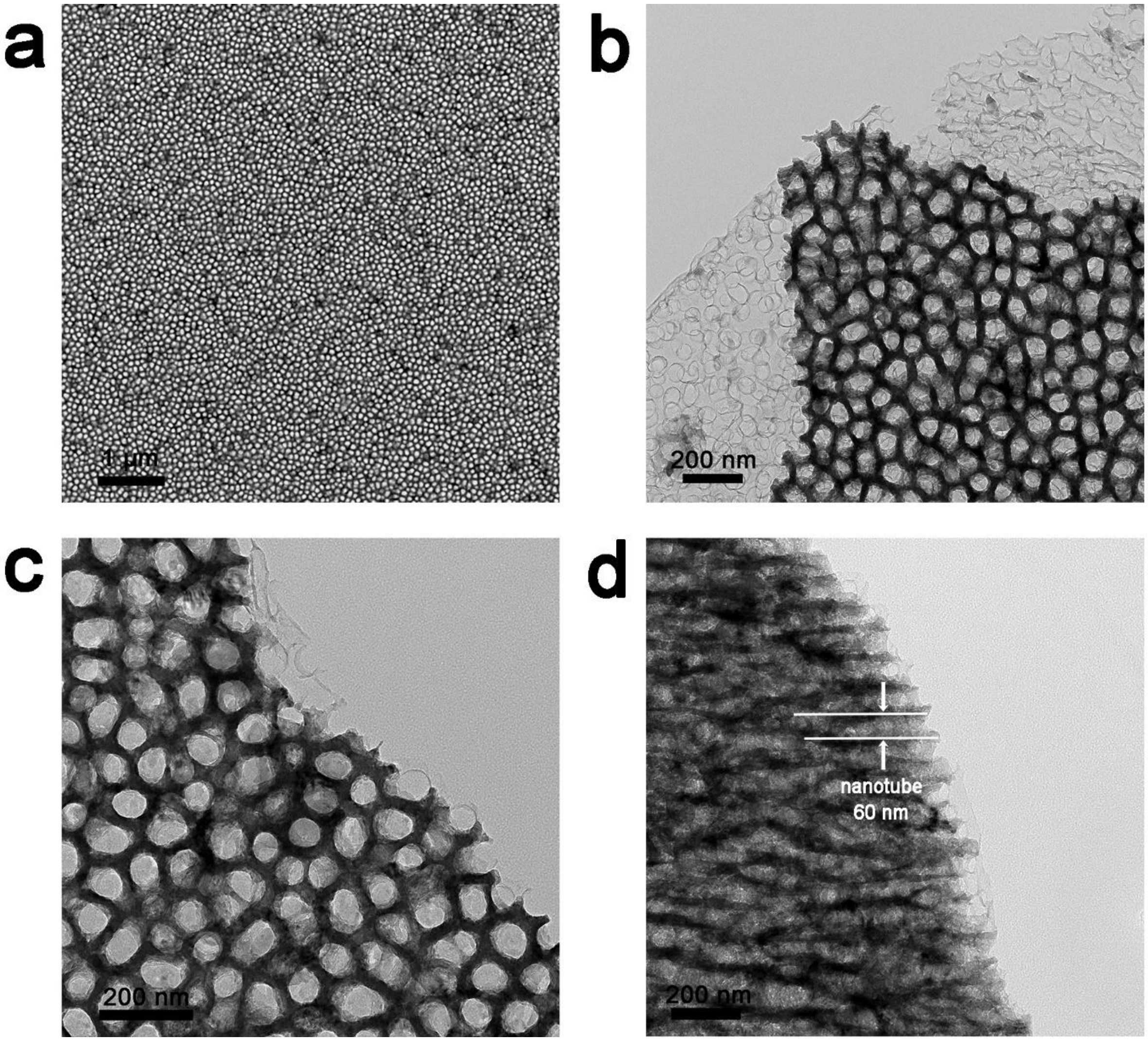

Figure 4.4 TEM images of N-G-CNT-G with AAO template: (a), (b) and (c) top view in different magnification; (d) cross-section view of N-G-CNT-G with AAO template.

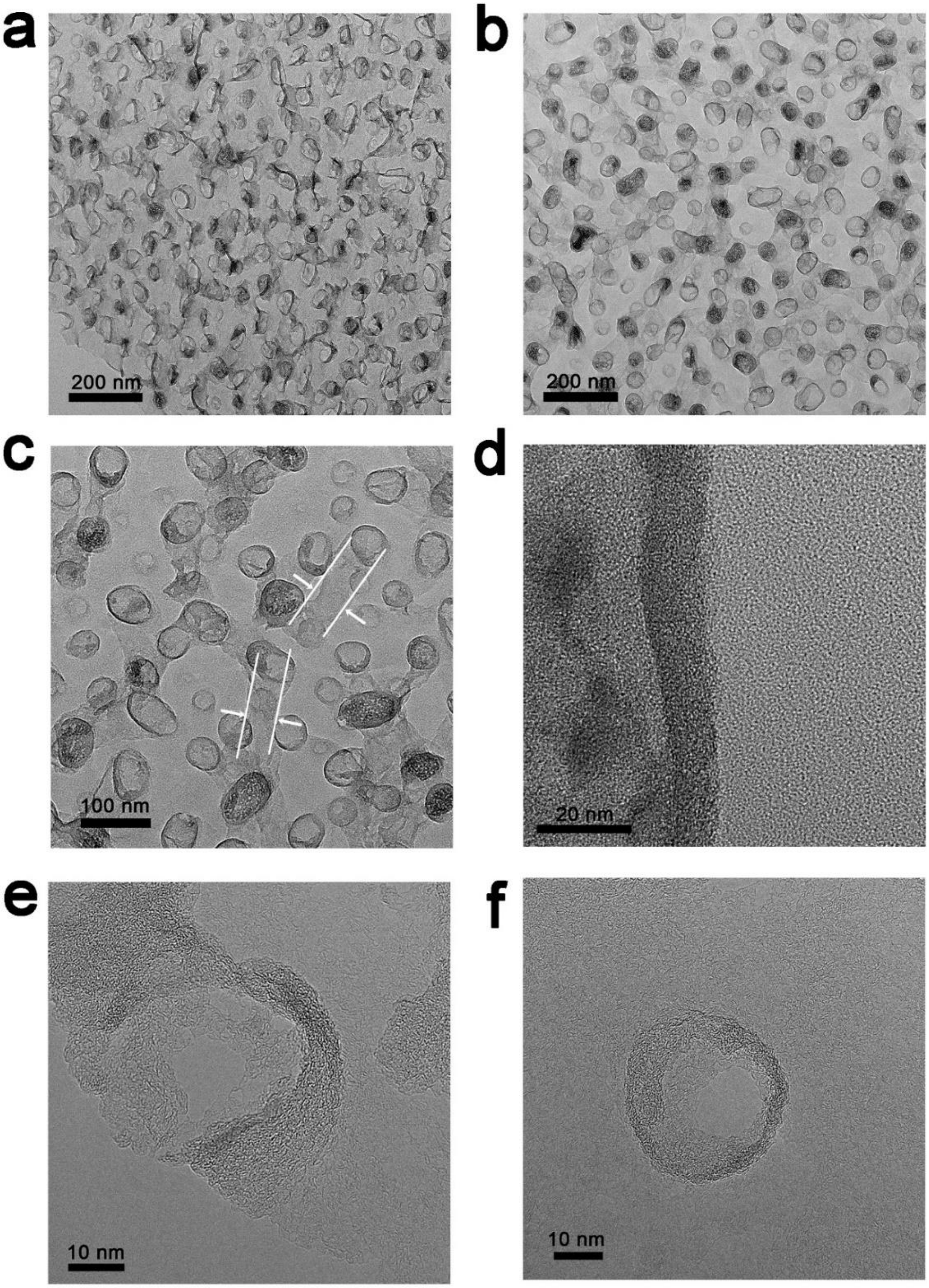
a
200 nm
b
200 nm
c
100 nm
d
20 nm
e
10 nm
f
10 nm

Figure 4.5 TEM images of (a-b) N-G-CTN-G after removal of AAO template; (c) enlarged view of CNTs under the top graphene layer; (d) the thickness of the graphene layer (ca. 10 nm); (e-f) joint of graphene and CNT indicating covalent bonding.

The obtained N-G-CNT-G samples were characterized by XRD and Raman spectroscopy. Fig. 4.6a is the XRD pattern of obtained N-G-CNT-G with a sharp graphite-structure peak at ca. 26° (JCPDS 41-1487), illustrating the high crystallization degree. Raman spectrum of the N-G-CNT-G thin film in Fig. 4.6b shows the pronounced defect-related D band and graphite-related G band[130, 160]. The weak but symmetric 2D band can also be observed, suggestion the multilayer graphene that is consistent with the TEM image in Fig. 4.5d.

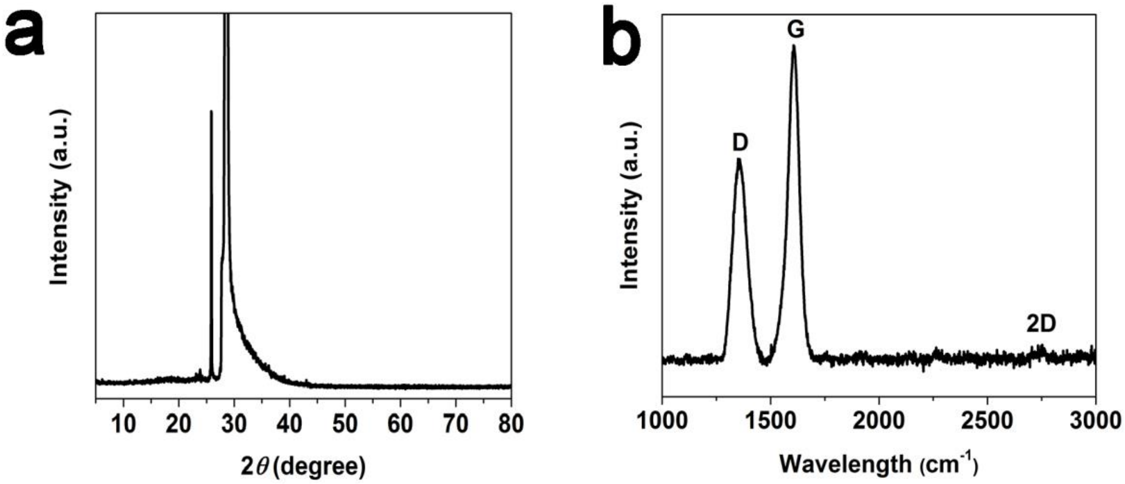

Figure 4.6 (a) XRD and (b) Raman spectrum of N-G-CNT-G.

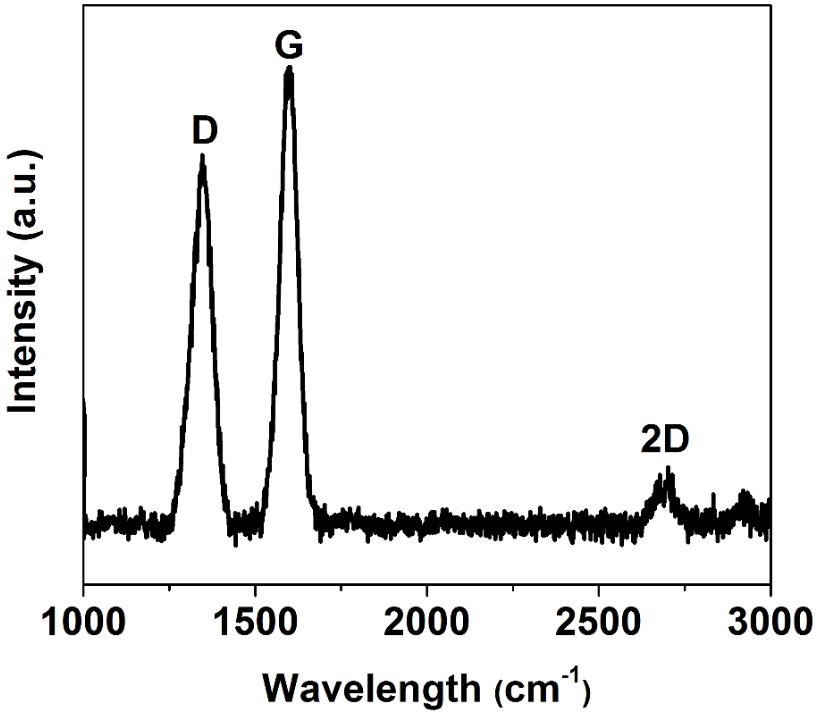

Figure 4.7 Raman spectrum of G-CNT-G.

In contrast, the Raman spectrum of the G-CNT-G sample in Fig.4.7 shows a stronger 2D band than that of the N-G-CNT-G sample, indicating a highly ordered stacking of graphene sheets. The lower 2D band in Raman spectrum of N-G-CNT-G can be attributed to the N doping process that can result in the structure distortion and induce more defects.

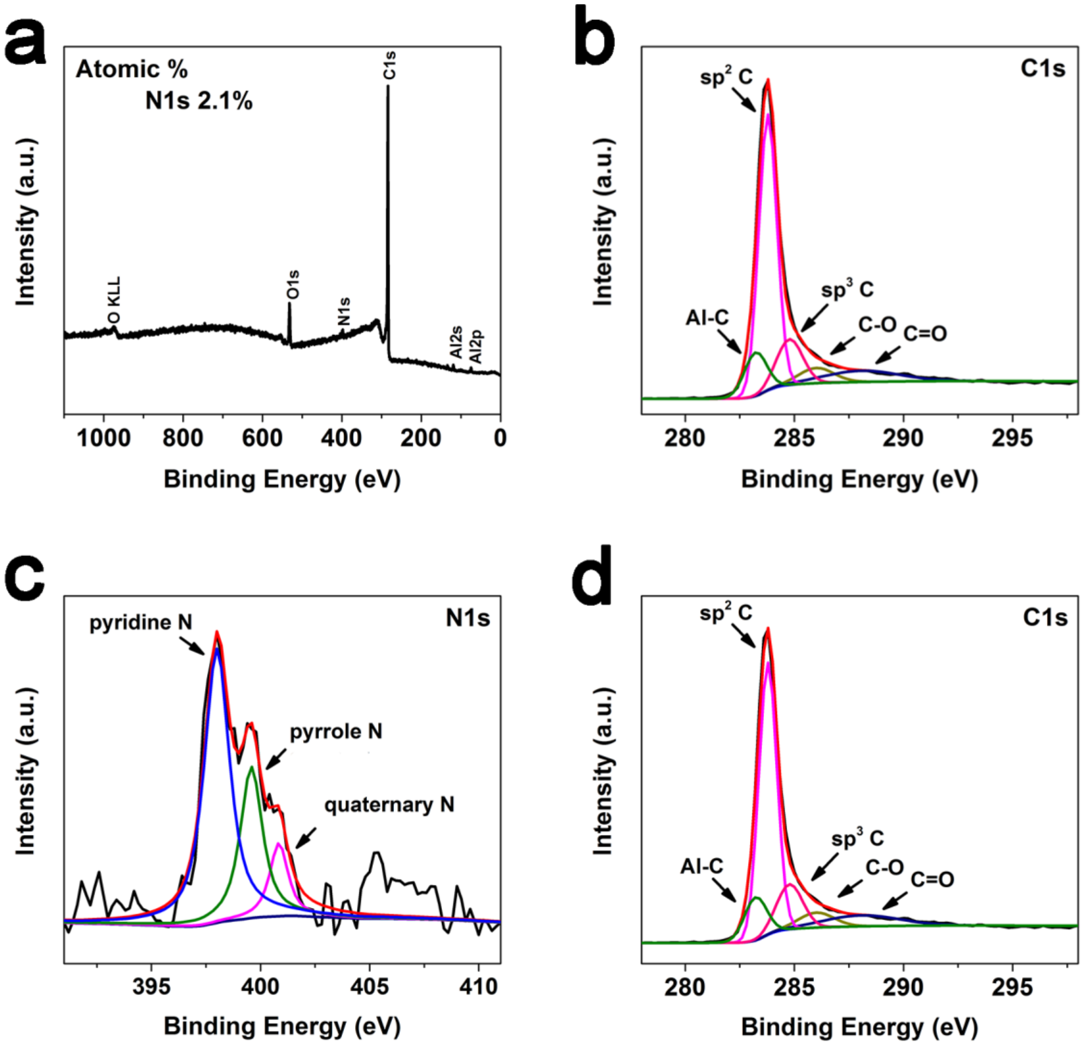

Figure 4.8 (a) XPS survey spectra of N-G-CNT-G; HR-XPS spectra of (b) C1s and (c) N1s of N-G-CNT-G; (d) HR-XPS spectra of C1s of G-CNT-G.

The X-ray photoelectron spectroscopy (XPS) was performed to investigate chemical compositions of the N-G-CNT-G. As shown in Fig. 4.8, the XPS survey spectrum for N-G-CNT-G shows a predominant C 1s peak at ca. 284 eV with N 1s peak at ca. 398 eV. The high-resolution XPS (HR-XPS) of C1s and N1s spectra are shown in Figs. 4.8b and c, respectively. The C1s peak can be resolved into sp$^2$ and sp$^3$ carbon at ~284.4 eV, C-O bonding at ~285.6.0 eV and hydroxyl carbon at ~288.6 eV[90], while HR-XPS spectrum of N1s peak reveals pyridinic N at 398 eV, pyrrolic N at 399.6 eV and quaternary N at ~400.8 eV [131] in the N-G-CNT-G sample, indicating part of N atoms are incorporating into carbon hexagonal rings. Compared to the HR-XPS C1s spectrum of G-CNT-G in Fig. 4.8d, the N-G-CNT-G inherits the graphite-like carbon bonding from G-CNT-G, which is accordance with the sharp G peaks in both Raman spectra of N-G-CNT-G in Fig. 4.6b and G-CNT-G in Fig. 4.7.

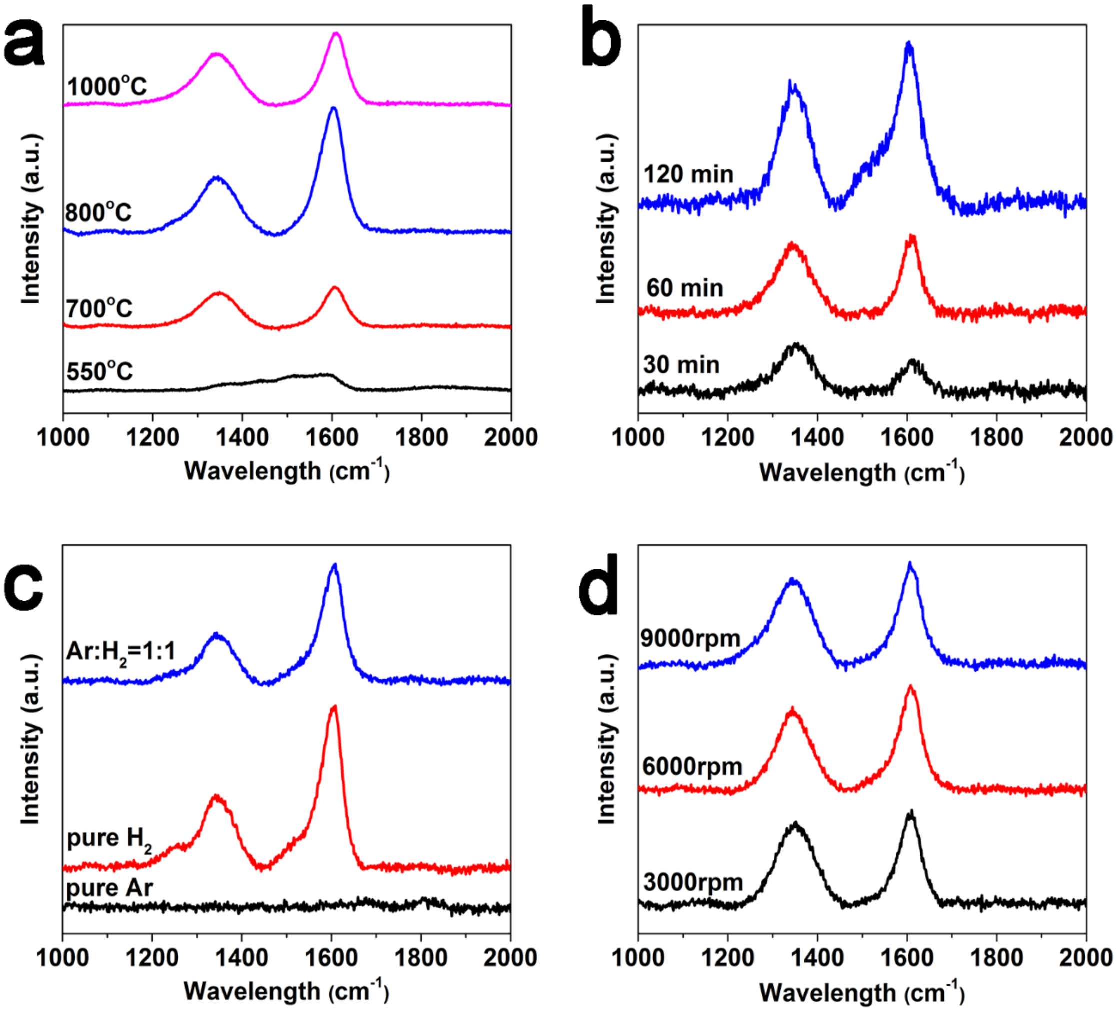

Figure 4.9 Raman spectra of G-CNT-G from (a) different growth temperature varied from 550 ℃, 700 ℃, 850 ℃, to 1000 ℃; (b) different growth time ranged from 30 min, 60 min to 120 min ; (c) different loading mass of precursor by varying the spinning rate; (d) the injected gas changed by only pure Ar (200 sccm), only pure $H_2$ (5 sccm), or by mixture of $H_2$ (5 sccm) and Ar (200 sccm)

It is worthy to notice that the graphitization degree of the G-CNT-G strongly determines its electric properties before N doping. On one hand, defects are favorably introduced to increase the electrochemical active sites. On the other hand, too many defects lead to the low-quality graphene, which would significantly reduce the electric conductivity. Therefore, the effects of the growth temperature, the growth time, the gas flow ratio and precursor loading mass of precursor, particularly in terms of their effects on the quality of the resultant G-CNT-G.

Fig. 4.9a shows Raman spectra of the G-CNT-G samples synthesized at 550 ℃, 700 ℃, 800 ℃ and 1000 ℃ in the same atmosphere (200 sccm Ar and 5 sccm $H_2$) for 120 min. At a relatively low CVD growth temperature (as low as 550 ℃), the weak G peak indicates a low graphitization degree. As the temperature raises, more precursors involve in the graphitization process that includes the decomposition of precursor and the formation of hexagonal carbon rings. Correspondingly, a remarkable G peak appears with defects-related D peak. The effect of the growth time on the quality of graphene on AAO template is more significant, as seen in Fig. 4.9b. As the temperature is set at 700 ℃, Raman spectra of G-CNT-G obtained from 30 min, 60 min and 120 min CVD growth show the ratio of D band to G band as 1.57, 0.88 and 0.74, respectively. It proves that a fraction of defects eliminates gradually and the graphitization and the crystallization are further intensified. Notably, hydrogen plays a critical role in the formation of graphene on the AAO template by using PEDOT:PSS as the carbon precusor. Fig. 4.9c shows comparisons for the Raman spectra of G-CNT-G obtained under pure Ar, pure $H_2$, and mixed Ar and $H_2$, respectively. It can be seen that the absence of $H_2$ resulted in the amorphous carbon. By contrast, there is a no clear effect of the precursor loading mass on the formation of graphene during the AAO template-assisted CVD growth (Fig. 4.9d).

### Electrochemical performance

The N-G-CNT-G thin films were obtained by one-step CVD growth so that the electron transport can be enhanced while more active sites induced by N-doping. Both the N-G-CNT-G and the G-CNT-G thin films were applied as electrodes for the symmetric solid-state supercapacitors.

The electrochemical performance of N-G-CNT-G based supercapacitor was analyzed by cyclic voltammetry (CV) and galvanostatic charge/discharge (GCD) testing. Fig. 4.10a shows the CV curve from 0 to 0.8 V with a broad range of scan rates with nearly a rectangular shape, which indicates an excellent capacitive behavior. The GCD curve in Fig. 4.10b is close to a triangular shape at different current density, suggesting the fast electron transporting and the sufficient ion diffusing via two electrodes. The N-G-CNT-G based supercapacitor exhibits an excellent long-term cycling at a constant current density of 0.5 μA (Fig. 4.10c). Since the mass of N-G-CNT-G based electrodes was too small to evaluate, the performance per geometrical area was used instead of gravimetric values. Thus the area specific capacitance ($C_{sp}$) was calculated using the equation:

$$C_{sp} = {}^{I\Delta t}\!/_{S\Delta V} \qquad (4\text{-}1)$$

where $I$ is the applied current, $\Delta t$ is the discharging time, $S$ is the area of the active electrode in a supercapacitor, and $\Delta V$ is the voltage window, respectively. Calculations from the GCD curves shown in Fig. 4.10b indicate that the areal specific capacitances are 231.7 μF $\mathrm{cm}^{-2}$ at the discharge current of 0.1 μA and 172 μF $\mathrm{cm}^{-2}$ at 2.0 μA respectively (Fig. 4.10d).

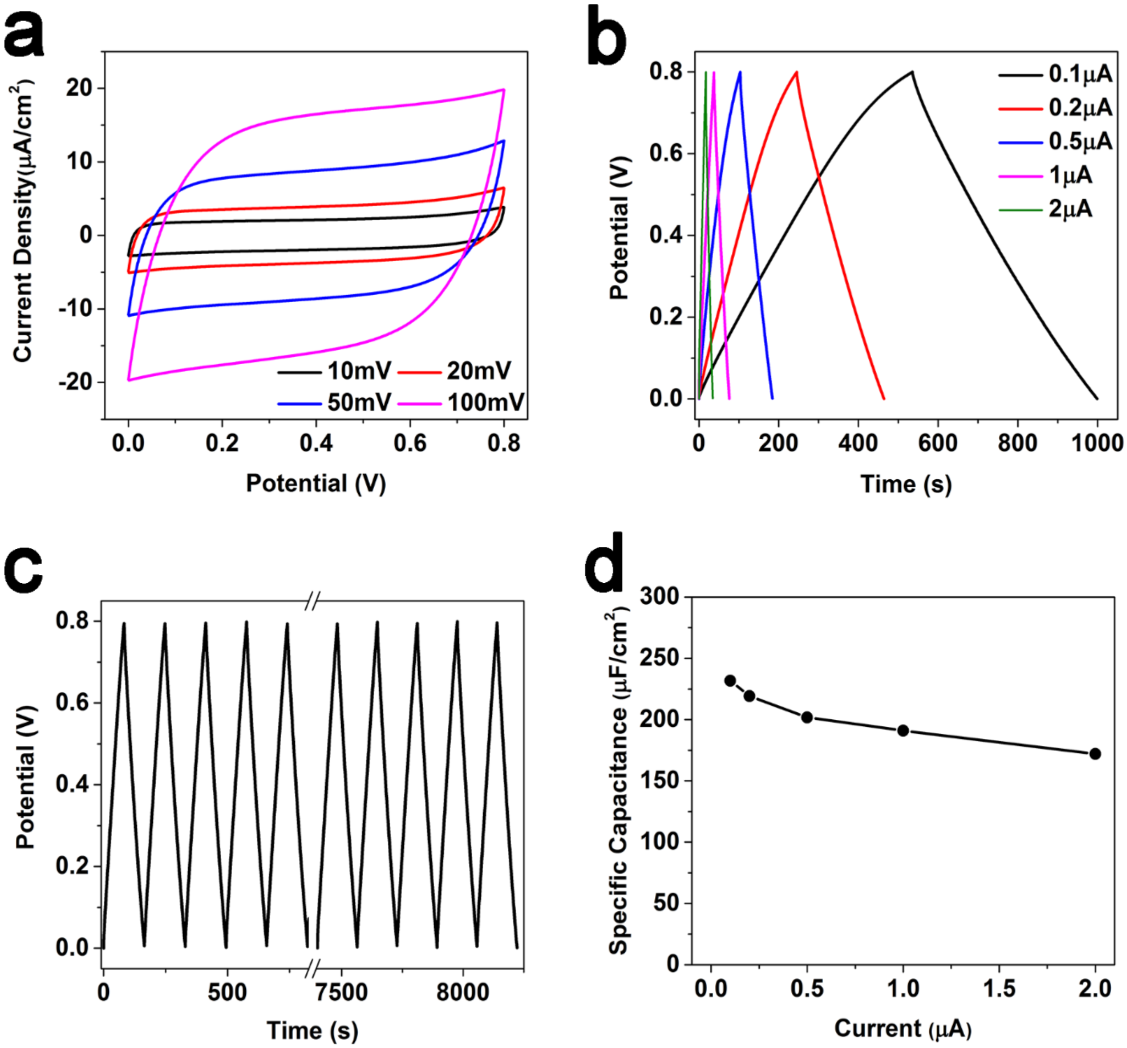

Figure 4.10 N-G-CNT-G based supercapacitor: a) CV curves at the scan rate from 10 to 100 mV $s^{-1}$ ; (b) Galvanostatic charge/discharge (GCD) curves of the device recorded at

different applied currents; (c) GCD curve at a constant current of 0.1 μA; (d) variation of specific capacitance as a function of the applied current.

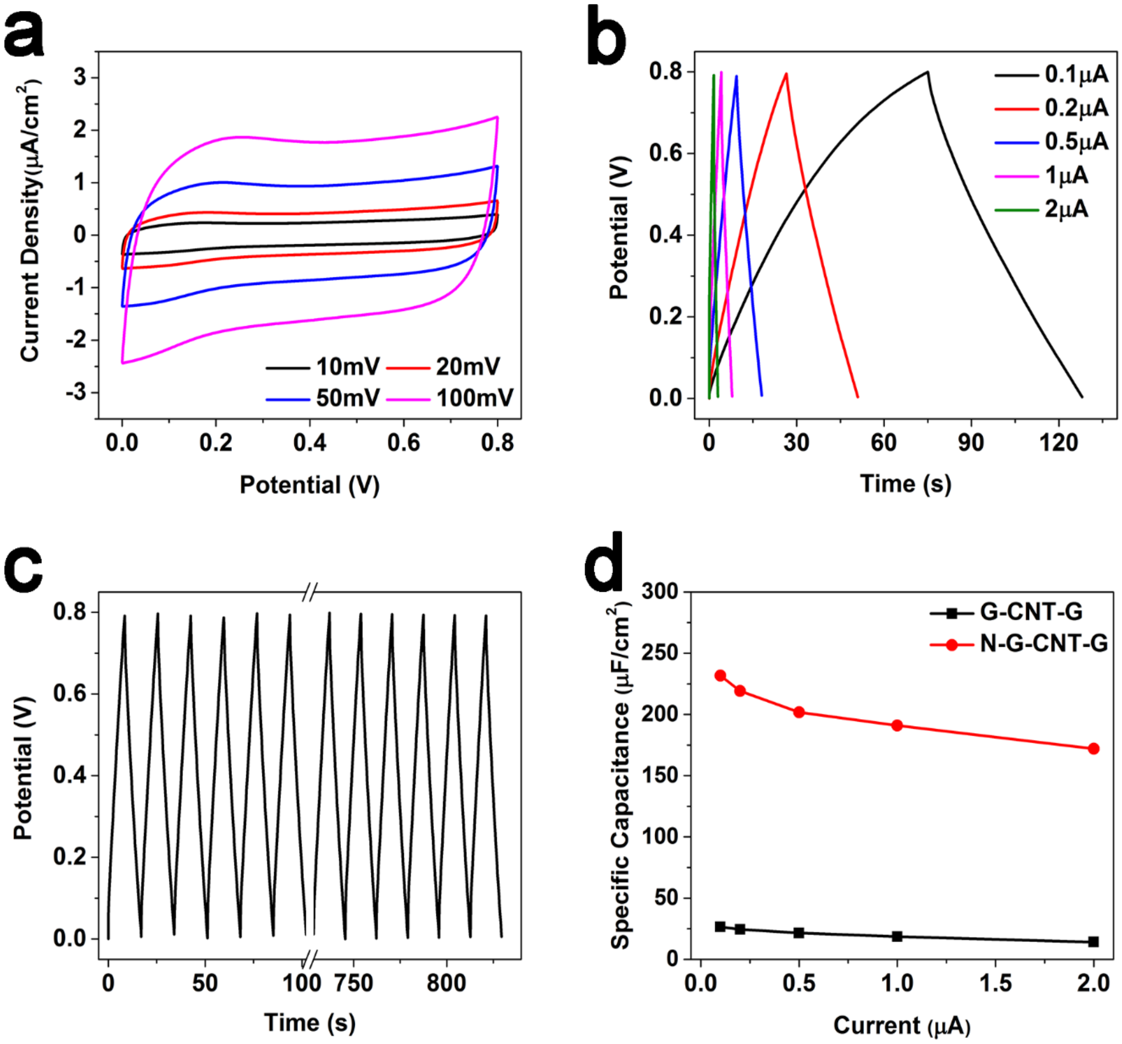

Figure 4.11 G-CNT-G based supercapacitor: a) CV curves at the scan rate from 10 to 100 mV s$^{-1}$ ; (b) Galvanostatic charge/discharge (GCD) curves of the device recorded at different applied currents; (c) GCD curve at a constant current of 0.1 μA; (d) variation of specific capacitance as a function of the applied current.

The G-CNT-G based supercapacitor was also studied for comparison. The CV curves in Fig. 4.11a show rectangular shape in the voltage range from 0 to 0.8 V at a various scan rates and the GCD curves in Fig. 4.11b also show the triangular shape at different current density. Fig. 4.11c demonstrates a stable cycle capability in the charge/discharge process. Therefore, G-CNT-G based supercapacitor exhibited a good all-solid-state symmetric Supercapacitor behavior as G-CNT-G based device due to the 3D graphene framework with sufficient diffusion pathway for electrolyte ions and fast electron transport.

However, it is apparent that the performance of N-G-CNT-G based supercapacitor is superior to that of G-CNT-G based device with a higher areal specific capacity (as seen in Fig. 4.11d) due to the N doping induced more active sites with an improved electron migration in the electrodes.

## 4.4 Conclusions

In summary, a simple one-step CVD fabrication approach to three-dimensional nitrogen doped graphene-CNT-graphene (N-G-CNT-G) structures has been developed. This resultant ordered N-G-CNT-G material endows the fast electron transport through the 3D framework, easy access to electrolytes, and sufficient active sites in the electrochemical reactions. The N-G-CNT-G based all-solid-state supercapacitors exhibit the excellent electrochemical performances with an area-specific capacitance of 231.7 $\mu$F cm$^{-2}$ at the discharge current of 0.1 $\mu$A, and a long-term cycle stability. The methodology developed in this study for unique 3D N-G-CNT-G material can be easily applicable to other doped thin-film or decorated composites for other energy storage devices, such as Li-ion batteries.

# Chapter 5

# Hierarchical $MoS_2$ decorated 3D graphene as anodes for lithium-ion battery

## 5.1 Introduction

With the increasing market needs for electrical vehicles (EVs), the demand for advanced lithium-ion batteries (LIB) with higher energy density has rapidly grown[1]. The development of anode nanomaterials has provided the potential opportunities to improve the performance of batteries with a high specific capacity and long cycle life[101]. Two-dimensional (2D) nanomaterials have been widely used as for electrode materials for LIBs because of their attractive properties within the ultrathin planar and ease with which they can be assembled into various three-dimensional (3D) architectures[20].

Graphene, the most representative 2D material, has attracted great attention as a promising LIB anode material due to its fast electron transfer, large surface area and environmental friendliness[3, 145]. Graphene-based anode materials exhibited a high specific capacity of 794-1054 mAh $g^{-1}$ as a result from Li-ion adsorption on both sides of atomic carbon sheet and the fast Li-ion diffusion with a lower barrier[136]. Furthermore, the 3D structure was established such as graphene gel and graphene foam to raise the ion storage capacity and achieve more efficient Li-ion diffusion in the batteries, which exhibited a high reversible capacity, high-rate capability and long cycle life[149, 161].

Transition metal dichalcogenides (TMDs) with analogous structures to graphite but relatively high theoretical capacities have also been investigated as potential anode materials for LIBs[71]. Among them, molybdenum disulfide ($MoS_2$) is a typical 2D material consisting of a S-Mo-S layered-structure and separated by the Van der Waals interaction[162]. Thin-layered $MoS_2$ based anode materials had been demonstrated to exhibit a high specific capacity, but suffered from a fast capacity degradation and low rate capability due to their low electric conductivity in c-direction and considerable strain during the cycling[163]. Many methods have been reported to relax the strain upon charging/discharging, such as restacking of $MoS_2$ to enlarge the interlayer spacing and lower the barrier of Li intercalation and improve the specific capacity to 800 mAh $g^{-1}$ [72]. However, the electrochemical performance of $MoS_2$ based LIB is still impeded by its intrinsic poor electric conductivity.

To address these issues, the 3D nanostructured $MoS_2$-graphene hybrids are proposed[70, 164]. In this regard, graphene can serve as an ideally epitaxial substrate for the nucleation and the growth of $MoS_2$, and provide an efficient pathway to enhance the electron transport and the ion diffusion in the hybrid nanostructure. In contrast, nano-layered $MoS_2$ can host Li-ions largely as its texture so that the hybrid $MoS_2$-graphene 3D nanostructure enables efficient lithiation and delithiation. Hence, the hybrid 3D $MoS_2$-graphene based anode materials can offer a series of advantages and keep the excellent intrinsic properties of the constituent graphene and $MoS_2$ respectively.

To date, the most common approach to synthesize $MoS_2$-graphene heterostructure is by mixing the precursor of 2D $MoS_2$ with reduced graphene oxide (rGO) in solution, and then get the $MoS_2$-graphene composites[68, 73, 165]. Nevertheless, this method would lead to restacked $MoS_2$, the mismatch of $MoS_2$ and rGO in c-direction, and the poor electric conductivity of rGO hampers the enhancement of electron transport. Since graphene from CVD has better electron transport property than that of rGO, $MoS_2$ nanosheet is synthesized on graphene foam from nickel foam via CVD method[166]. As the morphology of heterostructure and the interaction between $MoS_2$ and graphene can affect the electrochemical performance, it is highly desirable to develop a good 3D $MoS_2$-graphene heterostructure with superior performance as anode materials in lithium ion batteries.

Herein, we developed a $MoS_2$ decorated 3D graphene ($MoS_2$-3DG) thin film with an ordered structure by chemical vapor deposition, in which the graphene sheets could act as ideal substrates for the high-quality-$MoS_2$ growth. With the vertically aligned holes in the 3D graphene, the newly-developed $MoS_2$-3DG offered a sufficient contact to the electrolyte and the 3DG served as an interconnected conductive matrix for the current collector. When used as an anode in LIBs, therefore, the resultant $MoS_2$-3DG nano thin film exhibited a high specific capacity of 1560 mAh $g^{-1}$ at 0.1 A $g^{-1}$, a good rate capacity of 1100 mAh $g^{-1}$ at 1 A $g^{-1}$ and a long cycle life.

## 5.2 Experimental section

### 5.2.1 AAO template preparation

250 nm aluminum was sputtering coated (Denton Vacuum Explorer 14) onto a 1 cm × 3 cm silicon wafer (with 200 nm silicon oxide coated, Silicon Quest International, Inc.). The thin film was anodized with a constant voltage of 40 V in 0.3 M oxalic acid at 0 ℃ for 1 hour to form anodic porous aluminum oxide (AAO) template. A slice of platinum (1 cm × 3 cm) was supplied as a counter electrode, and the distance between the working and counter electrode is 3 cm. After anodization for 1 hour, the pores of AAO template were

further expanded by chemical etching in the 0.1 M phosphoric acid ($H_3PO_4$, 85%, Fisher Scientific) solution for 30 min via water bath at 40 ℃.

### 5.2.2 CVD synthesis of 3DG

The AAO template was placed at the center of quartz tube in the furnace. 200 sccm argon (Ar, 99.99% purity, Airgas) and 10 sccm hydrogen (H2, 99.999% purity, Airgas) were introduced into the quartz tube for 30 min. Then the temperature was raised to 700 ℃ and kept for 5 minutes to pre-heating AAO template. Subsequently, 20 sccm acetylene ($C_2H_2$, 99.6% purity, Airgas) was injected with Ar and $H_2$ for 30 min to grow the graphene on AAO template. After rapid cooling down, the 3DG was formed.

### 5.2.3 CVD synthesis of $MoS_2$-3DG

The precursor ammonium tetrathiomolybdate ($(NH_4)_2MoS_4$, Sigma-Aldrich) was dissolved in N,N-dimethylformamide (DMF, anhydrous, 99.8%, Sigma-Aldrich) at a concentration of 0.1 mM. The obtained solution was spin-coated on the 3DG surface with various spinning speeds to change the thickness of precursor (detailed information). The 3DG with precursor was put in the center of the quartz tube and heated at 50 ℃ for 30 min to remove the residual DMF. Then, the sample was further heated to 400 ℃ with a ramping rate of 5 ℃ $min^{-1}$ and kept at 400 ℃ for 15 min. After rapid cooling down, the resulting $MoS_2$-3DG was formed.

### 5.2.4 Transfer $MoS_2$-3DG thin films

Poly(methyl methacrylate) (PMMA, Sigma-Aldrich) was dissolved in anisole (anhydrous 99.7%, Sigma-Aldrich) at a concentration of 6 wt%. After CVD synthesis, $MoS_2$-3DG with AAO/$SiO_2$ wafer was spinning coated by PMMA solution at 5000 rpm for 1 min. The sample was baked under vacuum at 80 °C for 1 hour for PMMA curing and immersed in 20 wt% hydrofluoric acid (HF, Sigma-Aldrich, 48 wt% in $H_2O$) to remove AAO and $SiO_2$ wafer, and then in heated acetone at 70 °C to remove PMMA. Finally, the obtained $MoS_2$-3DG thin film can be transferred to various substrates such as PDMS or battery case.

### 5.2.5 Characterization

Scanning electron microscope (SEM) images were conducted on a JSM-7001F SEM unit. Transmission electron microscopy (TEM) images were collected from an FEI Tecnai G2 T20 (120 kV). The element mappings were carried out on a STEM unit with HAADF detector (FEI Tecnai G2 F30, 200kV). Raman spectra were collected using a Raman spectrometer (Renishaw) with a 514-nm laser. The X-ray powder diffraction (XRD) patterns were obtained on a Bruker D8-advance X-ray powder diffractometer with Cu Kα radiation source (λ= 1.54 Å). The XPS measurements were performed on a PHI 5000 Versa Probe.

### 5.2.6 Battery assembly

The $MoS_2$-3DG thin film was transferred to battery case directly to fabricate CR2032 coin cells. The batteries were assembled in the Ar-filled glove box by stacking $MoS_2$-3DG thin film as anode, a porous polypropylene film as separator, Li foil as counter electrode and reference electrode The electrolyte was 1 M $LiPF_6$ in a mixture of ethylene carbonate (EC), diethyl carbonate (DEC) and dimethyl carbonate (DMC) (1:1:1).

## 5.3 Results and discussion

The synthesis of $MoS_2$-3DG nano thin film is depicted in Fig. 5.1. The sputter-coated aluminum (250 nm) is anodized in 0.3 M of oxalic acid at 40 V to form the porous anodic aluminum oxide (AAO) template (1 cm × 3 cm) on a silicon wafer. The AAO template is placed in the quartz furnace, and hydrogen and acetylene were introduced with the temperature at 700 ℃ for 30 min. After 3DG had been grown on AAO template, 10 mM of $(NH_4)_2MoS_4$ in DMF was spinning coated on the surface of 3DG as a precursor. The 3DG-AAO template with $((NH_4)2MoS_4$ is heated up to 400 ℃ at a ramping rate of 5 ℃ $min^{-1}$ and maintained for another 15 min to grown $MoS_2$ nanosheet on 3DG.

The free-standing $MoS_2$-3DG thin film is highly transparent and can be transferred to PDMS substrate (Fig. 5.2), demonstrating the potential application in wearable and transparent energy device.

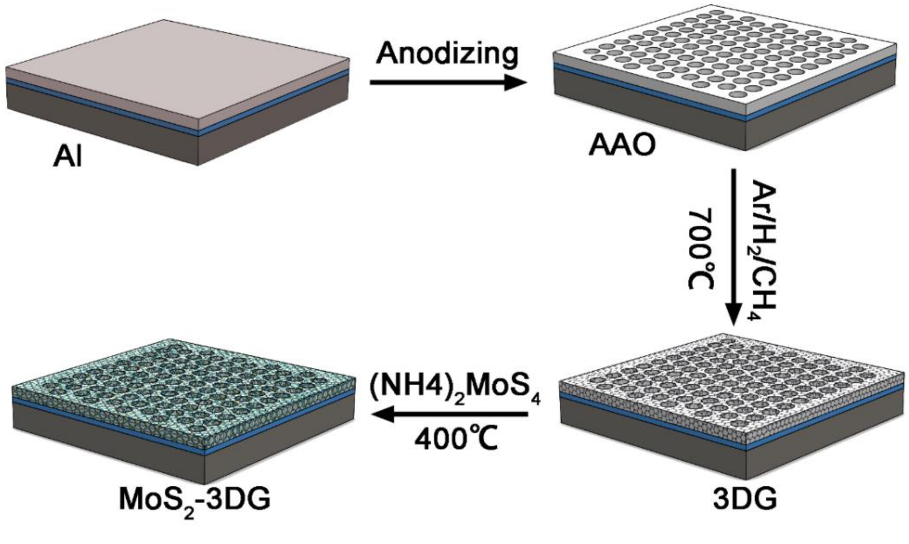

Figure 5.1 Schematic illustration of synthesis of $MoS_2$-3DG

Figure 5.2 Photo of transparent $MoS_2$-3DG thin film on PDMS.

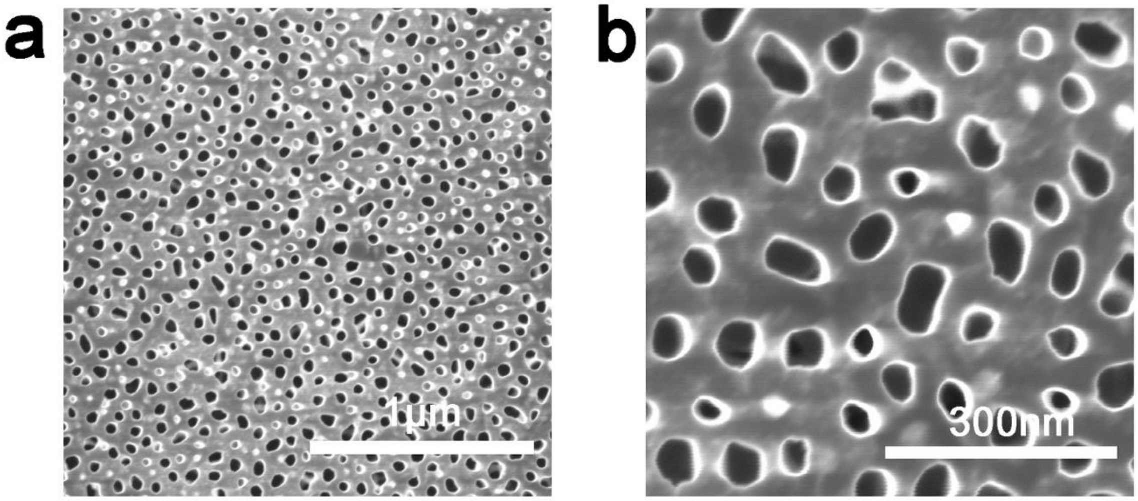

Figure 5.3 (a) and (b) SEM images of $MoS_2$-3DG with AAO template under different magnification.

The morphology and nanostructure of the $MoS_2$-3DG film were characterized by scanning SEM. Figs. 5.3a and b show the typical morphology of $MoS_2$-3DG on AAO template surface. The pore size ranged from 50 to 100 nm. $MoS_2$ nanosheet is grown along the graphene surface with binder-free contact, and the 3DG fully covers the AAO template.

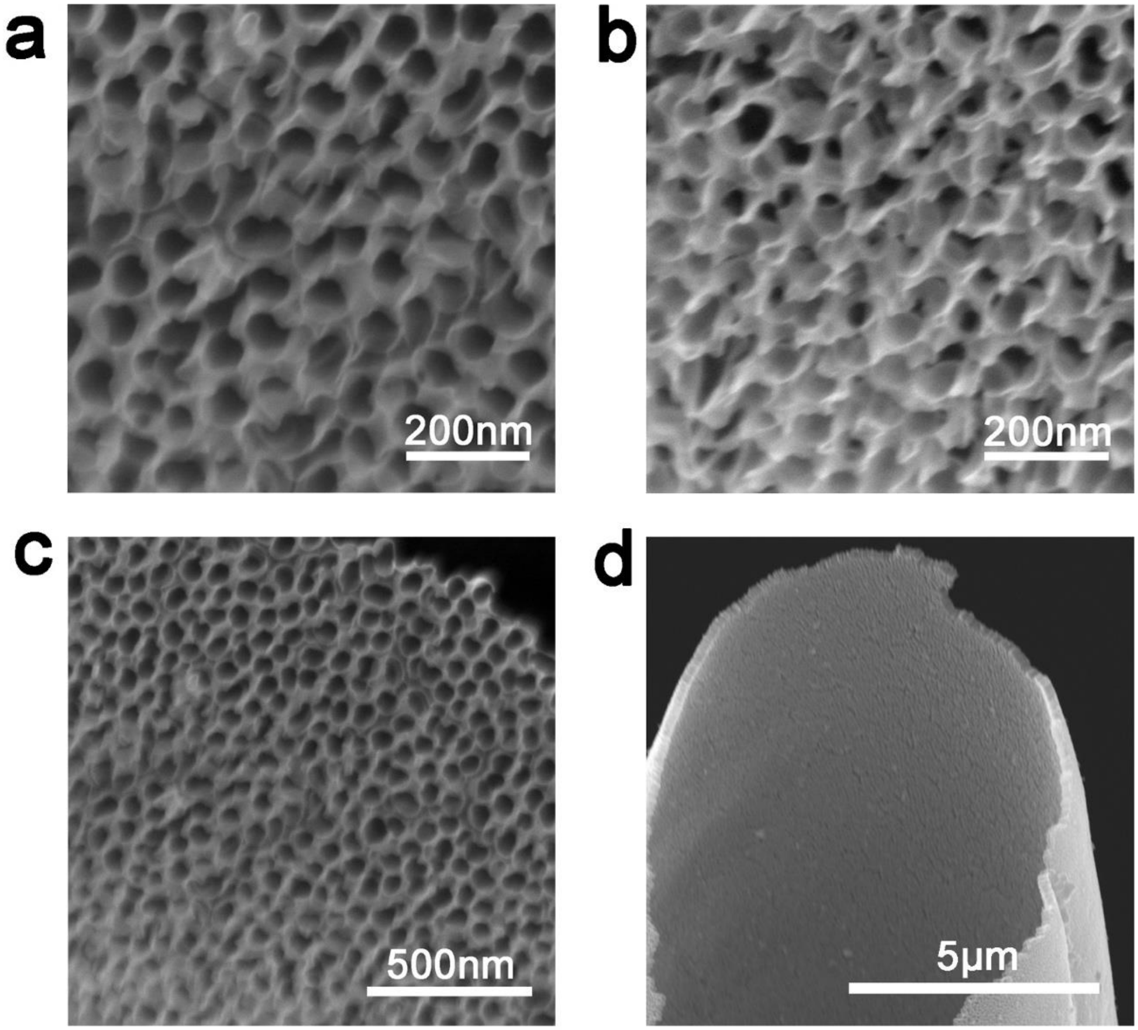

Figure 5.4 SEM images of the free-standing $MoS_2$-3DG thin film after removal of AAO templates under different magnification.

After removal of the AAO template, the $MoS_2$-3DG thin film could retain the ordered 3D structures. Figs. 5.4a-c show the vertically aligned holes with an average diameters of ca. 50-100nm in the 3D architecture, indicating the strong 3D graphene matrix and complete replica of AAO structure. With this method, the large-scale $MoS_2$-3DG thin film can be achieved, as seen in Fig. 5.4d.

Transmission electron microscopy (TEM) was performed to characterize the heterostructure of $MoS_2$-3DG. The $MoS_2$-3DG hybrid thin film was transferred to TEM grid and dried at room temperature. $MoS_2$-3DG heterostructure was revealed by TEM image in Fig. 5.5a, showing the highly ordered $MoS_2$ decorated 3D graphene structures. The high-resolution TEM (HRTEM) image in Fig. 5.5b illustrates the seamless attaching of $MoS_2$ nanosheets on 3D graphene with the layered crystal lattice structure. As marked in the HRTEM image, the lattice plane spacing of $MoS_2$ is 0.19 nm, which is corresponding to (105) plane. The obviously $MoS_2$ polycrystalline structure in Fig. 5.5c can be further confirmed via the selected area electron diffraction (SAED) pattern in Fig. 5.5d.

The corresponding elements (C, N, Mo, and S) mapping images in Fig. 5.6 show the $MoS_2$ nanosheets attached on 3DG with a low distribution, indicating the integrated 3DG framework is retained and the $MoS_2$ nanosheets can be sufficiently utilized for Li intercalation/deintercalation.

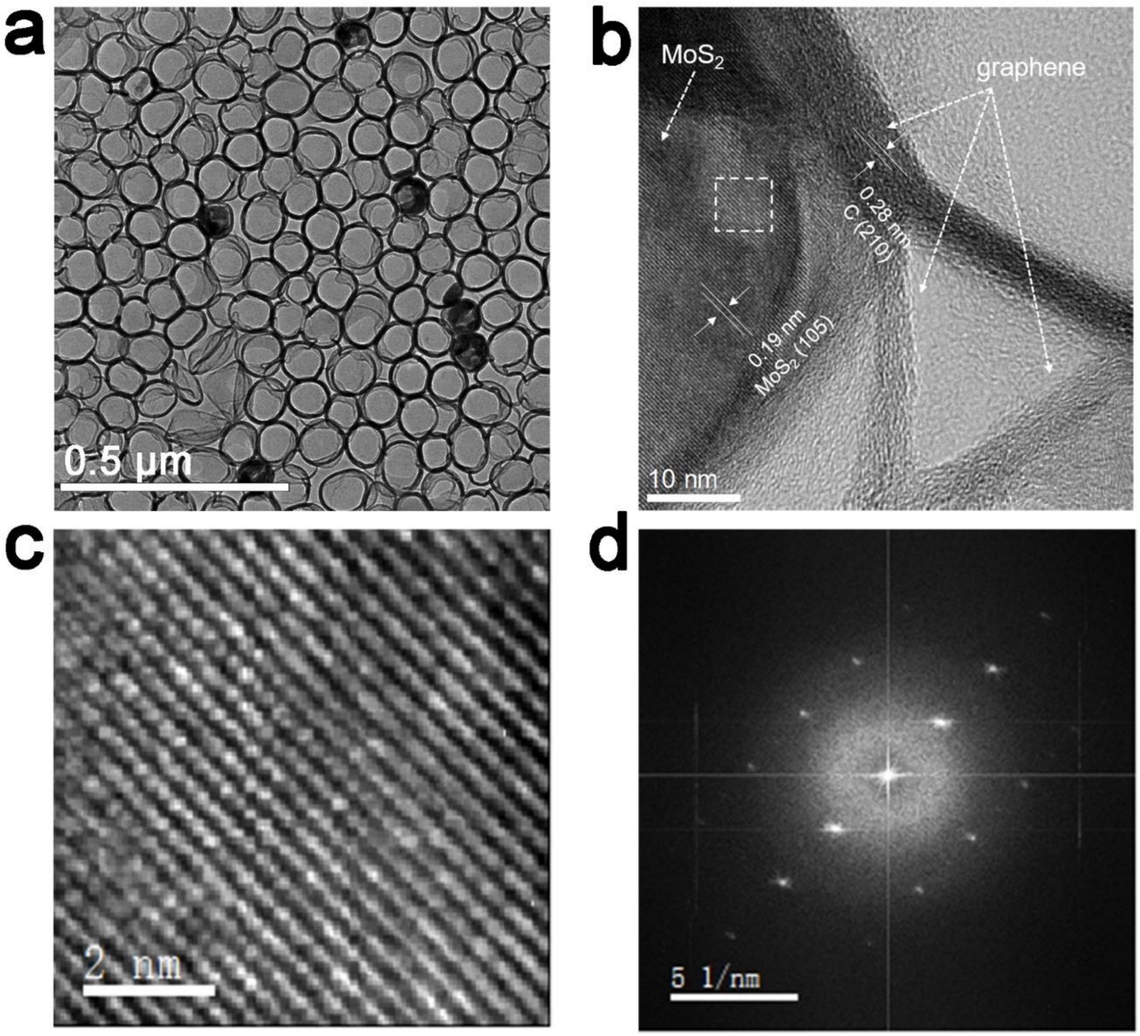

Figure 5.5 (a) TEM images of MoS$_2$-3DG; (b) HRTEM image of MoS$_2$ nanosheet layers with orientation along (105) and graphene nanosheet layers with orientation along (210); (c) HRTEM image of MoS$_2$ nanosheet plane; (d) selected area electron diffraction (SAED) pattern.

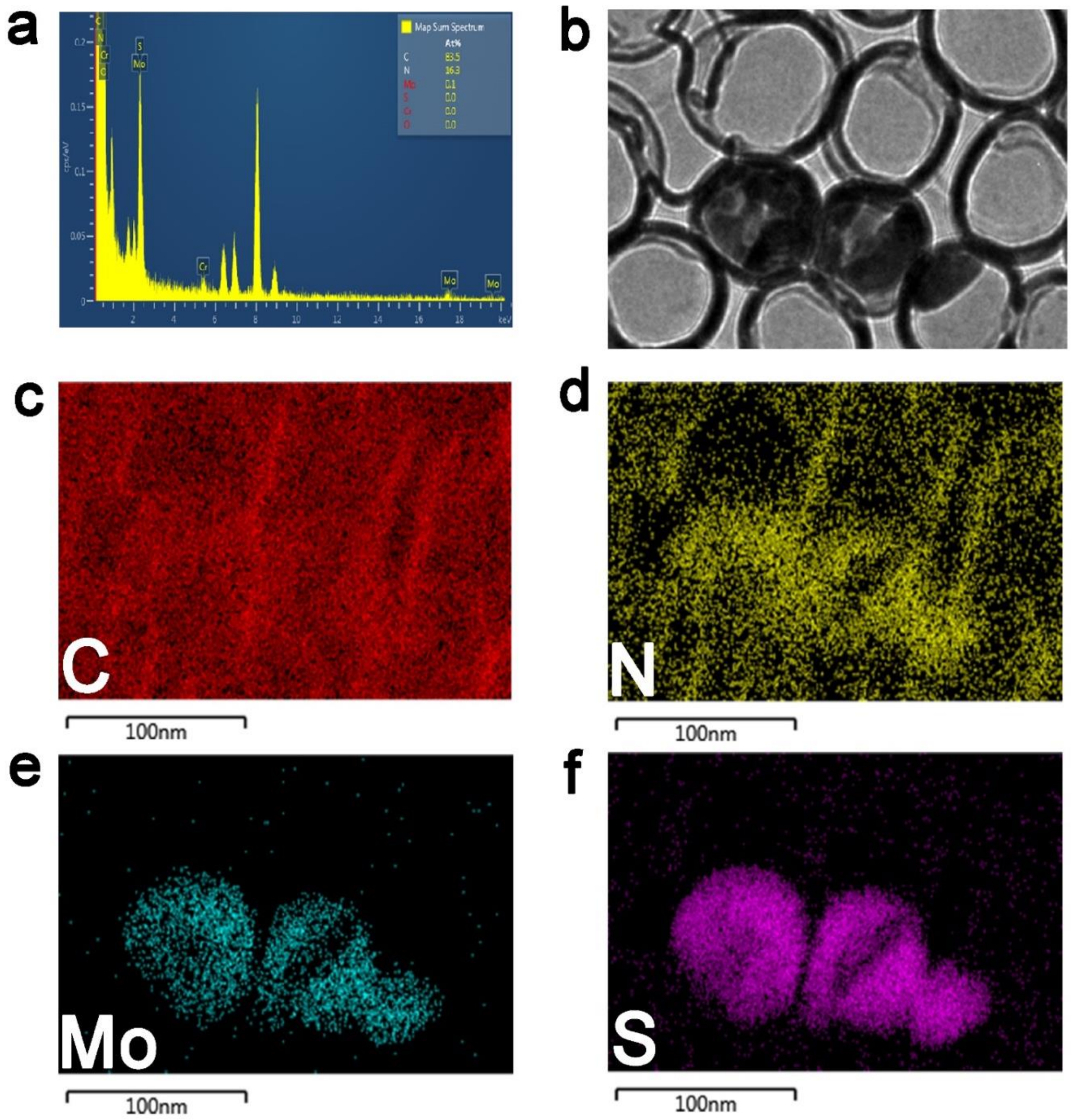

Figure 5.6 Element (C, N, Mo, and S) mapping of $MoS_2$-3DG.

The $MoS_2$-3DG heterostructures were further investigated by Raman spectroscopy and X-ray diffraction (XRD). Raman spectrum of 3DG in Fig. 5.7a shows a sharp D peak and G peak at 1351 $cm^{-1}$ and 1607 $cm^{-1}$, respectively, with a D to G peak ratio of 0.71. In Fig.

5.7b, Raman spectrum of $MoS_2$-3DG shows the peak at 382 $cm^{-1}$ and 407 $cm^{-1}$, which are attributed to characteristic in-plane Mo-S phonon mode $E_{2g}^{1}$ and out-of plane Mo-S phonon mode $A_{1g}$ [167] for $MoS_2$ crystal on 3DG respectively (also seen in Fig. 5.7c). The Raman spectra also displays D (1347 $cm^{-1}$) and G (1606 $cm^{-1}$) peaks of graphene with a ratio of 0.64, indicating a high graphitization degree[160]. Comparatively, the $I_D/I_G$ value of $MoS_2$-3DG is lower than that of 3DG, indicating that the defects on graphene was relatively decreased to improve the ion transport and 3D graphene structure is not deteriorated during the growth of $MoS_2$. The $MoS_2$-3DG crystal heterostrucutre can also be confirmed by XRD characterization.

The XRD patterns of 3DG and $MoS_2$-3DG in Fig. 5.7d both show the sharp diffraction peaks of graphitic carbon at ca. 26°, illustrating the high crystallization degree of 3D graphene framework. In the XRD pattern of $MoS_2$-3DG, the peaks of the (002), (100), (110) and (105) planes of $MoS_2$ with a hexagonal structure (JCPDS 37-1492) can also be observed.

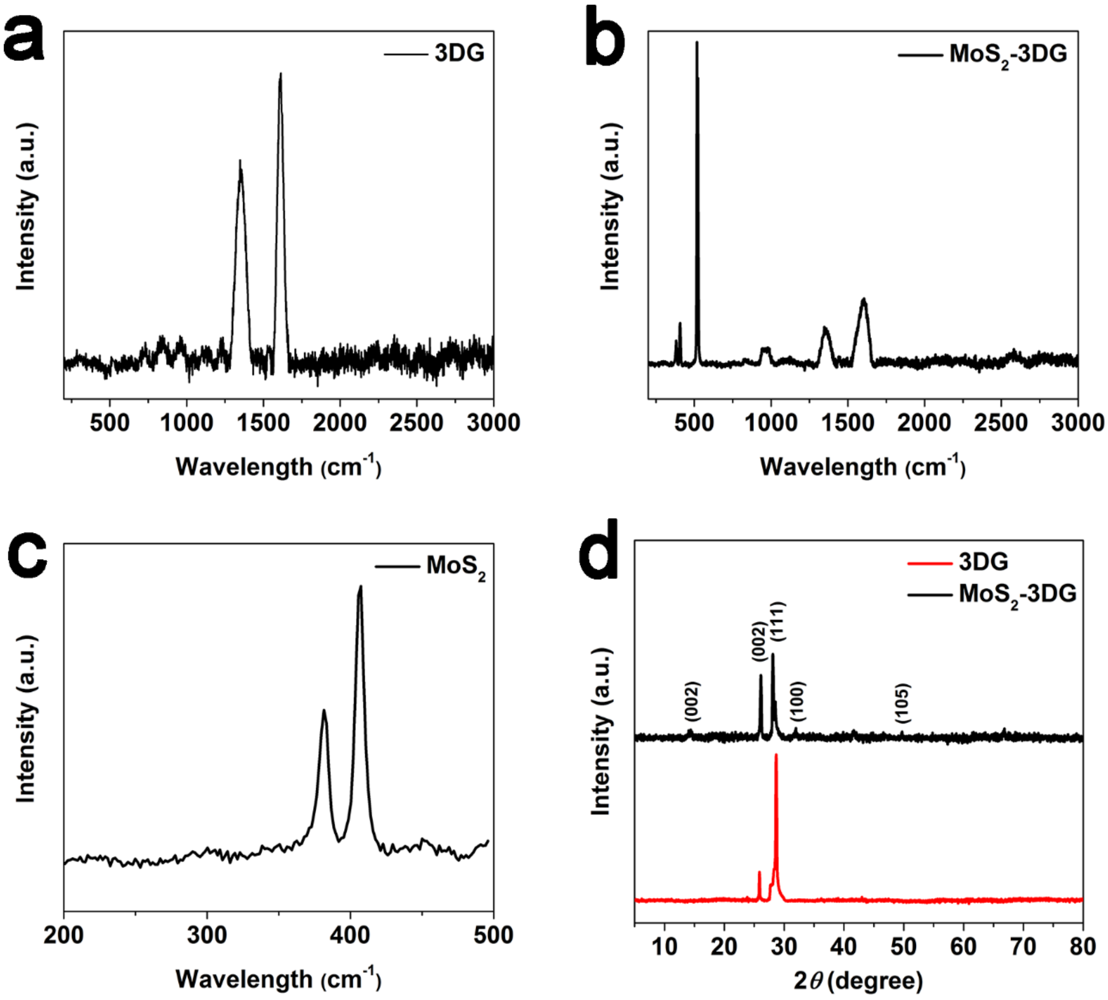

Figure 5.7 (a) Raman spectrum of 3DG; (b) Raman spectrum of $MoS_2$-3DG; (c) Raman spectrum of $MoS_2$; (d) XRD patterns of 3DG and $MoS_2$-3DG.

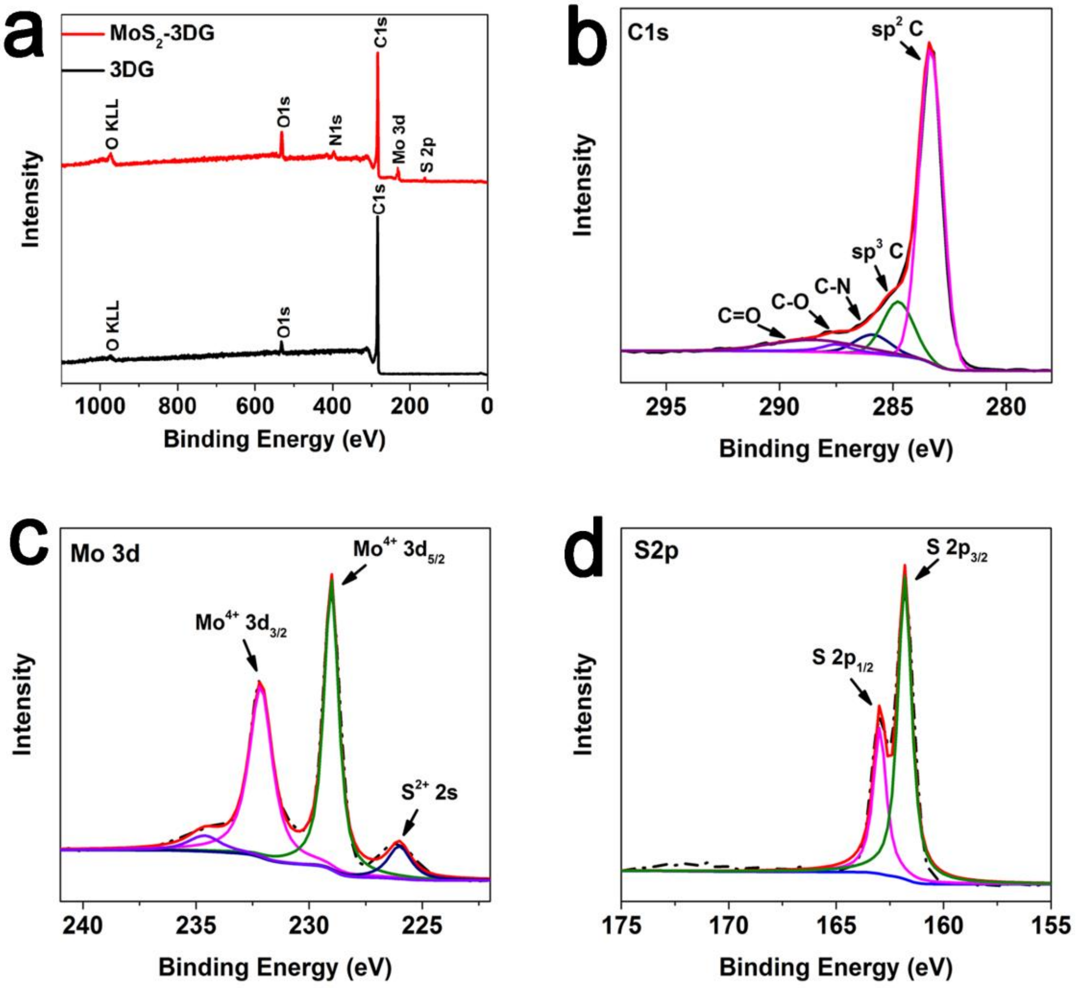

Figure 5.8 (a) XPS survey spectra of $MoS_2$-3DG and 3DG; high resolution XPS spectra of (b) C 1s, (c) Mo 3d, (d) S 2p.

The chemical composition of the as-synthesized 3DG and $MoS_2$-3DG films can be determined by X-ray photoelectron spectroscopy (XPS). The XPS survey spectrum in Fig. 5.8a shows a sharp C1s peak, Mo 3d peak, and weak S 2p peak. Since the precursor to fabricate $MoS_2$ nanosheets is $(NH_4)_2MoS_4$, nitrogen elements would be doped in the 3D graphene. The doping of N elements can introduce active sites to improve the electrochemical performance. Figs. 5.8b, c, and d show the high-resolution XPS spectra of C1s, Mo3d, and S2p, respectively. The C1s peak can be resolved into $sp^2$ carbon at ca. 284 eV, hydroxyl carbon C-O at ca. 285.2 eV and carbonyl carbon C=O at ca. 287.6 eV, and metal carbide at ca. 283.2eV. From the high-resolution XPS spectrum of Mo 3d, the peaks of $Mo^{4+}$ 3d 3/2 and $Mo^{4+}$ 3d 5/2 are located at 232.2eV and 229 eV in $MoS_2$ respectively[168]. The peak at 226 eV can be attributed to S 2s. The peaks in Fig. 5.8d are ascribed to S 2p1/2 and S 2p3/2 in $MoS_2$ [169]. The XPS results illustrated that no oxidation of Mo is observed and C-Mo bond is formed in $MoS_2$-3DG films.

The growth mechanism of $MoS_2$-3DG heterostructure is studied by characterizing the morphology via SEM. The different dose of $(NH_4)_2MoS_4$ were spinning coated on 3DG before CVD growth with various speeds from 1000, to 3000, and then 5000 rpm. After CVD growth at 400 °C for 15 min, the covered area of $MoS_2$ on 3DG increased with abundant edges, which are useful for electrochemical reaction (reference), as seen in Figs. 5.9a, b, and c. When too much precursor was loaded, the thick $MoS_2$ crystal flakes were formed and fully covered the 3DG surface with the graphene as an excellent conductive matrix, as seen in Fig. 5.9d.

The Raman spectrum in Fig. 5.10 also demonstrates the strong peak of $MoS_2$ and the inconspicuous peaks of graphene. Since the 3DG is served as a conductive matrix, while $MoS_2$ can improve the storage of $Li^+$ ion, the structure of the uniform thin sheet of $MoS_2$ decorated and binder-free anchored on 3DG is optimal as anode materials in lithium ion batteries.

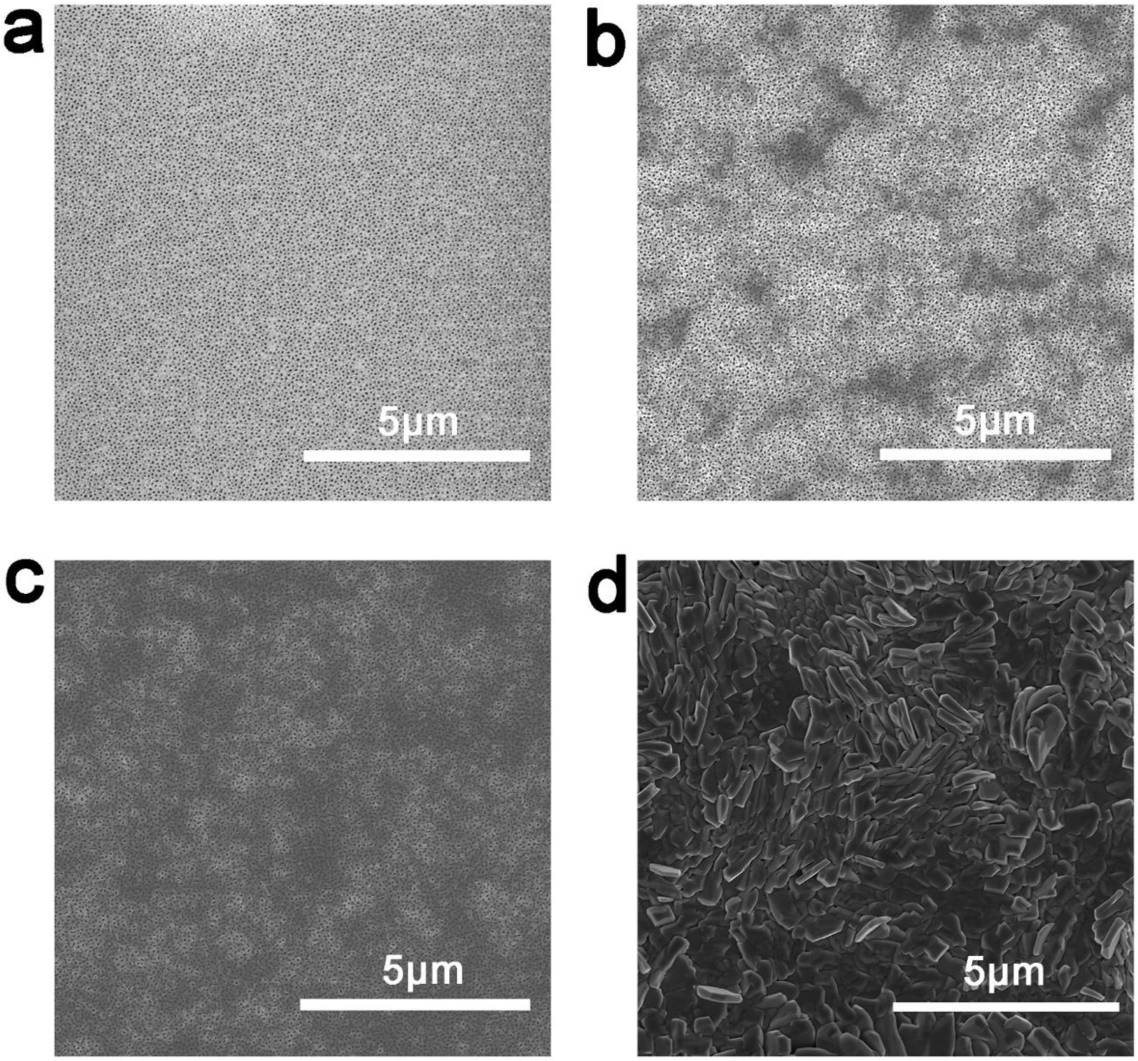

Figure 5.9 SEM images of different volume of $MoS_2$ growing on 3DG

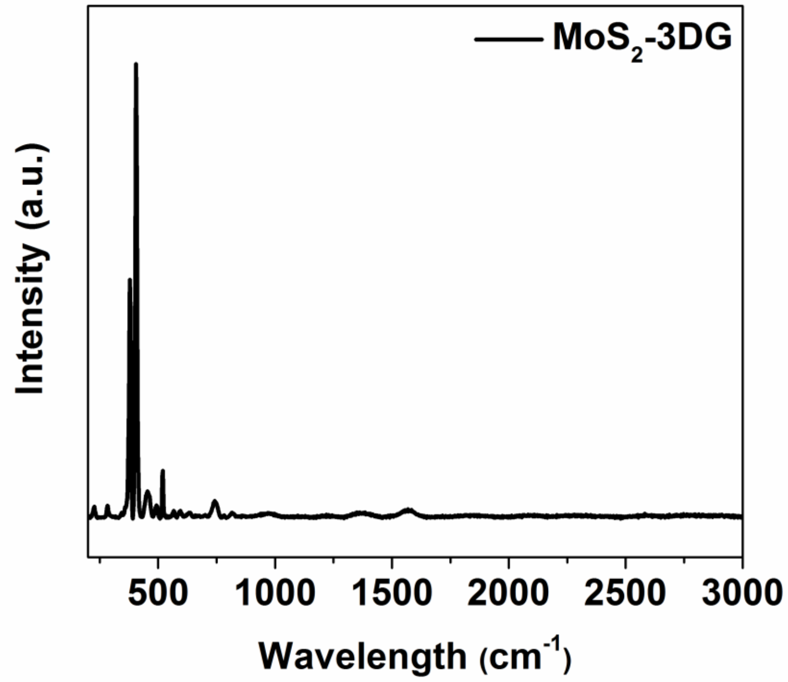

Figure 5.10 Raman spectra of thick $MoS_2$ decorated on 3DG, corresponding to the sample in Fig. 5.9d.

### Electrochemical performance of the $MoS_2$-3DG films

The electrochemical performance of the $MoS_2$-3DG film as anode in LIBs was evaluated by transferring of $MoS_2$-3DG thin film to the battery cells directly. Thus, it avoided the step to mix with extra materials such as polymer binders or carbon black, providing a simple method for the potential LIB fabrications white retaining the intrinsic electric properties of 3DG.

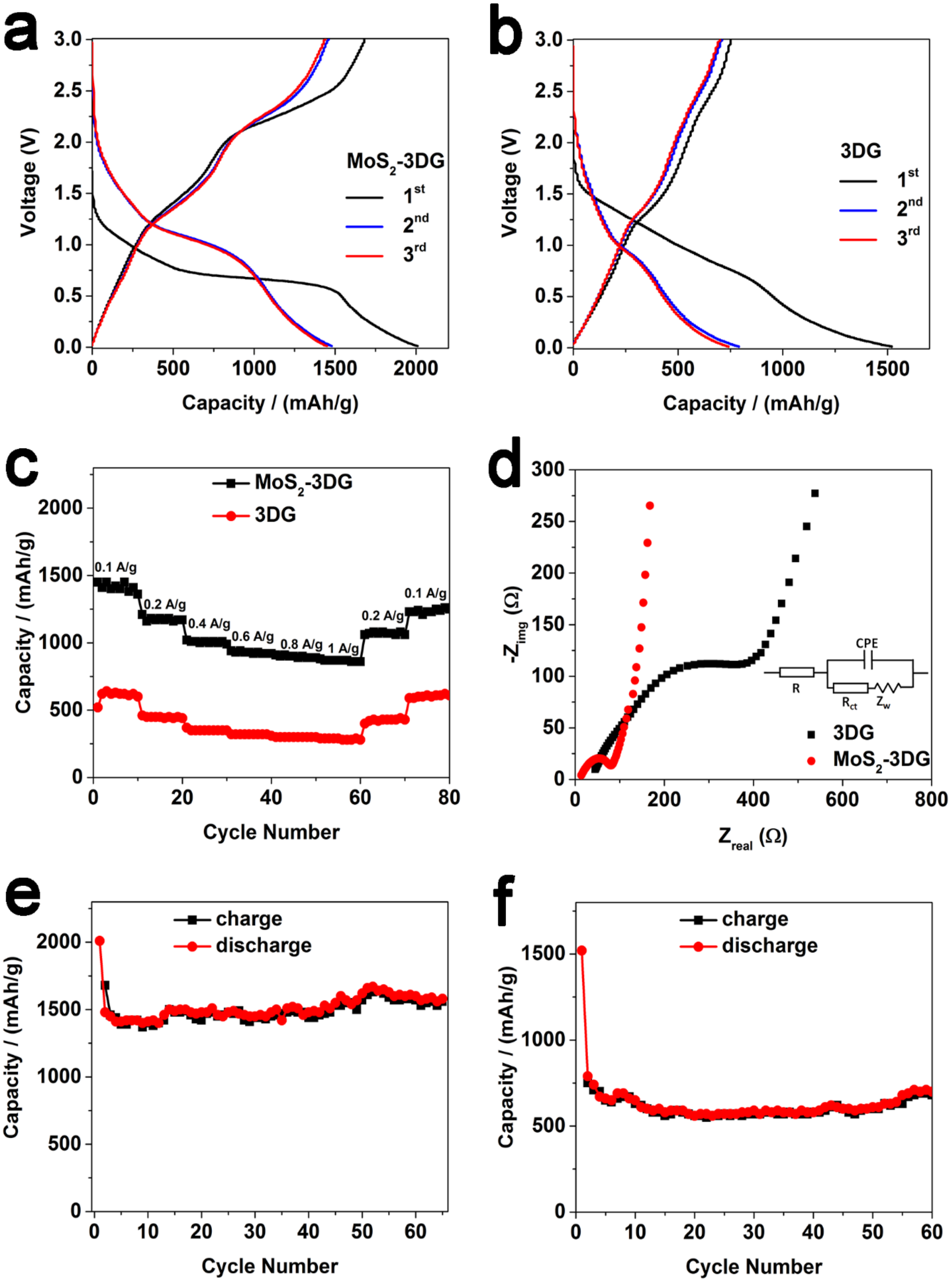
a
MoS$_2$-3DG
1st
2nd
3rd
Voltage (V)
Capacity / (mAh/g)
b
3DG
1st
2nd
3rd
Voltage (V)
Capacity / (mAh/g)
c
MoS$_2$-3DG
3DG
0.1 A/g
0.2 A/g
0.4 A/g
0.6 A/g
0.8 A/g
1 A/g
0.2 A/g
0.1 A/g
Capacity / (mAh/g)
Cycle Number
d
-Z$_{img}$ (Ω)
Z$_{real}$ (Ω)
CPE
R
R$_{ct}$
Z$_w$
3DG
MoS$_2$-3DG
e
charge
discharge
Capacity / (mAh/g)
Cycle Number
f
charge
discharge
Capacity / (mAh/g)
Cycle Number

Figure 5.11 Galvanostatic charge and discharge curves of (a) $MoS_2$-3DG and (b) 3DG at a current density of 0.1A $g^{-1}$ measured in a voltage range from 0.02 to 3.0 V; (c) rate performance of $MoS_2$-3DG and 3DG; (d) Nyquist plots of $MoS_2$-3DG and 3DG; cycling performances of (e) $MoS_2$-3DG and (f) 3DG.

Fig. 5.11a shows the first three cycle of galvanostatic charge and discharge for $MoS_2$-3DG at current density of 0.1 A $g^{-1}$ in the voltage range from 0.02 to 3.0 V. In the first discharge process, a conspicuous plateau at 1.06 V was observed, which can be attributed to the intercalation of Li ions into $MoS_2$ to form $Li_xMoS_2$ and subsequently reduced to Mo and $Li_2S$[170]. This behavior became much apparent in the second and the third discharge curves. The plateau at ca. 0.65 V is ascribed to the formation of the solid electrolyte interphase (SEI) film from the electrolyte decomposition[135], which disappeared in the second and the third discharge curves. The capacity lower than 0.5 V could account for the Li-ions intercalation on 3D graphene layers. In the anodic scanning, the Li-ions were continually released from the $MoS_2$-3DG matrix, and Mo was partially oxidized to form $MoS_2$. Thus, the slopes from 1.24 to 1.90 V can be observed. The subsequent cycles demonstrated the reversible and stable reaction to convert between $MoS_2$ and Mo/$Li_2S$.

As the initial discharge and charge capacities were 2010 and 1680 mAh $g^{-1}$, respectively, with an initial Coulombic efficiency of 84%, which is much higher than that of other $MoS_2$/G based anodes (Tab. 5.1). The second discharge and charge capacities are 1480 and 1460 mAh $g^{-1}$, respectively, with a loss capacity due to the SEI formation. Nevertheless, the Coulombic efficiencies reached to and kept above 99% from the second cycles, illustrating the excellent stability and cycling performance, which could be attributed to the stable chemical structures arising from the robust 3D framework, and the uniform distribution of $MoS_2$.

In contrast, 3DG based anode exhibited poorer performance than $MoS_2$-3DG, as seen in Fig. 5.11b. The initial discharge and charge capacities are 1520 and 751 mAh $g^{-1}$, respectively, with a low Coulombic efficiency of 49%. The irreversible capacity at ca. 0.7 V in the first discharge cycle could be attributed to the formation of the SEI film. It disappeared since the second cycle with discharge/charge capacities of 790/710 mAh $g^{-1}$, respectively. There was no apparent plateau in discharge/charge curve, suggesting the disordered stacking structure of graphene in the 3D framework.

To test the rate capability, the cells based on $MoS_2$-3DG anodes and 3DG anodes were both measured from 0.1 to 1 A $g^{-1}$ in the voltage range of 0.01~3 V. As seen in Fig. 5.11c, the $MoS_2$-3DG anode showed a superb rate capacity with the average discharge capacities of 1420, 1180, 1000, 1007, 910 and 870 mAh $g^{-1}$ as the current density increased from 0.1, 0.2, 0.4, 0.6, 0.8, and 1 A $g^{-1}$, respectively. After discharging/charging at 1 A $g^{-1}$, $MoS_2$-3DG anodes bounced back to 1070 mAh $g^{-1}$ at 0.2 A $g^{-1}$ and maintained a reversible capacity as high as 1250 mAh $g^{-1}$ when the current density returned to 0.1 A $g^{-1}$. The 3DG based anode also demonstrated a great rate capacity with a good recovery of capacity as the current density decreased to 0.1 mA $g^{-1}$. It is proved that the 3DG could be served as a stable and conductive matrix.

The Electrochemical impedance spectroscopy (EIS) was carried out to study the electrochemical behavior of $MoS_2$-3DG as shown in Fig. 5.11d. The semicircle at the high-frequency represents the interface resistance between electrode and electrolyte (Rct and

CPE) and the diagonal slope at the low-frequency reveals the Li-ion diffusion in the active materials of the electrode, known as the Warburg impedance (Zw)[171]. Hence, $MoS_2$-3DG shows a lower resistance and higher ion diffusion compared to 3DG, suggesting that $MoS_2$-3DG can enhance the ability of Li-ions diffusion by decorating $MoS_2$ on the 3DG framework.

The cycling performance of $MoS_2$-3DG was further investigated by discharging/charging the cells for 60 cycles at 0.1 A $g^{-1}$ in the voltage range of 0.02~3.0 V. As seen in Fig. 5.11e, the $MoS_2$-3DG based anodes exhibited a stable capacity after the initial cycles, representing a complete transport and contact of electrolytes to the $MoS_2$-3DG anode materials during the cycling. The slightly ascending of capacities can be observed after several cycles due to the permanent expanding of $MoS_2$ interlayers by Li intercalation. The excellent cycling performance of the 3DG based anode can also be observed in Fig. 5.11f, which shows that 3DG plays critical roles in structure stability.

Table 1 Comparison of electrochemical properties of $MoS_2$ and $MoS_2$/carbon nanomaterial hybrids

| **Electrode description** | **1st Specific capacity** | **1st Coulombic efficiency** | **Cycling stability** | **Rate performance** |
|---|---|---|---|---|
| $MoS_2$-3DG (This work) | 2010 mAh/g at 100 mA/g | 85.6% | 1650 mAh/g after 54 cycles at 100 mA/g | 1180, 1000, 1007, 910 and 870 mAh/g at 200, 400, 600, 800 and 1000 mA/g |
| Honeycomb-like $MoS_2$ on | 1397 mAh/g at 100 mA/g | 82.9% | 1100 mAh/g after 60 cycles at 200 mA/g | 1172, 1095,1007, 966 and 800 mAh/g at |

| | | | | |
|---|---|---|---|---|
| 3D graphene foam [166] | | | | 200, 500, 1000, 2000 and 5000 mA/g |
| $MoS_2$ /3DG network composite[46] | 1222mAh/g at 100 mA/g | 83.5% | 877 mAh/g after 50 cycles at 100mA/g | 849, 782, 692 and 597 mAh/g at 100, 200, 500, and 1000 mA/g |
| NDG/$MoS_2$[172] | 1000 mAh/g at 100mA/g | 75% | ~1040mAh/g after 1000 cycles at 100mA/g | 1050, 970, 810, 700, 630, and 460 mAh/g at 100, 200, 500, 1000, 2000, and 5000 mA/g |
| $MoS_2$/G composite[168] | 1160 mAh/g at 100mA/g | 77.2% | 1077 mAh/g at 100 mA/g after 150 cycles | 1035, 1012, 986, and 890 mAh/g at 200, 300, 500, and 1000 mA/g |
| $MoS_2$/G (1:2)[68] | 1571 mAh/g at 100mA/g | 65.6% | 1187 mAh/g after 100 cycles at 100mA/g | ~900 mAh/g at 1000 mA/g |
| $MoS_2$/graphene nanosheet composite[165] | 2200 mAh/g at 100 mA/g | 59% | 1290 mAh/g after 50 cycles at 100 mA/g | 1040 mAh/g at 1000 mA/g |
| $MoS_2$ nanospheres/alkylcarboxyl functional[173] | 1464mAh/g at 100mA/g | 74% | 1064 mAh/g after 100 cycles at 100mA/g | 1173, 1050, 1004, 980 and 910 mAh/g at 100, 200, 400, 800 and 1600 mA/g |
| CNT–$MoS_2$ composite[174] | 1715 mAh/g at 200 mA/g | 76.10% | 1456 mAh/g after 50 cycles at 200 mA/g | 1431,1367, 1302 and 1224 mAh/g at 400, 600, 800 and 1000 mA/g |

| | | | | |
|---|---|---|---|---|
| MoSx/CNT[169] | 1549 mAh/g at 50 mA/g | 74.80% | ≥1000 mA/g after 40 cycles at 50 mA/g | 1119, 904, 659, 358 and 197 mAh/g at 50, 200, 500 and 1000 mA/g |
| $MoS_2$ nanoplates[163] | 1062mAh/g at 1060 mA/g | 87% | 907 mAh/g after 50 cycles at 1060/g | 790 and 700 mAh/g at 31.8 and 53.1A/g |
| Graphene sheets[103] | 2035 mAh/g at 100 mA/g | 62.1% | 848 mAh/g after 40 cycles at 100 mA/g | 936 , 718 and 445 mAh/g at 300, 500 and 1000 mA/g |

The electrochemical performance of the thick $MoS_2$ decorated 3DG (thick-$MoS_2$-3DG) was also studied for comparison. As seen in Fig. 5.12a, thick-$MoS_2$-3DG showed a similar lithium intercalation and deintercalation process regarding the reversible convert between $MoS_2$ and Mo/$Li_2S$ as $MoS_2$-3DG samples. However, the initial discharge and charge capacities of the thick-$MoS_2$-3DG are 1600 and 890 mAh $g^{-1}$, respectively with the initial Coulombic efficiency of 56%, which are much lower than that of $MoS_2$-3DG due to the poor conductivity of $MoS_2$.

The rate and cycling performance of the thick-$MoS_2$-3DG are demonstrated in Figs. 12b and c. Consider the 3DG and the $MoS_2$-3DG based anodes, all three electrodes exhibit high rate capabilities and cycling stabilities, indicating the incorporation of 3DG can offer the fast electron transport and the sufficient Li-ion diffusion and enhance the electrodes' stabilities during the lithiation/delithiation process.

The EIS in Fig. 5.12d shows a low interface resistance and the high Li ion diffusion, consistent with EIS of $MoS_2$-3DG based anodes. Thus, $MoS_2$ decorated 3DG can contribute the high lithium storage in layered $MoS_2$ and the highly conductive in ordered 3DG structure.

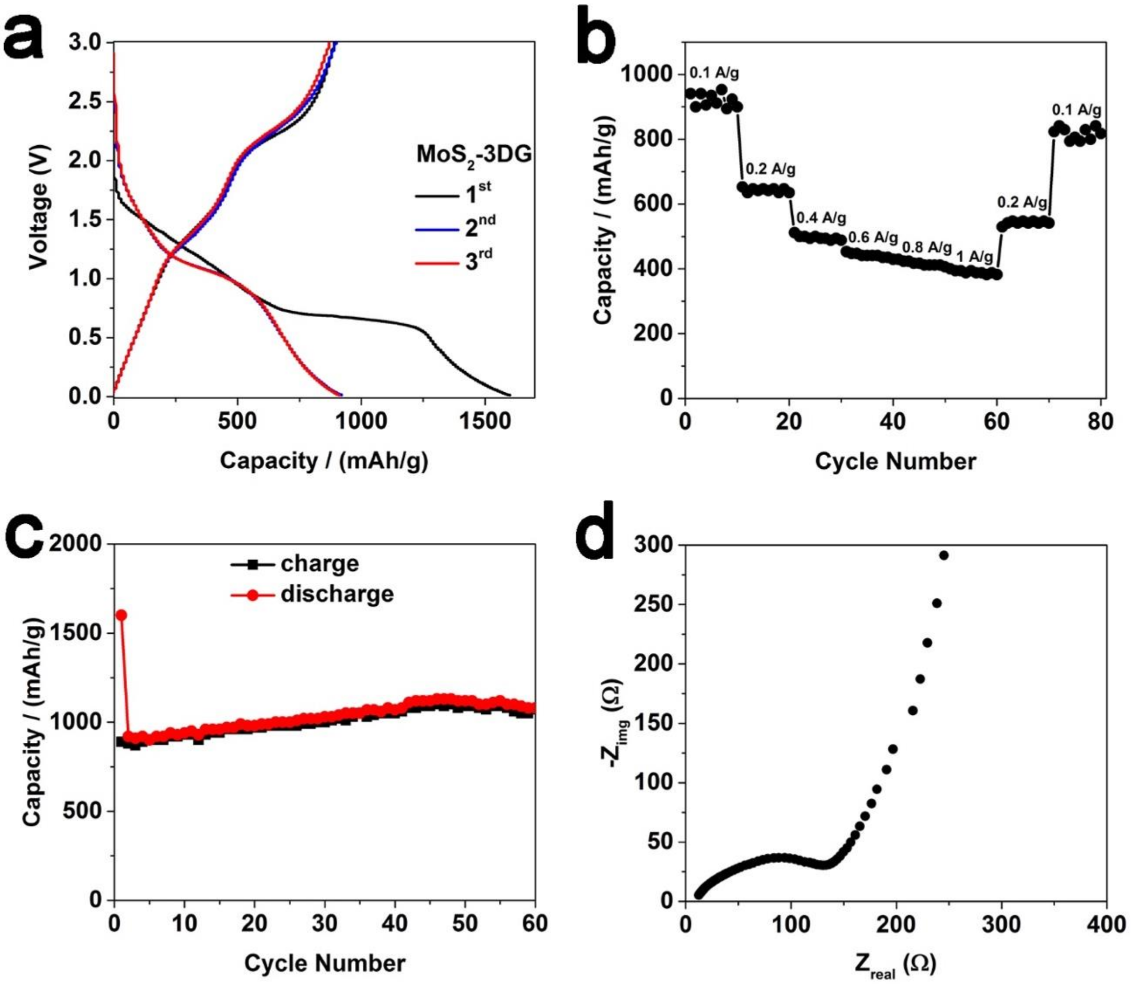

Figure 5.12 Electrochemical performance of thick-$MoS_2$ decorated 3DG: (a) Galvanostatic charge and discharge curves at a current density of 0.1A $g^{-1}$ measured in a voltage range from 0.02 to 3.0 V; (b) rate performance; (c) cycling performances; (d) Nyquist plots.

## 5.4 Conclusions

In summary, 3D ordered graphene materials decorated with $MoS_2$ were fabricated via a CVD method. The resultant $MoS_2$-3DG hybrid illustrates a new heterostructure with $MoS_2$ nanosheets anchoring on a 3D graphene framework. The $MoS_2$-3DG based anodes exhibited outstanding performances with a high reversible capacity, high rate capability, and long cycle life, which are much higher than those of other $MoS_2$-graphene composites (Table 5.1). The demonstrated controllable synthesis of $MoS_2$ on 3DG offers an opportunity to the rational design for other 3D graphene hybrids with tunable electrochemical properties to enhance the performance for Li-ion storage and many other applications.

# Bibliography

1. Ellingsen, L.A.W. *et al.* Nanotechnology for environmentally sustainable electromobility (vol 11, pg 1039, 2016). *Nature Nanotechnology* **12**, 90-90 (2017).

2. Dai, L.M., Chang, D.W., Baek, J.B. & Lu, W. Carbon nanomaterials for advanced energy conversion and storage. *Small* **8**, 1130-1166 (2012).

3. Geim, A.K. & Novoselov, K.S. The rise of graphene. *Nature Materials* **6**, 183-191 (2007).

4. Novoselov, K.S. *et al.* Two-dimensional gas of massless Dirac fermions in graphene. *Nature* **438**, 197-200 (2005).

5. Novoselov, K.S. *et al*. Electric field effect in atomically thin carbon films. *Science* **306**, 666-669 (2004).

6. Lee, C., Wei, X., Kysar, J.W. & Hone, J. Measurement of the elastic properties and intrinsic strength of monolayer graphene. *Science* **321**, 385-388 (2008).

7. Nair, R.R. *et al*. Fine structure constant defines visual transparency of graphene. *Science* **320**, 1308-1308 (2008).

8. Sutter, P.W., Flege, J.I. & Sutter, E.A. Epitaxial graphene on ruthenium. *Nature Materials* **7**, 406-411 (2008).

9. Eizenberg, M. & Blakely, J.M. Carbon monolayer phase condensation on Ni(111). *Surface Science* **82**, 228-236 (1979).

10. Reina, A. *et al*. Large area, few-layer graphene films on arbitrary substrates by chemical vapor deposition. *Nano Letters* **9**, 30-35 (2008).

11. Lotya, M. *et al*. Liquid phase production of graphene by exfoliation of graphite in surfactant/water solutions. *Journal of the American Chemical Society* **131**, 3611-3620 (2009).

12. Stankovich, S. *et al*. Synthesis of graphene-based nanosheets via chemical reduction of exfoliated graphite oxide. *Carbon* **45**, 1558-1565 (2007).

13. Dai, L.M. Functionalization of graphene for efficient energy conversion and storage. *Accounts of Chemical Research* **46**, 31-42 (2013).

14. Duan, J.J., Chen, S., Jaroniec, M. & Qiao, S.Z. Heteroatom-doped graphene-based materials for energy-relevant electrocatalytic processes. *ACS Catalysis* **5**, 5207-5234 (2015).

15. Georgakilas, V. *et al*. Functionalization of graphene: covalent and non-covalent approaches, derivatives and applications. *Chemical Reviews* **112**, 6156-6214 (2012).

16. Cao, X.H., Yin, Z.Y. & Zhang, H. Three-dimensional graphene materials: preparation, structures and application in supercapacitors. *Energy & Environmental Science* **7**, 1850-1865 (2014).

17. Li, C. & Shi, G.Q. Three-dimensional graphene architectures. *Nanoscale* **4**, 5549-5563 (2012).

18. Hass, J., de Heer, W.A. & Conrad, E.H. The growth and morphology of epitaxial multilayer graphene. *Journal of Physics-Condensed Matter* **20** (2008).

19. Kim, K.S. *et al*. Large-scale pattern growth of graphene films for stretchable transparent electrodes. *Nature* **457**, 706-710 (2009).

20. Novoselov, K.S. *et al*. Two-dimensional atomic crystals. *Proceedings of the National Academy of Sciences of the United States of America* **102**, 10451-10453 (2005).

21. Park, S. & Ruoff, R.S. Chemical methods for the production of graphenes. *Nature Nanotechnology* **4**, 217-224 (2009).

22. Xu, Y.X., Sheng, K.X., Li, C. & Shi, G.Q. Self-assembled graphene hydrogel via a one-step hydrothermal process. *ACS Nano* **4**, 4324-4330 (2010).

23. Chen, Z.P. *et al*. Three-dimensional flexible and conductive interconnected graphene networks grown by chemical vapour deposition. *Nature Materials* **10**, 424-428 (2011).

24. Hummers, W.S. & Offeman, R.E. Preparation of graphitic oxide. *Journal of the American Chemical Society* **80**, 1339-1339 (1958).

25. Pei, S.F., Zhao, J.P., Du, J.H., Ren, W.C. & Cheng, H.M. Direct reduction of graphene oxide films into highly conductive and flexible graphene films by hydrohalic acids. *Carbon* **48**, 4466-4474 (2010).

26. Chen, W.F. & Yan, L.F. In situ self-assembly of mild chemical reduction graphene for three-dimensional architectures. *Nanoscale* **3**, 3132-3137 (2011).

27. Qiu, B.C., Xing, M.Y. & Zhang, J.L. Mesoporous $TiO_2$ nanocrystals grown in situ on graphene aerogels for high photocatalysis and lithium-ion batteries. *Journal of the American Chemical Society* **136**, 5852-5855 (2014).

28. Li, L. *et al*. Monolithic $Fe_2O_3$/graphene hybrid for highly efficient lithium storage and arsenic removal. *Carbon* **67**, 500-507 (2014).

29. Wang, Z.J., Zhou, X.Z., Zhang, J., Boey, F. & Zhang, H. Direct electrochemical reduction of single-layer graphene oxide and subsequent functionalization with glucose oxidase. *Journal of Physical Chemistry C* **113**, 14071-14075 (2009).

30. Zhou, M. *et al*. Controlled synthesis of large-area and patterned electrochemically reduced graphene oxide films. *Chemistry-A European Journal* **15**, 6116-6120 (2009).

31. Sheng, K.X., Sun, Y.Q., Li, C., Yuan, W.J. & Shi, G.Q. Ultrahigh-rate supercapacitors based on eletrochemically reduced graphene oxide for ac line-filtering. *Scientific Reports* **2** 247 (2012).

32. Li, X. *et al*. Large-area synthesis of high-quality and uniform graphene films on copper foils. *Science* **324**, 1312-1314 (2009).

33. Reina, A. *et al*. Large area, few-layer graphene films on arbitrary substrates by chemical vapor deposition. *Nano Letters* **9**, 30-35 (2009).

34. Kwon, S.Y. *et al*. Growth of semiconducting graphene on palladium. *Nano Letters* **9**, 3985-3990 (2009).

35. Coraux, J., N'Diaye, A.T., Busse, C. & Michely, T. Structural coherency of graphene on Ir (111). *Nano Letters* **8**, 565-570 (2008).

36. Hamilton, J.C. & Blakely, J.M. Carbon segregation to single-crystal surfaces of Pt, Pd and Co. *Surface Science* **91**, 199-217 (1980).

37. Mattevi, C., Kim, H. & Chhowalla, M. A review of chemical vapour deposition of graphene on copper. *Journal of Materials Chemistry* **21**, 3324-3334 (2011).

38. Fang, W.J., Hsu, A.L., Song, Y. & Kong, J. A review of large-area bilayer graphene synthesis by chemical vapor deposition. *Nanoscale* **7**, 20335-20351 (2015).

39. Bae, S. *et al*. Roll-to-roll production of 30-inch graphene films for transparent electrodes. *Nature Nanotechnology* **5**, 574-578 (2010).

40. Chen, J.Y. *et al*. Oxygen-aided synthesis of polycrystalline graphene on silicon dioxide substrates. *Journal of the American Chemical Society* **133**, 17548-17551 (2011).

41. Fanton, M.A. *et al*. Characterization of graphene films and transistors grown on sapphire by metal-free chemical vapor deposition. *ACS Nano* **5**, 8062-8069 (2011).

42. Rummeli, M.H. *et al*. Direct low-temperature nanographene CVD synthesis over a dielectric insulator. *ACS Nano* **4**, 4206-4210 (2010).

43. Ning, G.Q. *et al*. Gram-scale synthesis of nanomesh graphene with high surface area and its application in supercapacitor electrodes. *Chemical Communications* **47**, 5976-5978 (2011).

44. Yoon, J.C., Lee, J.S., Kim, S.I., Kim, K.H. & Jang, J.H. Three-dimensional graphene nano-networks with high quality and mass production capability via precursor-assisted chemical vapor deposition. *Scientific Reports* **3** 1788 (2013).

45. Yang, C.Y. *et al*. Direct PECVD growth of vertically erected graphene walls on dielectric substrates as excellent multifunctional electrodes. *Journal of Materials Chemistry A* **1**, 770-775 (2013).

46. Cao, X.H. *et al*. Preparation of $MoS_2$-coated three-dimensional graphene networks for high-performance anode material in lithium-ion batteries. *Small* **9**, 3433-3438 (2013).

47. Duan, J.J., Chen, S., Chambers, B.A., Andersson, G.G. & Qiao, S.Z. 3D $WS_2$ nanolayers@heteroatom-doped graphene films as hydrogen evolution catalyst electrodes. *Advanced Materials* **27**, 4234-4241 (2015).

48. Haigh, S.J. *et al*. Cross-sectional imaging of individual layers and buried interfaces of graphene-based heterostructures and superlattices. *Nature Materials* **11**, 764-767 (2012).

49. Zhu, Y. *et al*. A seamless three-dimensional carbon nanotube graphene hybrid material. *Nature Communications* **3** 1225 (2012).

50. Fan, Z. *et al*. A Three-dimensional carbon nanotube/graphene sandwich and its application as electrode in supercapacitors. *Advanced Materials* **22**, 3723-3728 (2010).

51. Yu, D.S. & Dai, L.M. Self-assembled graphene/carbon nanotube hybrid films for supercapacitors. *Journal of Physical Chemistry Letters* **1**, 467-470 (2010).

52. Du, F. *et al*. Preparation of tunable 3D pillared carbon nanotube-graphene networks for high-performance capacitance. *Chemistry of Materials* **23**, 4810-4816 (2011).

53. Yu, A.P. *et al*. Free-standing layer-by-layer hybrid thin film of graphene-$MnO_2$ nanotube as anode for lithium ion batteries. *Journal of Physical Chemistry Letters* **2**, 1855-1860 (2011).

54. Yu, D.S., Park, K., Durstock, M. & Dai, L.M. Fullerene-grafted graphene for efficient bulk heterojunction polymer photovoltaic devices. *Journal of Physical Chemistry Letters* **2**, 1113-1118 (2011).

55. Chen, W.F., Li, S.R., Chen, C.H. & Yan, L.F. Self-assembly and embedding of nanoparticles by in situ reduced graphene for preparation of a 3D graphene/nanoparticle aerogel. *Advanced Materials* **23**, 5679-5683 (2011).

56. Guo, C.X. *et al*. Layered Graphene/quantum dots for photovoltaic devices. *Angewandte Chemie-International Edition* **49**, 3014-3017 (2010).

57. Chen, Q. *et al*. Graphene quantum dots-three-dimensional graphene composites for high-performance supercapacitors. *Physical Chemistry Chemical Physics* **16**, 19307-19313 (2014).

58. Wu, Z.S. *et al*. 3D Nitrogen-doped graphene aerogel-supported $Fe_3O_4$ nanoparticles as efficient eletrocatalysts for the oxygen reduction reaction. *Journal of the American Chemical Society* **134**, 9082-9085 (2012).

59. Xue, Y. *et al*. Rationally designed graphene-nanotube 3D architectures with a seamless nodal junction for efficient energy conversion and storage. *Science Advances* **1,** e1400198 (2015).

60. Xu, C., Wang, X. & Zhu, J.W. Graphene-metal particle nanocomposites. *Journal of Physical Chemistry C* **112**, 19841-19845 (2008).

61. Parvez, K. *et al*. Nitrogen-doped graphene and its iron-based composite as efficient electrocatalysts for oxygen reduction reaction. *ACS Nano* **6**, 9541-9550 (2012).

62. Peng, H.L. *et al*. High performance Fe- and N- doped carbon catalyst with graphene structure for oxygen reduction. *Scientific Reports* **3** (2013).

63. Yu, D.L. & He, X.Q. 3D cobalt-embedded nitrogen-doped graphene xerogel as an efficient electrocatalyst for oxygen reduction reaction in an alkaline medium. *Journal of Applied Electrochemistry* **47**, 13-23 (2017).

64. Yan, J. *et al*. Fast and reversible surface redox reaction of graphene-$MnO_2$ composites as supercapacitor electrodes. *Carbon* **48**, 3825-3833 (2010).

65. Chang, Y.H. *et al*. Synthesis of 3D nitrogen-doped graphene/$Fe_3O_4$ by a metal ion induced self-assembly process for high-performance Li-ion batteries. *Journal of Materials Chemistry A* **1**, 14658-14665 (2013).

66. Luo, J.S. *et al*. Three-dimensional graphene foam supported $Fe_3O_4$ lithium battery anodes with long cycle life and high rate capability. *Nano Letters* **13**, 6136-6143 (2013).

67. Dong, X.C. *et al*. 3D graphene-cobalt oxide electrode for high-performance supercapacitor and enzymeless glucose detection. *ACS Nano* **6**, 3206-3213 (2012).

68. Chang, K. & Chen, W.X. L-cysteine-assisted synthesis of layered $MoS_2$/graphene composites with excellent electrochemical performances for lithium ion batteries. *ACS Nano* **5**, 4720-4728 (2011).

69. Hou, Y. *et al*. A 3D hybrid of layered $MoS_2$/nitrogen-doped graphene nanosheet aerogels: an effective catalyst for hydrogen evolution in microbial electrolysis cells. *Journal of Materials Chemistry A* **2**, 13795-13800 (2014).

70. Lim, H., Yoon, S.I., Kim, G., Jang, A.R. & Shin, H.S. Stacking of two-dimensional materials in lateral and vertical directions. *Chemistry of Materials* **26**, 4891-4903 (2014).

71. Huang, X., Zeng, Z.Y. & Zhang, H. Metal dichalcogenide nanosheets: preparation, properties and applications. *Chemical Society Reviews* **42**, 1934-1946 (2013).

72. Du, G.D. *et al*. Superior stability and high capacity of restacked molybdenum disulfide as anode material for lithium ion batteries. *Chemical Communications* **46**, 1106-1108 (2010).

73. Li, Y.G. *et al*. $MoS_2$ nanoparticles grown on graphene: an advanced catalyst for the hydrogen evolution reaction. *Journal of the American Chemical Society* **133**, 7296-7299 (2011).

74. Zhang, J.T., Xia, Z.H., & Dai, L.M. Carbon-based electrocatalysts for advanced energy conversion and storage. *Science Advances* **1,** e1500564 (2015).

75. Denis, P.A., Faccio, R. & Mombru, A.W. Is it possible to dope single-walled carbon nanotubes and graphene with sulfur? *Chemphyschem* **10**, 715-722 (2009).

76. Xue, Y.H. *et al*. Three-dimensional B,N-doped graphene foam as a metal-free catalyst for oxygen reduction reaction. *Physical Chemistry Chemical Physics* **15**, 12220-12226 (2013).

77. Xu, J.T. *et al*. High-performance sodium ion batteries based on a 3D anode from nitrogen-doped graphene foams. *Advanced Materials* **27**, 2042-2048 (2015).

78. Yu, M., Ma, Y.X., Liu, J.H. & Li, S.M. Polyaniline nanocone arrays synthesized on three-dimensional graphene network by electrodeposition for supercapacitor electrodes. *Carbon* **87**, 98-105 (2015).

79. Xu, Y.X., Wu, Q.O., Sun, Y.Q., Bai, H. & Shi, G.Q. Three-dimensional self-assembly of graphene oxide and DNA into multifunctional hydrogels. *ACS Nano* **4**, 7358-7362 (2010).

80. Winter, M. & Brodd, R.J. What are batteries, fuel cells, and supercapacitors? *Chemical Reviews* **104**, 4245-4269 (2004).

81. Simon, P. & Gogotsi, Y. Materials for electrochemical capacitors. *Nature Materials* **7**, 845-854 (2008).

82. Arico, A.S., Bruce, P., Scrosati, B., Tarascon, J.M. & Van Schalkwijk, W. Nanostructured materials for advanced energy conversion and storage devices. *Nature Materials* **4**, 366-377 (2005).

83. Cao, X.H. *et al*. Preparation of novel 3D graphene networks for supercapacitor applications. *Small* **7**, 3163-3168 (2011).

84. Shui, J.L., Wang, M., Du, F., & Dai, L.M. N-doped carbon nanomaterials are durable catalysts for oxygen reduction reaction in acidic fuel cells. *Science Advances* **1,** e1400129 (2015).

85. Geng, D.S., Hu, Y.H., Li, Y.L., Li, R.Y. & Sun, X.L. One-pot solvothermal synthesis of doped graphene with the designed nitrogen type used as a Pt support for fuel cells. *Electrochemistry Communications* **22**, 65-68 (2012).

86. Guo, S.J., Dong, S.J. & Wang, E.K. Three-dimensional Pt-on-Pd bimetallic nanodendrites supported on graphene nanosheet: facile synthesis and used as an advanced nanoelectrocatalyst for methanol oxidation. *ACS Nano* **4**, 547-555 (2010).

87. Liang, Y.Y. *et al*. Covalent hybrid of spinel manganese-cobalt oxide and graphene as advanced oxygen reduction electrocatalysts. *Journal of the American Chemical Society* **134**, 3517-3523 (2012).

88. Liang, Y.Y. *et al*. $Co_3O_4$ nanocrystals on graphene as a synergistic catalyst for oxygen reduction reaction. *Nature Materials* **10**, 780-786 (2011).

89. Gong, K.P., Du F., Xia, Z.H., Durstock, M., & Dai, L.M. Nitrogen-doped carbon nanotube arrays with high electrocatalytic activity for oxygen reduction. *Science* **323,** 760-764 (2009).

90. Qu, L.T., Liu, Y., Baek, J.B. & Dai, L.M. Nitrogen-doped graphene as efficient metal-free electrocatalyst for oxygen reduction in fuel cells. *ACS Nano* **4**, 1321-1326 (2010).

91. Kotz, R. & Carlen, M. Principles and applications of electrochemical capacitors. *Electrochimica Acta* **45**, 2483-2498 (2000).

92. Chen, T. & Dai, L.M. Flexible supercapacitors based on carbon nanomaterials. *Journal of Materials Chemistry A* **2**, 10756-10775 (2014).

93. Xu, Y.X. *et al*. Flexible solid-state supercapacitors based on three-dimensional graphene hydrogel films. *ACS Nano* **7**, 4042-4049 (2013).

94. Wu, Z.S. *et al*. Three-dimensional nitrogen and boron co-doped graphene for high-performance all-solid-state supercapacitors. *Advanced Materials* **24**, 5130-5135 (2012).

95. Chen, S., Zhu, J.W., Wu, X.D., Han, Q.F. & Wang, X. Graphene oxide-$MnO_2$ nanocomposites for supercapacitors. *ACS Nano* **4**, 2822-2830 (2010).

96. He, Y.M. *et al*. Freestanding three-dimensional graphene/$MnO_2$ composite networks as ultra light and flexible supercapacitor electrodes. *ACS Nano* **7**, 174-182 (2013).

97. Wu, Q., Xu, Y.X., Yao, Z.Y., Liu, A.R. & Shi, G.Q. Supercapacitors based on flexible graphene/polyaniline nanofiber composite films. *ACS Nano* **4**, 1963-1970 (2010).

98. Dong, X.C. *et al*. Supercapacitor electrode based on three-dimensional graphene-polyaniline hybrid. *Materials Chemistry and Physics* **134**, 576-580 (2012).

99. Lin, J. *et al*. 3-dimensional graphene carbon nanotube carpet-based microsupercapacitors with high electrochemical performance. *Nano Letters* **13**, 72-78 (2013).

100. Tarascon, J.M. & Armand, M. Issues and challenges facing rechargeable lithium batteries. *Nature* **414**, 359-367 (2001).

101. Bruce, P.G., Scrosati, B. & Tarascon, J.M. Nanomaterials for rechargeable lithium batteries. *Angewandte Chemie-International Edition* **47**, 2930-2946 (2008).

102. Dahn, J.R., Zheng, T., Liu, Y.H. & Xue, J.S. Mechanisms for lithium insertion in carbonaceous materials. *Science* **270**, 590-593 (1995).

103. Lian, P.C. *et al*. Large reversible capacity of high quality graphene sheets as an anode material for lithium-ion batteries. *Electrochimica Acta* **55**, 3909-3914 (2010).

104. Wang, H.B. *et al*. Nitrogen-doped graphene nanosheets with excellent lithium storage properties. *Journal of Materials Chemistry* **21**, 5430-5434 (2011).

105. Lee, J.K., Smith, K.B., Hayner, C.M. & Kung, H.H. Silicon nanoparticles-graphene paper composites for Li ion battery anodes. *Chemical Communications* **46**, 2025-2027 (2010).

106. Xue, D.J. *et al*. Improving the electrode performance of Ge through Ge@C core-shell nanoparticles and graphene networks. *Journal of the American Chemical Society* **134**, 2512-2515 (2012).

107. Wang, G.X. *et al*. Sn/graphene nanocomposite with 3D architecture for enhanced reversible lithium storage in lithium ion batteries. *Journal of Materials Chemistry* **19**, 8378-8384 (2009).

108. Wang, R.H., Xu, C.H., Sun, J., Gao, L. & Yao, H.L. Solvothermal-induced 3D macroscopic $SnO_2$/nitrogen-doped graphene aerogels for high capacity and long-life lithium storage. *ACS Applied Materials & Interfaces* **6**, 3427-3436 (2014).

109. Zhang, Y. *et al*. Nitrogen-doped graphene ribbon assembled core-sheath MnO@graphene scrolls as hierarchically ordered 3D porous electrodes for fast and durable lithium storage. *Advanced Functional Materials* **26**, 7754-7765 (2016).

110. Wei, W. *et al*. 3D graphene foams cross-linked with pre-encapsulated $Fe_3O_4$ Nanospheres for Enhanced Lithium Storage. *Advanced Materials* **25**, 2909-2914 (2013).

111. Zhao, Y. *et al*. Functional graphene nanomesh foam. *Energy & Environmental Science* **7**, 1913-1918 (2014).

112. Jeong, H.M. *et al*. Nitrogen-doped graphene for high-performance ultracapacitors and the importance of nitrogen-doped sites at basal planes. *Nano Letters* **11**, 2472-2477 (2011).

113. Yang, Z. *et al*. Sulfur-doped graphene as an efficient metal-free cathode catalyst for oxygen reduction. *ACS Nano* **6**, 205-211 (2012).

114. Geng, D.S. *et al*. High oxygen-reduction activity and durability of nitrogen-doped graphene. *Energy & Environmental Science* **4**, 760-764 (2011).

115. Zhao, Y. *et al*. A versatile, ultralight, nitrogen-doped graphene framework. *Angewandte Chemie-International Edition* **51**, 11371-11375 (2012).

116. Zhang, J.T., Zhao, Z.H., Xia, Z.H. & Dai, L.M. A metal-free bifunctional electrocatalyst for oxygen reduction and oxygen evolution reactions. *Nature Nanotechnology* **10**, 444-452 (2015).

117. Wu, Z.S., Ren, W.C., Xu, L., Li, F. & Cheng, H.M. Doped graphene sheets as anode materials with superhigh rate and large capacity for lithium ion batteries. *ACS Nano* **5**, 5463-5471 (2011).

118. Davis, M.E. Ordered porous materials for emerging applications. *Nature* **417**, 813-821 (2002).

119. Hiraoka, T. *et al*. Selective synthesis of double-wall carbon nanotubes by CCVD of acetylene using zeolite supports. *Chemical Physics Letters* **382**, 679-685 (2003).

120. Yang, Z.X., Xia, Y.D. & Mokaya, R. Aligned N-doped carbon nanotube bundles prepared via CVD using zeolite substrates. *Chemistry of Materials* **17**, 4502-4508 (2005).

121. Zhao, W., Kim, H.T. & Kim, I.J. Effect of catalysts on the yield and morphology of carbon nanotubes using a zeolite template. *Journal of Ceramic Processing Research* **13**, 81-85 (2012).

122. Vanderbilt, D. & Tersoff, J. Negative-curvature fullerene analog of $C_{60}$. *Physical Review Letters* **68**, 511-513 (1992).

123. Nueangnoraj, K. *et al*. Formation of crosslinked-fullerene-like framework as negative replica of zeolite Y. *Carbon* **62**, 455-464 (2013).

124. Ma, Z.X., Kyotani, T. & Tomita, A. Preparation of a high surface area microporous carbon having the structural regularity of Y zeolite. *Chemical Communications*, 2365-2366 (2000).

125. Park, C. & Keane, M.A. Controlled growth of highly ordered carbon nanofibers from Y zeolite supported nickel catalysts. *Langmuir* **17**, 8386-8396 (2001).

126. Yang, Z.X., Xia, Y.D. & Mokaya, R. Enhanced hydrogen storage capacity of high surface area zeolite-like carbon materials. *Journal of the American Chemical Society* **129**, 1673-1679 (2007).

127. Nishihara, H. *et al*. A possible buckybowl-like structure of zeolite templated carbon. *Carbon* **47**, 1220-1230 (2009).

128. Takai, K., Suzuki, T., Enoki, T., Nishihara, H. & Kyotani, T. Structure and magnetic properties of curved graphene networks and the effects of bromine and potassium adsorption. *Physical Review B* **81** (2010).

129. Kim, K. *et al*. Lanthanum-catalysed synthesis of microporous 3D graphene-like carbons in a zeolite template. *Nature* **535**, 131-135 (2016).

130. Ferrari, A.C. & Basko, D.M. Raman spectroscopy as a versatile tool for studying the properties of graphene. *Nature Nanotechnology* **8**, 235-246 (2013).

131. Pels, J.R., Kapteijn, F., Moulijn, J.A., Zhu, Q. & Thomas, K.M. Evolution of nitrogen functionalities in carbonaceous materials during pyrolysis. *Carbon* **33**, 1641-1653 (1995).

132. Yang, H.B. *et al*. Identification of catalytic sites for oxygen reduction and oxygen evolution in N-doped graphene materials: Development of highly efficient metal-free bifunctional electrocatalyst. *Science Advances* **2** e1501122 (2016).

133. Xue, Y.H. *et al*. Nitrogen-doped graphene foams as metal-free counter electrodes in high-performance dye-sensitized solar cells. *Angewandte Chemie-International Edition* **51**, 12124-12127 (2012).

134. Lai, L.F. *et al*. Exploration of the active center structure of nitrogen-doped graphene-based catalysts for oxygen reduction reaction. *Energy & Environmental Science* **5**, 7936-7942 (2012).

135. Wang, G.X., Shen, X.P., Yao, J. & Park, J. Graphene nanosheets for enhanced lithium storage in lithium ion batteries. *Carbon* **47**, 2049-2053 (2009).

136. Pan, D.Y. *et al*. Li storage properties of disordered graphene nanosheets. *Chemistry of Materials* **21**, 3136-3142 (2009).

137. Wang, G.P., Zhang, L. & Zhang, J.J. A review of electrode materials for electrochemical supercapacitors. *Chemical Society Reviews* **41**, 797-828 (2012).

138. Chen, T. & Dai, L.M. Carbon nanomaterials for high-performance supercapacitors. *Materials Today* **16**, 272-280 (2013).

139. El-Kady, M.F., Strong, V., Dubin, S. & Kaner, R.B. Laser scribing of high-performance and flexible graphene-based electrochemical capacitors. *Science* **335**, 1326-1330 (2012).

140. He, Y.M. *et al*. An overview of carbon materials for flexible electrochemical capacitors. *Nanoscale* **5**, 8799-8820 (2013).

141. Chen, Y. *et al*. High-performance supercapacitors based on a graphene-activated carbon composite prepared by chemical activation. *RSC Advances* **2**, 7747-7753 (2012).

142. Si, P., Ding, S.J., Lou, X.W. & Kim, D.H. An electrochemically formed three-dimensional structure of polypyrrole/graphene nanoplatelets for high-performance supercapacitors. *RSC Advances* **1**, 1271-1278 (2011).

143. Chen, T., Xue, Y.H., Roy, A.K. & Dai, L.M. Transparent and stretchable high-performance supercapacitors based on wrinkled graphene electrodes. *ACS Nano* **8**, 1039-1046 (2014).

144. Nam, I., Park, S., Kim, G.P., Park, J. & Yi, J. Transparent and ultra-bendable all-solid-state supercapacitors without percolation problems. *Chemical Science* **4**, 1663-1667 (2013).

145. Geim, A.K. Graphene: status and prospects. *Science* **324**, 1530-1534 (2009).

146. Fan, X.L., Chang, D.W., Chen, X.L., Baek, J.B. & Dai, L.M. Functionalized graphene nanoplatelets from ball milling for energy applications. *Current Opinion in Chemical Engineering* **11**, 52-58 (2016).

147. Liu, J.L. *et al*. Improved synthesis of graphene flakes from the multiple electrochemical exfoliation of graphite rod. *Nano Energy* **2**, 377-386 (2013).

148. Lee, J.S., Ahn, H.J., Yoon, J.C. & Jang, J.H. Three-dimensional nano-foam of few-layer graphene grown by CVD for DSSC. *Physical Chemistry Chemical Physics* **14**, 7938-7943 (2012).

149. Li, N., Chen, Z.P., Ren, W.C., Li, F. & Cheng, H.M. Flexible graphene-based lithium ion batteries with ultrafast charge and discharge rates. *Proceedings of the National Academy of Sciences of the United States of America* **109**, 17360-17365 (2012).

150. Fan, X.L., Chen, T., & Dai, L.M. Graphene networks for high-performance flexible and transparent supercapacitors. *RSC Advances* **4,** 36996-37002 (2014).

151. Ismach, A. *et al*. Direct chemical vapor deposition of graphene on dielectric surfaces. *Nano Letters* **10**, 1542-1548 (2010).

152. Zhou, Y. & Loh, K.P. Making patterns on graphene. *Advanced Materials* **22**, 3615-3620 (2010).

153. Yuan, W.J. *et al*. The edge- and basal-plane-specific electrochemistry of a single-layer graphene sheet. *Scientific Reports* **3** 2248 (2013).

154. Zhang, K., Zhang, L.L., Zhao, X.S. & Wu, J.S. Graphene/polyaniline nanofiber composites as supercapacitor electrodes. *Chemistry of Materials* **22**, 1392-1401 (2010).

155. Yan, J. *et al*. Electrochemical properties of graphene nanosheet/carbon black composites as electrodes for supercapacitors. *Carbon* **48**, 1731-1737 (2010).

156. Zhang, L. & Shi, G.Q. Preparation of highly conductive graphene hydrogels for fabricating supercapacitors with high rate capability. *Journal of Physical Chemistry C* **115**, 17206-17212 (2011).

157. Dimitrakakis, G.K., Tylianakis, E. & Froudakis, G.E. Pillared graphene: a new 3-D network nanostructure for enhanced hydrogen storage. *Nano Letters* **8**, 3166-3170 (2008).

158. Varshney, V., Patnaik, S.S., Roy, A.K., Froudakis, G. & Farmer, B.L. Modeling of thermal transport in pillared-graphene architectures. *ACS Nano* **4**, 1153-1161 (2010).

159. Kim, N.D. *et al*. Growth and transfer of seamless 3D graphene-nanotube hybrids. *Nano Letters* **16**, 1287-1292 (2016).

160. Dresselhaus, M.S., Jorio, A., Hofmann, M., Dresselhaus, G. & Saito, R. Perspectives on carbon nanotubes and graphene raman spectroscopy. *Nano Letters* **10**, 751-758 (2010).

161. Yen, H.J. *et al*. Structurally defined 3D nanographene assemblies via bottom-up chemical synthesis for highly efficient lithium storage. *Advanced Materials* **28**, 10250-10256 (2016).

162. Wang, Q.H., Kalantar-Zadeh, K., Kis, A., Coleman, J.N. & Strano, M.S. Electronics and optoelectronics of two-dimensional transition metal dichalcogenides. *Nature Nanotechnology* **7**, 699-712 (2012).

163. Hwang, H., Kim, H. & Cho, J. $MoS_2$ nanoplates consisting of disordered graphene-like layers for high rate lithium battery anode materials. *Nano Letters* **11**, 4826-4830 (2011).

164. Huang, X., Tan, C.L., Yin, Z.Y. & Zhang, H. 25th anniversary article: hybrid nanostructures based on two-dimensional nanomaterials. *Advanced Materials* **26**, 2185-2204 (2014).

165. Chang, K. & Chen, W.X. In situ synthesis of $MoS_2$/graphene nanosheet composites with extraordinarily high electrochemical performance for lithium ion batteries. *Chemical Communications* **47**, 4252-4254 (2011).

166. Wang, J. *et al*. Self-assembly of honeycomb-like $MoS_2$ nanoarchitectures anchored into graphene foam for enhanced lithium-ion storage. *Advanced Materials* **26**, 7162-7169 (2014).

167. Lee, C. *et al*. Anomalous lattice vibrations of single- and few-layer $MoS_2$. *ACS Nano* **4**, 2695-2700 (2010).

168. Teng, Y.Q. *et al*. $MoS_2$ nanosheets vertically grown on graphene sheets for lithium-ion battery anodes. *ACS Nano* **10**, 8526-8535 (2016).

169. Shi, Y.M. *et al*. Self-assembly of hierarchical $MoS_x$/CNT nanocomposites ($2 < x < 3$): towards high performance anode materials for lithium ion batteries. *Scientific Reports* **3** 2169 (2013).

170. Dominko, R. *et al*. Dichalcogenide nanotube electrodes for Li-ion batteries. *Advanced Materials* **14**, 1531-1534 (2002).

171. Aurbach, D., Markovsky, B., Weissman, I., Levi, E. & Ein-Eli, Y. On the correlation between surface chemistry and performance of graphite negative electrodes for Li ion batteries. *Electrochimica Acta* **45**, 67-86 (1999).

172. Zhao, C.Y. *et al*. Self-assembly-induced alternately stacked single-layer $MoS_2$ and N-doped graphene: a novel van der waals heterostructure for lithium-ion batteries. *ACS Applied Materials & Interfaces* **8**, 2372-2379 (2016).

173. Wang, B.B. *et al*. Facile synthesis of a $MoS_2$ and functionalized graphene heterostructure for enhanced lithium-storage performance. *ACS Applied Materials & Interfaces* **9**, 12907-12913 (2017).

174. Lu, C.X., Liu, W.W., Li, H. & Tay, B.K. A binder-free CNT network-$MoS_2$ composite as a high performance anode material in lithium ion batteries. *Chemical Communications* **50**, 3338-3340 (2014).